POLITECNICO DI MILANO

SCUOLA DI INGEGNERIA DEI PROCESSI INDUSTRIALI

Corso di Laurea Magistrale in Ingegneria Nucleare

Thermal Hydraulic Modeling of the Advanced High Temperature Reactor for the Evaluation of Steady State and Transient Conditions

Relatore: Prof. Marco Enrico RICOTTI

Correlatore: Prof. Bojan PETROVIC

Tesi di Laurea di

Pietro Avigni

Matricola 766599

TABLE OF CONTENTS

LIST OF TABLES

LIST OF FIGURES

LIST OF SYMBOLS AND ABBREVIATIONS

AHTR   Advanced High Temperature Reactor

ATWS   Anticipated Transient Without Scram

CHM   Carbon to Heavy Metal ratio

CVR   Coolant Void Reactivity

DHX   DRACS Heat Exchanger

DRACS   Direct Reactor Auxiliary Cooling System

FLiBe $2LiF\text{-}BeF_2$

LOFC   Loss Of Forced Cooling

LSCR   Liquid Salt Cooled Reactor

LS-VHTR   Liquid Salt cooled Very High Temperature Reactor

LUEC   Levelized Unit Electricity Cost

MCNP   Monte Carlo N-Particle

PHX   Primary Heat Exchanger

PRACS   Pool Reactor Auxiliary Cooling System

PRISM   Power Reactor Innovative Small Module

RELAP5-3D   Reactor Excursion and Leak Analysis Program

RVACS   Reactor Vessel Auxiliary Cooling System

SCALE   Standardized Computer Analyses for Licensing Evaluation

SmAHTR   Small Modular Advanced High Temperature Reactor

TRISO   TRi-ISOtopic fuel particle

UCO   Uranium OxyCarbide

ABSTRACT

The Advanced High Temperature Reactor (AHTR) is a molten salt cooled and TRISO fueled reactor, which presents very good features in terms of power production and safety aspects. This work evaluates the thermal hydraulic performance of the heat removal system and the reactor core, in steady state conditions as well as during accidental transients, starting from the single channel level and concluding with the full core model. The AHTR is a novel reactor concept that introduces some new features, not known from other reactors' operation and experience; other features are instead well known and used in actual operating plants, but still need to be integrated in the new concept. For these reasons, the thermal hydraulic modeling for the AHTR requires to be based on the few other molten salt reactors studied in the last decades.

A single channel MATLAB model was developed in order to evaluate the temperature distribution in the fuel plate and the other thermal hydraulic features of the average fuel element. The model was used for the evaluation of the effects of the axial and transversal power distribution in the plate, and some sensitivity studies were performed on the main dimensional and material parameters of the fuel element, looking at the maximum fuel temperature variation.

In parallel, a SCALE model of the fuel assembly was developed for the characterization of the neutronic aspects, including the power distributions in the core and in the plate and the reactivity feedback.

The MATLAB single channel model was validated by a RELAP5 single channel model, involving a single fuel plate and a single coolant channel; the comparison between the two model was performed in several different conditions, in order to make sure of the compatibility of the results.

The RELAP5 single channel model was then adapted for the modeling of the fuel assembly, accounting for the particular structure of the box wall and the layout of the plates into the channels. Subsequently, the fuel assembly model was integrated in a 9 rings core model, accounting also for the effects of the in-core structures, the heat removal system (up to the secondary loop) and the safety system (DRACS). The full core model was used for the evaluation of the thermal hydraulic features during a LOFC scenario, focusing on the heat removal system, and the fuel assembly removal transient, in order to assess the potential applicability of an online refueling procedure.

The core model presents the capability to simulate different types of transient, which will be evaluated in the future work, including also a more specific modeling of the coolant flow in the channel and a more complete description of the power production inside the plate, as well as a 3D plate temperature distribution.

L'Advanced High Temperature Reactor (AHTR) è un reattore a sali fusi con combustibile TRISO che presenta buone caratteristiche in termini di produzione di potenza e di sicurezza. Questo lavoro riguarda la valutazione della termo idraulica del sistema di rimozione del calore e del nocciolo del reattore, in condizioni stazionarie, così come durante transitori accidentali, partendo dal livello del singolo canale e concludendo con il modello del nocciolo. L'AHTR è un recente concetto di reattore che introduce alcune nuove caratteristiche, non note dall'attività ed esperienza di altri reattori; altre caratteristiche invece sono ben note ed utilizzate in impianti effettivamente operanti, ma ancora richiedono di essere integrate nel nuovo design. Per queste ragioni, il modello termo idraulico dell'AHTR richiede di essere concepito sulla base degli altri reattori a sali fusi studiati negli ultimi decenni.

È stato sviluppato il modello MATLAB del singolo canale al fine di valutare la distribuzione di temperatura nella piastra di combustibile e le altre proprietà termo idrauliche dell'elemento di combustibile medio. Il modello è stato utilizzato per la valutazione degli effetti della distribuzione assiale e trasversale di potenza nella piastra; sono stati effettuati inoltre alcuni studi di sensitività rispetto ai principali parametri geometrici e fisici dell'elemento di combustibile, facendo riferimento alla variazione della temperatura massima.

In parallelo, è stato sviluppato il modella SCALE dell'elemento di combustibile per la caratterizzazione degli aspetti neutronici, inclusi le distribuzioni di potenza nel nocciolo e nella piastra e la retroazione di reattività.

Il modello MATLAB di singolo canale è stato validato tramite il modello RELAP5 di singolo canale, che include una singola piastra di combustibile e un canale per il termovettore; il confronto tra i due modelli è stato svolto in alcune differenti condizioni, al fine di assicurare la compatibilità dei risultati.

Il modello RELAP5 di singolo canale è stato successivamente adattato per la modellazione dell'elemento di combustibile, tenendo conto della particolare struttura del supporto e della distribuzione delle piastre nel canale. In seguito, il modello dell'elemento di combustibile è stato integrato nel modello di nocciolo a 9 anelli, il quale rende conto anche degli effetti dovuti alle strutture interne al core, del sistema di rimozione del calore (fino al circuito secondario) e del sistema di sicurezza (DRACS). Il modello del nocciolo è stato utilizzato per la valutazione delle proprietà termo idrauliche durante durante un incidente LOFC, con particolare attenzione al sistema di rimozione del calore, e durante un transitorio di rimozione dell'elemento di combustibile, al fine di determinare la potenziale applicabilità di una procedura di online refueling.

Il modello di nocciolo mostra la capacità di simulare diverse tipologie di transitorio, che saranno valutate in futuro, includendo inoltre una più specifica modellazione del flusso del termovettore nel canale e una più completa descrizione della generazione di potenza nella piastra, così come della distribuzione tridimensionale di temperatura.

CHAPTER 1

INTRODUCTION

The Advanced High Temperature Reactor (AHTR) is a 3400 MWth fluoride-cooled reactor concept developed at Oak Ridge National Laboratory on the basis of the molten salt reactor design proposed by the Generation IV Technology Roadmap[1].

The molten salt coolant allows low-pressure operation at high temperature, leading to high thermodynamic efficiency of the plant as well as to potential process heat production, and relatively small reactor size. For these reasons, molten salt reactors have been studied for decades, starting with the Aircraft Reactor Experiment (1954), a 2.5 MWth reactor experiment designed to obtain high power density for suitable aircraft propulsion applications. During 1960s the experience with molten salts culminated with the Molten Salt Reactor Experiment (MSRE), a 7.4 MWth test reactor simulating an inherently safe thorium fuel cycle breeder reactor, which went critical in 1965 and run for an equivalent of 1.5 years of full power operation, reaching an outlet temperature as high as 650°C.

Looking at more recent developments, different molten salt cooled reactor concepts have been studied and designed; two main categories can be identified based on the fuel form and type:

- the fuel can be melted and circulating with the coolant, enabling the thorium fuel cycle and breeding with thermal spectrum; this is a long-term option, despite the great international effort in the development of this technology;
- the fuel (typically uranium oxycarbide) is in solid form, contained into a carbon-layered sphere (TRISO particle) and embedded into a graphite matrix; this option provides high safety performance and relies on relatively well-established technologies;

The AHTR belongs to the second configuration and it consists of an evolution and optimization of some molten salt reactor designs developed by ORNL starting from 2000. It is a relatively new and recent reactor concept even if most of its features come from different and well-known power production systems: TRISO fuel and high-temperature operation from HTGRs, molten salts from MSRs, water/air tolerant and high heat transfer performance coolants from LWRs, low primary pressure and hot refueling technology from Liquid Metal Reactors, supercritical steam cycle from advanced supercritical coal-fired plants.

The main issue with this reactor design consists of the low heavy metal loading of the core, due to the use of TRISO fuel. For this reason the mass of fuel loaded into a fuel assembly needs to be as high as possible, but this results in high temperatures and thermal stresses, potentially higher than the constraints imposed by the reliability of the system: the cooling system requires to be accurately designed in order to provide good heat removal and to reduce the thermal stresses of materials.

Given that the effectiveness of the cooling system can provide the required heat removal capability, the utilization of the fuel can be improved by adopting a multibatch fuel cycle; the plant configuration and the safety features of the AHTR enable the implementation of a pseudo-online refueling, a rapid (2-3 hours) exchange of few fuel elements, leading to a substantially higher fuel discharge burnup.

Since the cooling system is required to be able to remove the heat even during this rapid transitory, in which the temperature of the fuel can eventually increase and compromise the safety of the system, the thermal-hydraulic design of the AHTR is even more challenging.

This work consists of a global review of AHTR preconceptual design, followed by a deeper analysis of both thermal and neutronic features, in order to provide a starting point for the development of accurate core models.

The main purpose of this work is to generate a simple model of the core that would allow the understanding of the dynamics of transients and accidents.

Since this is a completely new reactor concept, little experience is available in relation to thermal-hydraulics modeling, even though, as mentioned above, the AHTR combines several different established technologies; substantially new are the plank fuel design, the coolant channel shape and, from a global standpoint, the overall interaction of these integrated technologies.

The research approach of this work is based on a simple initial model of the single coolant channel developed with MATLAB and used for parametric studies and overall benchmarking; then the code RELAP5-3D, a 3D thermal-hydraulic code for transient's evaluation, is used to model the single channel, the fuel assembly and the core, as well as the global reactor system, allowing the study of all scenarios of interest; the code SCALE6.1 is used for neutronic evaluations, particularly for the reactivity feedback characterization.

The work is organized as follows: Chapter II gives a global description of the reactor structure, the core and the fuel assembly as they are designed by ORNL and presented in some recent reports; Chapter III summarizes the work performed in the last years about the modeling and study of liquid salt cooled reactors as well as some common neutronic and thermal-hydraulic features of this family of reactors; Chapter IV shows the modeling and results for preliminary studies made through the MATLAB model, compared to the RELAP model of the single channel; Chapter V presents the modeling for the single fuel assembly, the core and the reactor components and shows the results of the simulations for the core model, for different transient conditions; finally, Chapter VI gives some conclusions and an overview of the future work.

CHAPTER 2

REACTOR CORE AND NUCLEAR POWER PLANT DESIGN

The AHTR plant design and configuration is presented in several ORNL reports and summarized in this chapter.

2.1   Summary plant description

The overall objectives of the AHTR plant design are listed as follows:

- Plant operational life of at least 60 years;
- Net thermal efficiency of 45%;
- Plant availability of 92%;
- All essential safety features passive;
- Construction time less than 36 months;
- LUEC (Levelized Unit Electricity Cost) lower than competing technologies.

The mean outlet temperature of the core is 700°C, enabling a peak steam temperature of 650°C in the supercritical water power cycle. This leads to a 45% thermal efficiency, 12% higher than currently operating LWRs: for a 3400 MW_{th} plant, the net electrical power output is 1530 MW_e. Such high temperatures can be reached through the use of a fluoride salt coolant, which is an effective heat transfer medium and remains liquid at atmospheric pressure up to the evaporation temperature, about 1400°C. Also the coated particle fuel allows high-temperature operation, but requires graphite as moderator and so the power density is lower than in existing LWRs. Table 2.1 lists the main AHTR parameters.

The plant is composed of the primary, intermediate and power loop; the circulating fluids are FLiBe, KF-ZrF$_4$ and water, respectively. The heat transfer salt used in the direct reactor auxiliary cooling system (DRACS) is similar to the intermediate salt, and the ultimate heat sink is the atmospheric air. The chemical purity of both the primary and the intermediate salt, maintained by two different chemical control systems, is needed in order to limit the corrosion of structural materials and keep transparency for visual maintenance and refueling operations.

A complete overview of the plant configuration is presented in Ref. 2 and in Figure 2-1.

The primary circuit is connected to three heat transfer loops through three primary heat exchangers (PHX); each secondary circuit is connected to a unique supercritical water generator, from which two power loops convert the heat provided by steam into electric power, in a similar way to advanced supercritical coal plants. Two cooling towers are needed, one for each power loop; based on the availability of surface water, the towers can be natural draft evaporative cooling towers, hybrid wet-dry cooling towers or water-to-air heat exchangers. Cooling systems

for the reactor building are required in order to guarantee long-term passive safety; argon, air and other non-boiling cooling fluids are used in place of traditional water systems.

Table 2.1. Key AHTR parameters

Parameter	Value	Units
Overall parameters		
Core thermal power	3400	MW
Net electrical power	1530	MW
Overall thermal efficiency	45%	-
Reactor core parameters		
Fuel type	TRISO particles in graphite plates	
Uranium composition	UCO	-
Fuel enrichment	9.00/19.75	wt.% ^{235}U/U
Number of fuel assemblies	252	-
Assembly lattice type	Hexagonal	-
Fuel plates per assembly	18	-
Moderator and reflector	Graphite	-
Core height (fueled region)	5.5	m
Equivalent core diameter (fueled region)	7.81	m
Primary salt circuit parameters		
Primary coolant salt	FLiBe	-
Average reactor outlet temperature	700	°C
Primary coolant return temperature	650	°C
Primary coolant flow rate	28500	kg/s
Primary coolant pressure	Atmospheric	-
Number of loops	3	-
Intermediate salt circuit parameters		
Intermediate coolant salt	KF-ZrF$_4$	-
Intermediate salt supply temperature	675	°C
Intermediate salt return temperature	600	°C
Intermediate salt flow rate	43200	kg/s
Intermediate salt pressure	Atmospheric	-
Number of loops	3	-
Power cycle parameters		
Fluid to high pressure turbine	Supercritical steam	-
Turbine supply temperature	650	°C
Turbine supply pressure	24	Mpa
Turbine generator type	Tandem-compound	-
Decay heat removal		
DRACS heat transfer salt	53% KF-47% ZrF$_4$	mol %
DRACS heat sink	atmosphere	-
Number of DRACS loops	3	-
DRACS maximum power	8.75	MW
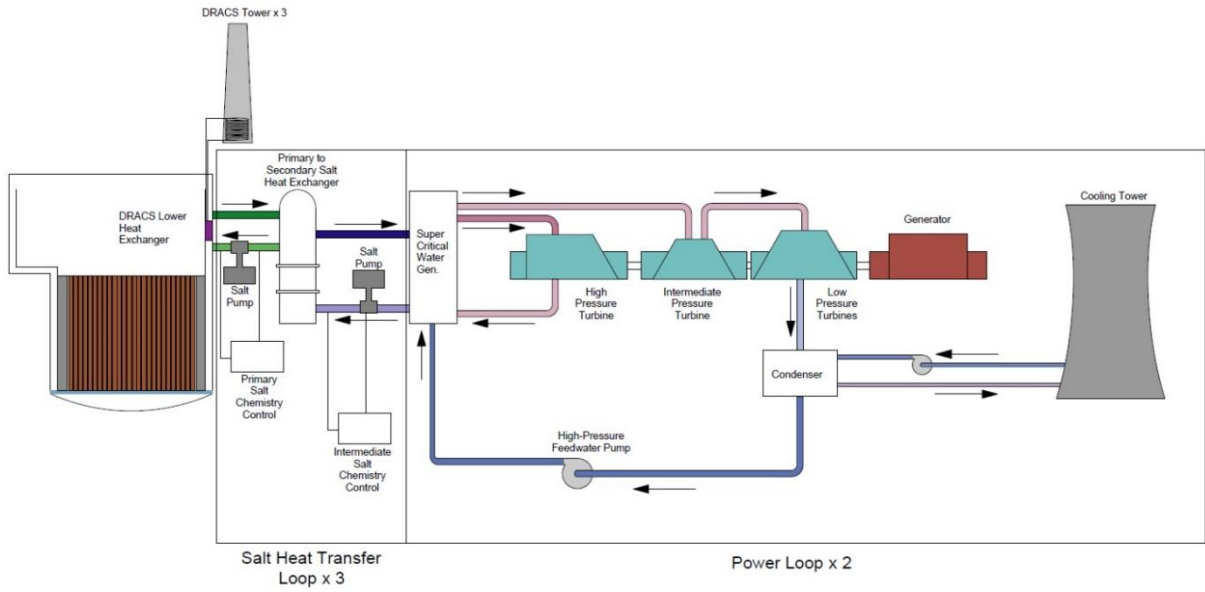
Figure 2-1. AHTR electric power generation[2]

2.2 Building and vessel description

An overview of the reactor building and the primary circuit is given in Figure 2-2.
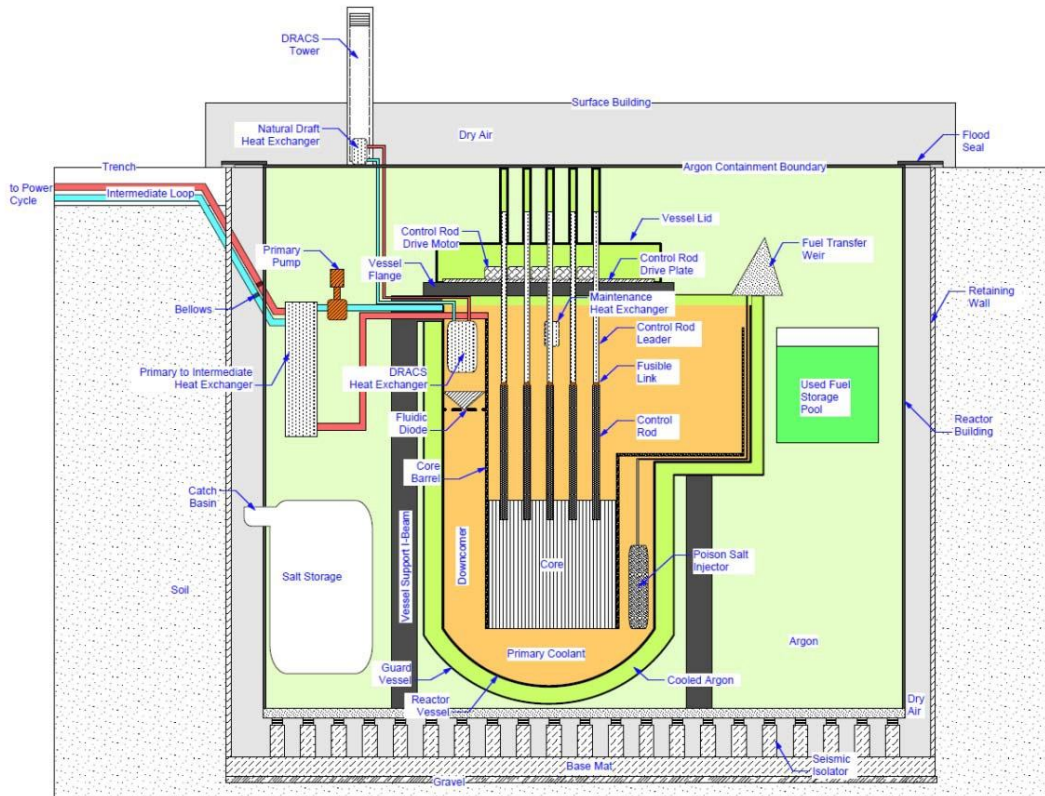
Figure 2-2. Reactor building layout[2]

The entire building is located below the ground level in order to minimize the effects of an eventual aerial impact; seismic isolators are provided as a protection against earthquakes.

The main features of the building layout are listed below:

- Outside dry air gap and inside argon atmosphere for building insulation and cooling;
- Salt and used fuel storage pools;
- I-Beams supporting the vessel, which is hung from its top flange;
- Guard vessel: keeps the core covered by coolant in the eventuality of a primary vessel rupture;
- Primary heat exchangers, primary piping and DRACS system;
- Control rod upper flange and refueling lobe.

The reactor vessel has the following dimensions: exterior vessel diameter equal to 10.5 m, vessel height equal to 19.1 m, primary salt depth above the upper core support plate equal to 7.15 m.

The penetrations for the inlet and outlet primary piping are located at the top of the vessel, to keep the core covered with salt even in the case of a rupture of the primary piping.

A C-C composite barrel separates the core region, with upward flow, from the downcomer region, located radially outside the barrel; the downcomer shell is divided into seven angular zones: three zones for the inlet downward flow, three zones for the DRACS recirculation system and the last zone is occupied by the refueling lobe.

The lower plenum serves as a salt mixing volume; the upper plenum collects coolant from different radial core positions and contains the control rod drive tubes, which can be extracted during refueling operations.

A cross section of the vessel is shown in Figure 2-3.
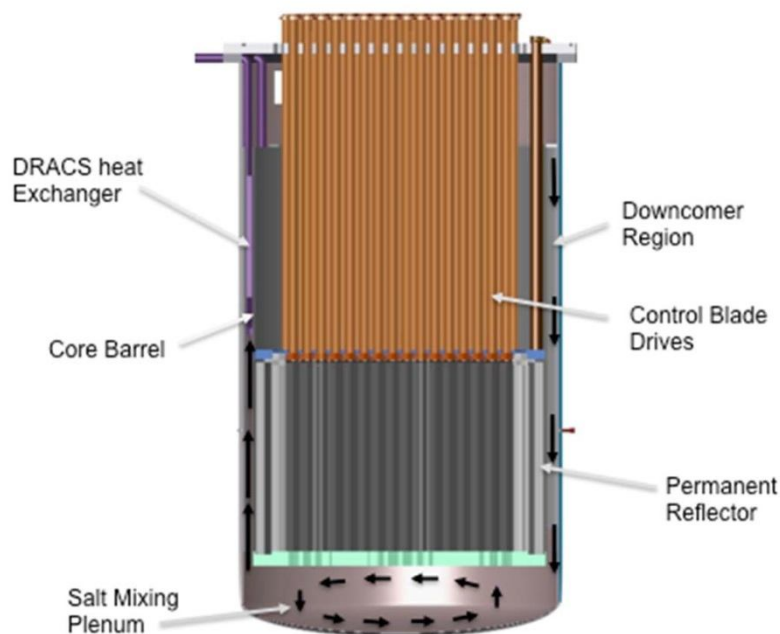
Figure 2-3. Vessel cross section[2]

2.3   Core description

The reactor core consists of 252 hexagonal fuel assemblies, 60 replaceable external reflector assemblies, a permanent radial reflector, and the lower and upper support plates.

A cross-sectional view of the reactor core is given in Figure 2-4 and the main core parameters are given in Table 2.2.
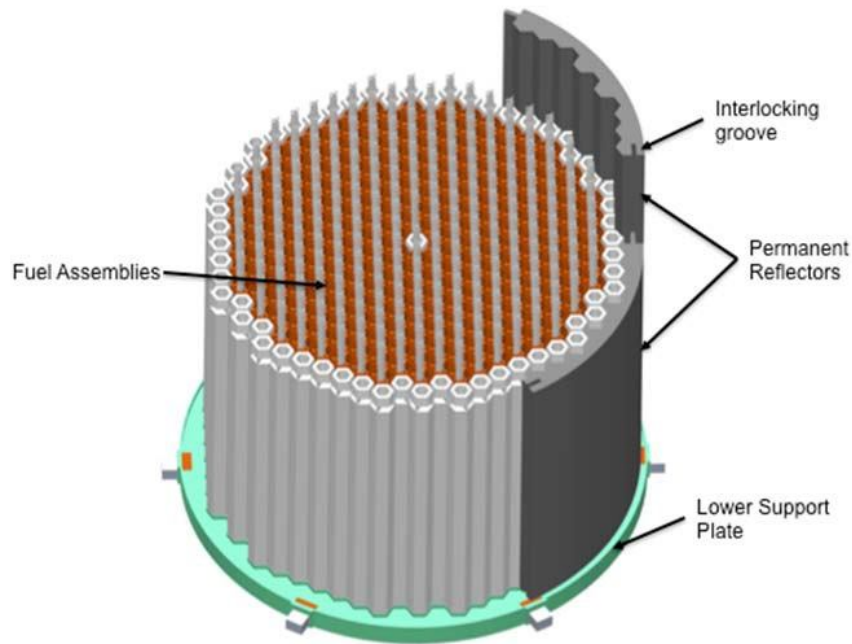
Figure 2-4. Cross-sectional view of the core[2]

Table 2.2. Main core parameters

Parameter	Value	Units
Power (thermal)	3400	MW
Number of fuel assemblies	252	-
Assembly lattice type	Hexagonal	-
Fuel type	Coated particle	-
Moderator	Graphite	-
Reflector	Graphite	-
Coolant	FLiBe	-
Coolant pressure drop across the core	1	atm
Core height (fueled region)	5.5	m
Core height (including axial reflector)	6.0	m
Equivalent core diameter (fueled region)	7.81	m
Core diameter (including radial reflector)	9.56	m
Average power per grain	41	mW/particle
Average power density in fueled region	52	W/cm^3
Volumetric core power density	12.9	MW/m^3
Mass of heavy metal	32.91	MT
Fuel enrichment	9 (19.75)	%

The fuel assembly overall average mass density is similar to the coolant mass density, so, in order to reduce the upward force exerted on the assembly by the coolant, the core is designed so that the friction pressure drop is lower than 1 atm.

The radial reflection is given by a replaceable and a permanent reflector; the axial reflection is given by 25 cm of graphite added below and above the active core height.

Despite the high thermal power produced by the core, its large diameter makes the AHTR volumetric power density lower than currently operating LWRs.

Two levels of enrichment were evaluated; the 19.75% enrichment was considered relatively high with respect to the current capabilities of enrichment plants, even if some interesting improvements could be obtained from the neutronic standpoint; the current design is based on a 9% enrichment.

The core is supported by the lower core support plate, a 35 cm thick honeycomb structure made of C-C composite, which regulates the mass flow rate in each core channel.

The upper support plate, with dimensions and configuration similar to the lower support plate, holds the assemblies in place during normal reactor operation; it can be raised during refueling operations.

2.4   Fuel assembly description
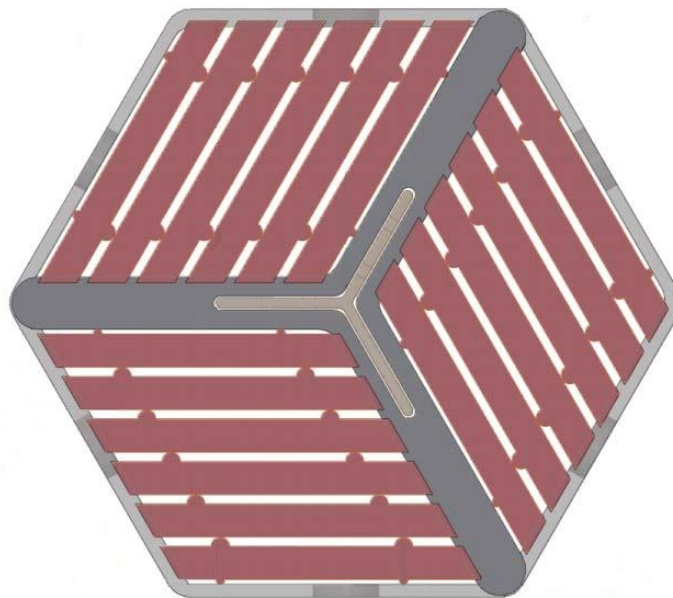
Figure 2-5. Transverse cross-section of the assembly with dimensions in cm²

The fuel assembly is a 6 m tall hexagonal prismatic block, of which the first and last 25 cm are reflector material. The outside distance between two faces of the hexagon is 45 cm and the inter-

assembly distance is about 1.75 cm. The wall, made of C-C composite and about 1 cm thick, forms a channel, which is divided into three symmetric/periodic zones by a Y-shaped support. Each assembly is provided with a Y-shaped control rod, inserted into the Y-shape, and fuel plates are supported by the assembly wall on one side and by a branch of the Y-shape on the other. Figure 2-5 shows the cross-section of the assembly and Table 2.3 gives the main assembly dimensions.

Table 2.3. Assembly main characteristics

Parameter	Value	Units
Total height	600	cm
Fueled region height	550	cm
Fuel assembly pitch	46.75	cm
Outer apothem	22.5	cm
Channel box wall thickness	1	cm
Y-shape thickness	4	cm
Coolant thickness between plates	7	mm
Coolant thickness between plate and wall	3.5	cm
Control blade thickness	1	cm
Control blade location wing length	10	cm
Fuel plate thickness	2.55	cm
Number of fuel plates	18	-

2.4.1 Fuel plate

The fuel plate design represents an evolution from the fuel concept of the SmAHTR.[3] The fuel plate is a rectangular prism 6 m high, the thickness of the plate is 2.55 cm.

The fuel is located in two stripes 6.2 mm thick, on both sides of the plate; a central non-fueled graphite "meat" provides the required moderation and a thin (1 mm) graphite sleeve protects the fuel from being eroded by the coolant.

Two spacer ridges are positioned on one of the two faces of the plate, to keep the correct distance between adjacent plates.

Figure 2-6 shows a cross-sectional view of the fuel plate.
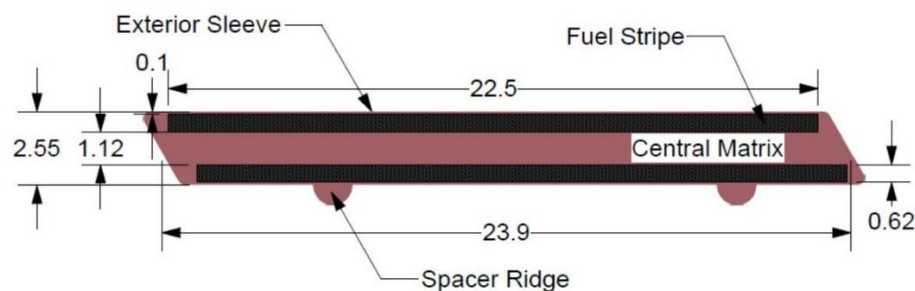
Figure 2-6. Fuel plate cross-section (all dimensions shown in cm)[2]

2.4.2 Control blade design

One control blade per assembly is employed, with relatively low reactivity worth; the rod is made of a Molybdenum-Hafnium carbide alloy (MHC), with a density of 10.28 g/cm^{3}, which makes the average density of the assembly higher than that of the coolant and prevents it from floating. The control blade drive mechanism consists of a leader rod which is lowered from the upper flange penetrations, through a guide tube, and connected to the upper part of each control rod. Figure 2-7 shows the control rod drive mechanism.
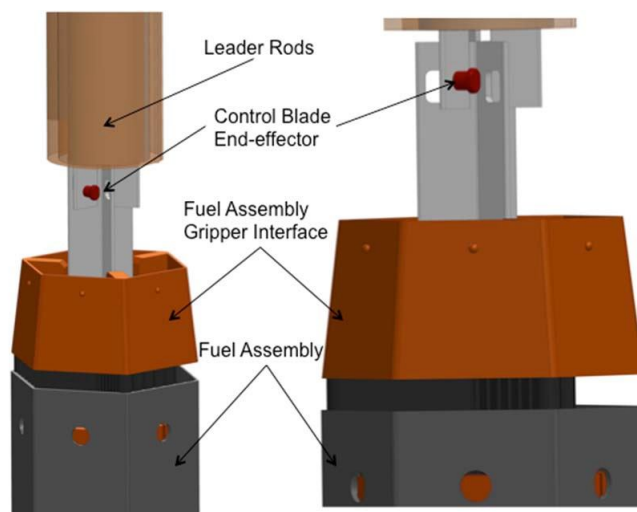
Figure 2-7. Control blade drive mechanism[2]

2.5   Materials

2.5.1 Coated particle fuel

The AHTR fuel is located in two narrow stripes for each fuel plate and is made of TRISO fuel particles dispersed into a graphite matrix. Typical particle parameters, from the AGR-2 prototype fuel presented in Ref. 4, are listed in Table 2.4.

Table 2.4. TRISO particle parameters[4]

Region	Parameter	Value [μm]	Material	Density [g/cm^3]
Kernel	diameter	427	UCO	10.90
Buffer	thickness	100	Porous graphite	1.00
IPyC	thickness	35	Pyrolitic graphite	1.90
SiC	thickness	35	SiC	3.20
OPyC	thickness	40	Pyrolitic graphite	1.87
Fuel particle	diameter	847	-	-
Matrix	pitch	927	Carbon material	1.59

Images of the fuel particle cross-section and structure are shown in Figure 2-8.
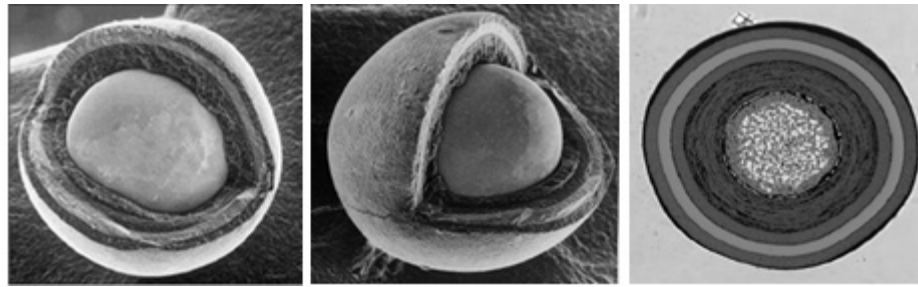
Figure 2-8. TRISO fuel particle cross-sections[5]

The pitch length was determined assuming a reference 40% packing fraction and a cubic lattice. The UCO kernel has a diameter of 427 μm and the following composition (molar fractions): 12.3% UC, 16.4% $UC_{1.86}$ and 71.4% UO_2.

The functions of the various particle shells are listed as follows:

- Fuel kernel: provides fission energy and retains fission products;
- Buffer layer: attenuates fission recoils, accommodates fission gases and kernel swelling;
- Inner Pyrocarbon: prevents chemical attack to kernel during manufacture, provides structural support for external layers and retains gaseous fission products;
- Silicon Carbide: primary load bearing member; retains gas and metal fission products;
- Outer Pyrocarbon: provides structural support for SiC and a fission product barrier in particles with defective SiC.

TRISO fuel is fundamental to AHTR design in order to reach higher operational temperatures and increase the overall thermal efficiency and plant capabilities; better safety performances are allowed, since the TRISO coating system provides an efficient primary barrier to the release of fission products. The irradiation performance of the particle is highly dependent on microstructure, which is subject to several failure mechanisms; an accurate control of coating properties and fuel service condition is required to avoid failure.

2.5.1.a   Thermal properties

Two crucial thermophysical properties are required in order to model TRISO fuel: thermal conductivity and specific volumetric heat.

The fact that this material is heterogeneous, since a great number of particles is mixed in a graphite matrix, is neglected and homogeneous properties are used; considering a power generation per particle of 41 mW (mean core value for the 2011 reference core model[6]), the geometrical configuration presented in Table 2.4 and a constant conductivity of 5 W/(m*K), it can be shown by solving the heat conduction equation for spherical geometry that the

temperature drop between the external surface and the central temperature of the particle is about 3°C; this temperature drop is low if compared to the mean fuel temperature, so the approximation made by considering an homogeneous material is reasonable in the context of our evaluations.

Little data is available regarding the thermal conductivity of TRISO fuel[7], the only recorded data available come from the German experience with HTGRs in the 1980s.

The effect of particle volume loading fraction (packing fraction PF, 40% for the AHTR fuel) was evaluated from several thermal conductivity measurements and was characterized as a multiplying factor φ, with respect to the pure (PF=0) graphite matrix conductivity, given by the following equation:

$$\varphi = (1 - PF)/\left(1 + {PF}/{2}\right) \qquad (2\text{-}1)$$

Figure 2-9 shows the dependence of the multiplying factor on the packing fraction: the higher is the packing fraction (which means the number of particles per unit volume) the lower is the fuel thermal conductivity.

In relation to the specific volumetric heat, little data were found in the past literature; little difference is expected between this material and the in-core graphite materials, whose properties are presented in section 2.5.2.
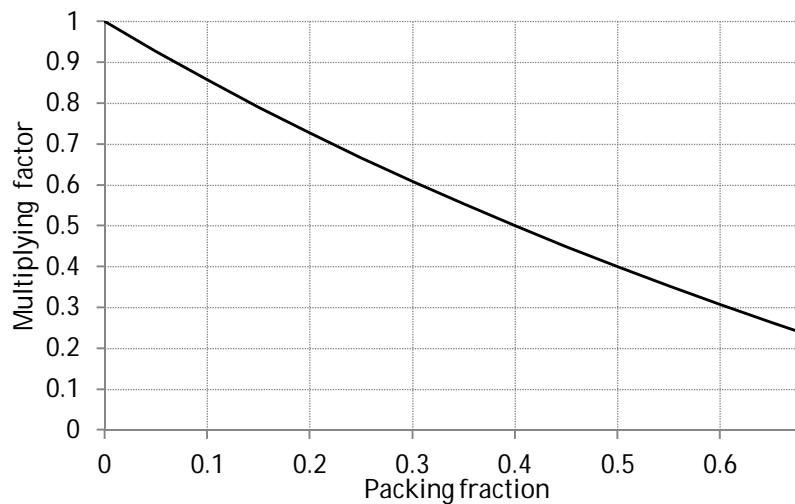
Figure 2-9. Fuel conductivity multiplying factor

2.5.2 In-core non-structural materials

Graphite is used as moderator material; the baseline AHTR design uses grade H-451 graphite, which is a near-isotropic, petroleum-coke-based, artificial graphite developed for HTGR fuel element and reflector applications. Other more recent and performing graphite grades are actually available, but their performance has not yet been completely characterized.[8]

Graphite density is 1740 kg/m3, the specific heat is given by the following formula:

$$c_p \left[\frac{J}{kg*K}\right] = 4184 \times (0.54212 - 2.42667 \times 10^{-6} \times T - 9.02725 \times 10^{1} \times T^{-1} +$$
$$-4.34493 \times 10^{4} \times T^{-2} + 1.59309 \times 10^{7} \times T^{-3} - 1.43688 \times 10^{8} \times T^{-4}$$

(2-2)

Figure 2-10 shows the specific heat as a function of graphite temperature.
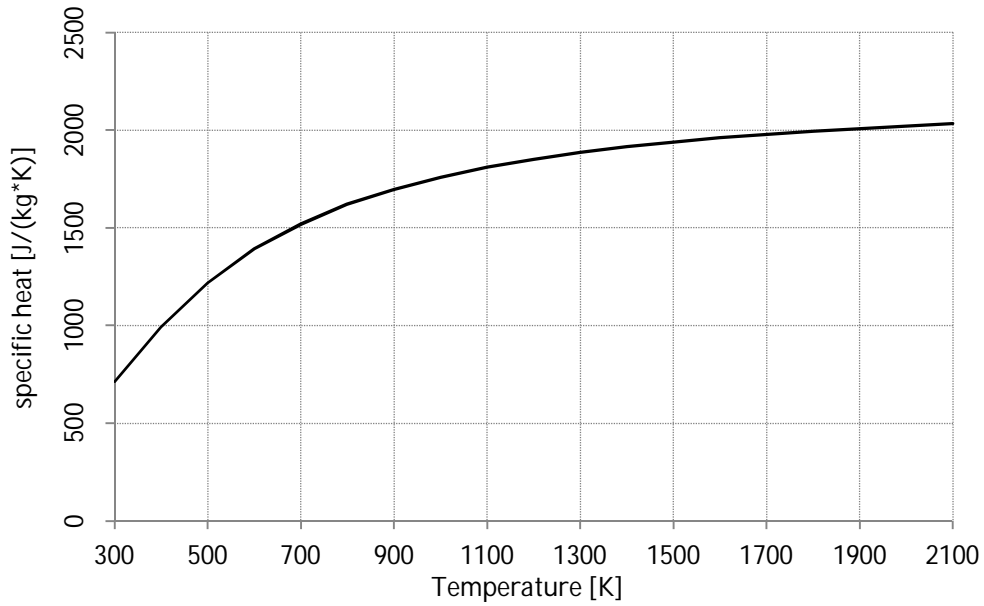
Figure 2-10. Specific heat for graphite H-451 as a function of temperature
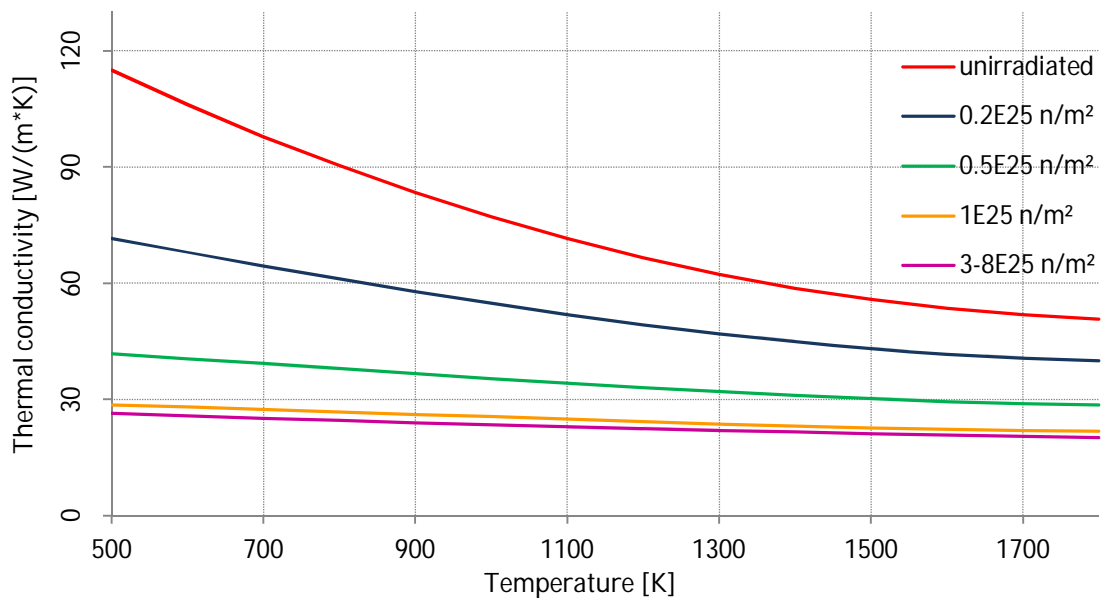
Figure 2-11. Thermal conductivity for graphite H-451 as a function of temperature, for different irradiation conditions

Thermal conductivity depends on the temperature as well as on the irradiation, i.e., fast neutron fluence; experimental data are available for the unirradiated graphite and for neutron fluence values up to $8*10^{25}$ n/cm^2, in the temperature range from 500 K to 1800 K. Figure 2-11 shows thermal conductivity dependence on temperature for different neutron fluence values.

2.5.3 Molten salt coolants

Molten salts have been considered as possible coolants for high temperature reactors, such as AHTR, for the following reasons:

- Relatively low melting point and high boiling point; wide range between the two limiting temperatures;
- Good heat transfer capabilities, high density and heat capacity;
- Low vapor pressure, low operation pressure;
- Good neutronic properties, low absorption.

Generally, lower-Z salts tend to exhibit better heat transfer and neutronic properties, because of higher heat capacities and lower absorption cross section, along with higher moderation capability. In relation to the compatibility with structural materials, the use of superior container alloys is required in order to limit the corrosion.

Table 2.5 shows possible salt choices compared to more conventional coolants, such as water or sodium.

Table 2.5. Properties of molten salts and common coolants[9]

Coolants	Heat capacity [cal/(g*K)]	Density [g/cc]	Viscosity [cP]	Volume expansivity [1/°C]	Thermal conductivity [W/(m*K)]	Prandtl number
Comparison coolants						
Water (300*C)	1.370	0.72	0.09	3.30E-03	0.54	0.967
Na (550°C)	0.303	0.82	0.23	8.60E-04	62	0.004
NaF-NaBF$_4$ (700°C)	0.360	1.75	0.88	4.25E-04	0.5	2.64
Candidate salt coolants at 700°C						
LiF-NaF-KF	0.450	2.02	2.9	3.61E-04	0.92	5.938
LiF-NaF-RbF	0.236	2.69	2.6	3.01E-04	0.62	4.143
2LiF-BeF$_2$	0.577	1.94	5.6	2.52E-04	1	13.525
NaF-BeF$_2$	0.520	2.01	7	1.84E-04	0.87	17.513
LiF-NaF-BeF$_2$	0.489	2.00	5	2.25E-04	0.97	10.551
LiF-ZrF$_4$	0.292	3.09	>5.2	2.99E-04	0.48	>13.241
NaF-ZrF$_4$	0.280	3.14	5.1	2.96E-04	0.49	12.199
KF-ZrF$_4$	0.251	2.80	<5.1	3.17E-04	0.45	<11.907
RbF-ZrF$_4$	0.200	3.22	5.1	3.11E-04	0.39	10.948
LiF-NaF-ZrF$_4$	0.300	2.79	6.9	3.12E-04	0.53	19.073

As we can see from the previous table, the heat capacity of salts is lower than in the case of water, but the density is higher, about double than water, so the heat transfer properties are still good.

The viscosity of salts is higher than the viscosity of water, so an optimized design of the coolant channels is required in order to reduce the friction pressure drop and the pumping power.

From the standpoint of the cost of the coolant components, there are three categories of salts: relatively inexpensive commodity chemicals (NaF), moderately expensive specialty materials (Zr-metal, LiF), very expensive specialty materials ([7]LiF, Be); however the cost of molten salts cannot easily be predicted, because many of the previous indicated constituents are not commodity chemicals available on the market. In 1971 the price of FLiBe was estimated by an ORNL survey at 52.2 $/liter, while, for comparison, the price of lead was 4.1 $/liter and the price of sodium was 0.72 $/liter.

2.5.3.a   Primary salt: FLiBe

For the primary circuit the FLiBe was selected, because of a high value of heat capacity, good radiation resistance, very low activation and neutronic absorption.

The composition of the salt is 66% LiF and 33% BeF2, the melting point is 459°C and the boiling point is 1430°C; the use of beryllium and enriched lithium makes this salt more expensive than other salts, but the overall performance is expected to be good. The advantage of the use of a molten salt is the atmospheric pressure core operation, which allows thinner and cheaper piping and vessel. Another advantage offered by FLiBe is the transparency which allows visual guidance of in-core operations during maintenance or refueling.

The main physical and thermal-hydraulic properties of this salt are implemented in RELAP5-3D[10], and the same correlations will be used in this work, as following described:

Specific heat (constant): $\qquad$ 2415 $J/_{kg*K}$ $\qquad$ (2-3)

Thermal conductivity (constant): $\qquad$ 1.1 $W/_{m*K}$ $\qquad$ (2-4)

Density: $\qquad$ $\rho(T[K]) = 2279.7 - 0.4884 * T[K]$ $kg/_{m^3}$ $\qquad$ (2-5)

Dynamic viscosity: $\qquad$ $\mu(T[K]) = 1.16 * 10^{-4} * e^{3755/_{T[K]}}$ $Pa*s$ $\qquad$ (2-6)

2.5.3.b   Secondary salt: KF-ZrF$_4$

KF-ZrF$_4$ was selected by ORNL as the coolant for the intermediate circuit; the composition is 50% KF and 50% ZrF$_4$, the melting point is 390°C.

The heat transfer properties of this salt are not as good as properties of FLiBe, but it is substantially cheaper, since it contains neither beryllium nor lithium (eventually enriched in [7]Li); the absence of lithium represents a further advantage from the chemical standpoint, since, in case of piping failure in the heat exchangers, the purity of the enriched primary lithium would not be compromised.

Since the properties of KF-ZrF$_4$ are not implemented in RELAP5-3D, a salt with similar properties, NaF-ZrF$_4$, was selected for the simulations.

2.5.4 Structural materials

Different types of structural materials are used for different neutronic, thermal, mechanical conditions: ceramic materials are used for in-core structures, where the neutronic flux would be too high for metallic alloys; nickel-based alloys are used for out-core structures, such as vessel and piping, for which good mechanical properties are required.

2.5.4.a   In-core structural materials

All the materials for in-core structures (lower and upper core support plate, core barrel) are advanced ceramic composites, primarily carbon (C-C) or silicon carbide (Si-C) fiber composites, which show the following properties:

- Good mechanical features, such as high strength at high temperatures;
- Good irradiation tolerance and nuclear performance;
- Good compatibility with fluoride salts.

The use of carbon-based materials is required in order to withstand temperatures exceeding 700°C, combined with high neutron fluxes and exposure to fluoride salts, since existing steels and alloys are not suitable for this purpose; moreover, graphite cannot be used because it would not provide enough tensile strength and toughness.[11]

Neither of the ceramic fiber has been qualified yet for use in reactor core; even if the manufacturability of ceramic materials is advancing rapidly, a large amount of work will be required in order to characterize the irradiation performance and mechanical limitations.[6]

2.5.4.b   Out-of-core structural materials

Since nickel is less vulnerable to dissolution into a fluoride salt than other elemental additions to common structural alloys and it is chemically compatible with fluoride salts at high temperature, nickel-based materials are leading candidates as structural materials.[12]

Several high-nickel alloys have been tested for use in high temperature reactors with molten salt coolants but, due to dissolution of alloying elements, none of these materials has been proven to be strongly corrosion-resistant; while a single material chemically compatible with salts would be preferable, a viable option is nickel cladding of a structural nickel-based alloy, similarly to stainless steel lining of a carbon steel vessel used in PWRs.

The cladding material must have the following properties: alloying elements with low solubility in liquid salts; high temperature exposure stability; good adhesion to the substrate, uniformity of composition, suitable mechanical properties and thermal expansion coefficient; several cladding techniques are available.

The primary vessel material is 800H (nickel-iron-chromium alloy) with an alloy N lining.

The piping material is Hastelloy N, a nickel-based alloy invented at Oak Ridge National Laboratory for specific use with molten salts; general properties of Hastelloy N are shown in Table 2.6.

Table 2.6. Hastelloy N properties[13]

Parameter	Temperature [°C]	Value	Units
Density	22	8.86	g/cm^3
Melting range	-	1300-1400	°C
Coeff. of thermal expansion	from 21 to 760	1.47E-05	1/°C
Thermal conductivity	700	23.6	W/(m*K)
Specific Heat	700	578	J/(kg*K)
Dynamic modulus of elasticity	700	171	Gpa
Yeld Strength	700	172	Mpa

2.6 Refueling

Two approaches to refueling are considered: the traditional multi-batch refueling with shutdown, and a novel pseudo-continuous approach.

2.6.1.a   Multi-batch refueling

Several combinations of fuel enrichment and cycle configuration have been examined and the configuration chosen for the refueling scheme of the AHTR baseline design is a two-batch cycle in which one half of the core fuel assemblies (126 out of 252) is replaced every six months; the enrichment (9%) was selected below 10% in order to enable the use of the existing enrichment facilities instead of building new plants; the cycle length was optimized, by varying the enrichment, in order to match the seasonal demand minimums.

The refueling procedure can be summarized as follows:

- All the control blades are inserted, the mass flow is reduced to 5% of the nominal value, the control rod guide tubes are removed and the upper core support plate is raised;
- Three automated refueling manipulators replace the used fuel with the fresh fuel in the core; the used fuel is removed from the core through a winch mechanism in the refueling lobe;
- The upper core support plate and the control blades are repositioned and the core is brought on power.

All the fuel reloading process is visually guided and automated in order to maximize the transfer speed and obtain a total refueling outage of 2-3 days.

2.6.1.b   Pseudo-online refueling

The core total fuel loading of the AHTR is limited by the enrichment and the use of a coated particle fuel type, since the fraction of volume occupied by heavy metal is relatively low.

The idea of the pseudo-online refueling is to utilize the better neutronic economy of a multibatch fuel cycle to improve the fuel utilization and increase the burn-up.

The procedure for the pseudo-online refueling is the same as the complete refueling but the outage duration is kept on the order of few hours to avoid the Xenon build-up, so only a limited number of fuel assemblies (between 12 and 18) can be replaced.

2.7   Safety design

The AHTR features full passive safety systems which do not require the action of an operator or an active control system to face all design basis accidents as well as beyond design basis accidents.

The first safety system is the primary shutdown system, consisting of neutron absorbing control blades, one for each fuel assembly, that can be lowered into the core through a motor or released in case of a loss of offsite power; a third release mechanism consists of a fusible link located at the top of the rod which would melt in case of high temperature increase and would let the rod fall into the core.

The secondary shutdown system is based upon the injection of rare earth fluoride salt into the inlet plenum through three canisters located in the part of the downcomer under the refueling lobe.

After the shutdown, the decay heat is removed through the primary cooling system; during maintenance of the primary system the maintenance heat removal system provides the required

cooling; if none of these two active systems is working, the decay heat is removed by the DRACS, which is completely passive.

A fourth method to remove decay heat is provided through the power generated by Stirling cycle generators which operate between the temperature of the used fuel storage pools and the outside temperature.

The AHTR has four different containment layers, as it is shown in Figure 2-12.
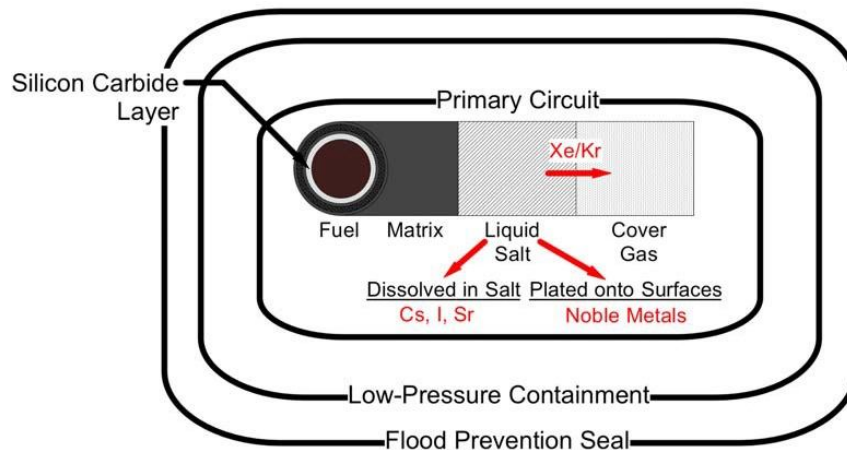
Figure 2-12. Containment layers[2]

The first layer is the SiC layer of the TRISO fuel particle; the second layer is the primary circuit; the third layer is the low-pressure containment; the fourth layer is the flood prevention seal.

Several different accident scenarios have been considered, such as over-cooling, air or water ingress, plane impact, ATWS, inadvertent control element movement, vessel breach, primary loop break, loss of forced flow, loss of ultimate heat sink, station blackout, loss of grid connection, failure of reactor vessel internals, partial flow blockage, but a complete analysis of safety systems still needs to be performed.

CHAPTER 3

LITTERATURE REVIEW OF THERMAL-HYDRAULIC LSCR STUDIES

This chapter gives an overview of the previous work on the thermal-hydraulic analysis and modeling of Liquid Salt Cooled Reactors (LSCR).

This field is not very well explored yet, since the AHTR is a novel reactor concept that introduces some new features, not known from other reactors' operation and experience (as, for example, plate fuel design); some other features are instead well known and used in actual operating plants, but still need to be integrated together in the new concept.

Especially from the thermal-hydraulic standpoint, a large amount of work is needed to understand the normal behavior as well as the accidental transients and the response of the safety system.

The AHTR in particular is a relatively recent concept, developed and studied since 2010; there are few similar reactors which can have some similarities and can be useful in the understanding of the AHTR. In particular we will focus our attention over the Liquid Salt Very High Temperature Reactor (LS-VHTR), the Small modular Advanced High Temperature Reactor (SmAHTR) and the Pebble bed Advanced High Temperature Reactor (PbAHTR).

3.1 Thermal-hydraulic modeling of molten salt reactors

This section presents a general description of the reactor designs previously mentioned, focusing on the models of the core and the global reactor system, including the safety systems. Particular attention is given to the RELAP5-3D models, since a similar model for the AHTR will be developed and presented in the next chapters.

3.1.1 Liquid Salt Very High Temperature Reactor (LS-VHTR)

The Liquid-Salt-Cooled Very High-Temperature Reactor (LS-VHTR) is a variant of the gas-cooled very high-temperature reactor (VHTR) concept and combines four established technologies in a new way: (1) coated-particle graphite-matrix fuels successfully used in helium-cooled reactors, (2) passive safety systems and plant designs previously developed for liquid metal-cooled fast reactors, (3) low-pressure liquid-salt coolants studied extensively for use in liquid-fueled reactors, and (4) high-temperature Brayton power cycles. The new combination of technologies enables the design of a high-power [2400 to 4000 MW$_t$], high-temperature (850 to 950°C) reactor with fully passive safety capability and economic production of electricity or hydrogen.

1.1.1.a LS-VHTR general description

The LS-VHTR uses coated-particle graphite-matrix fuels and a liquid-fluoride-salt coolant. The optically transparent liquid-salt coolant is a mixture of fluoride salts which provide good heat transfer capabilities and high safety performance. The reactor operates at near-atmospheric pressure.

The reactor and assembly layout for the LS-VHTR are shown in Figure 3-1 and Figure 3-2.
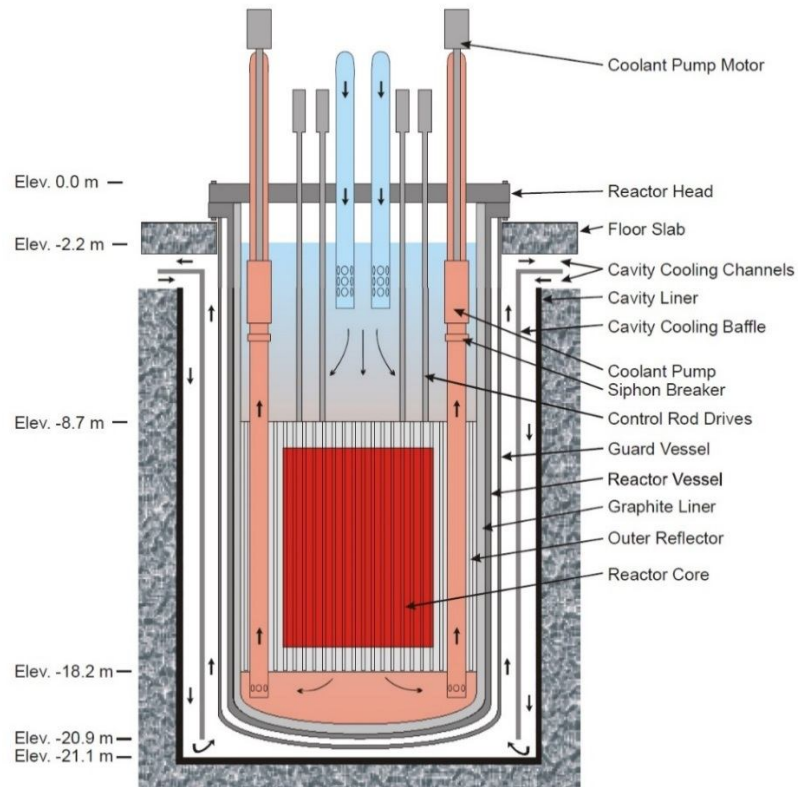
Figure 3-1. LS-VHTR reactor layout[14]
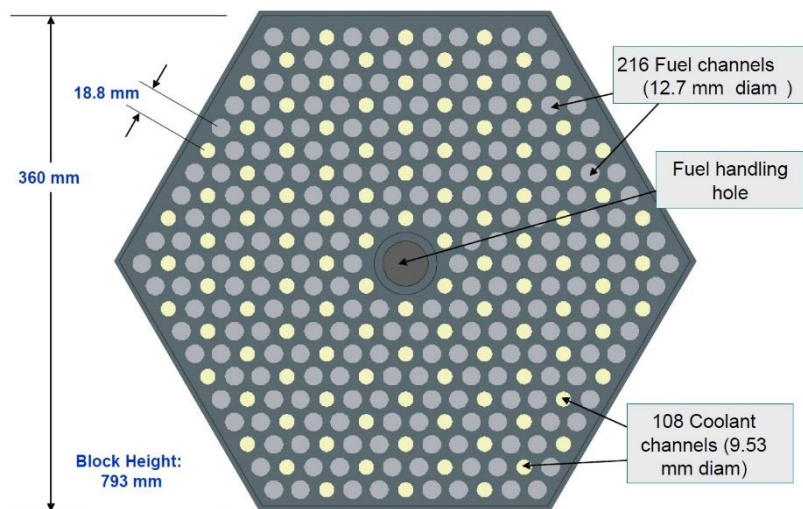
Figure 3-2. LS-VHTR assembly configuration[14]

21

3.1.1.a LS-VHTR RELAP5-3D modeling and safety performance

Thermal-hydraulic analyses were performed to evaluate the safety performance of the LS-VHTR. A one-dimensional model of the LS-VHTR was developed using the RELAP5-3D computer program. The RELAP5-3D nodalization diagram of the LS-VHTR is illustrated in Figure 3-3.
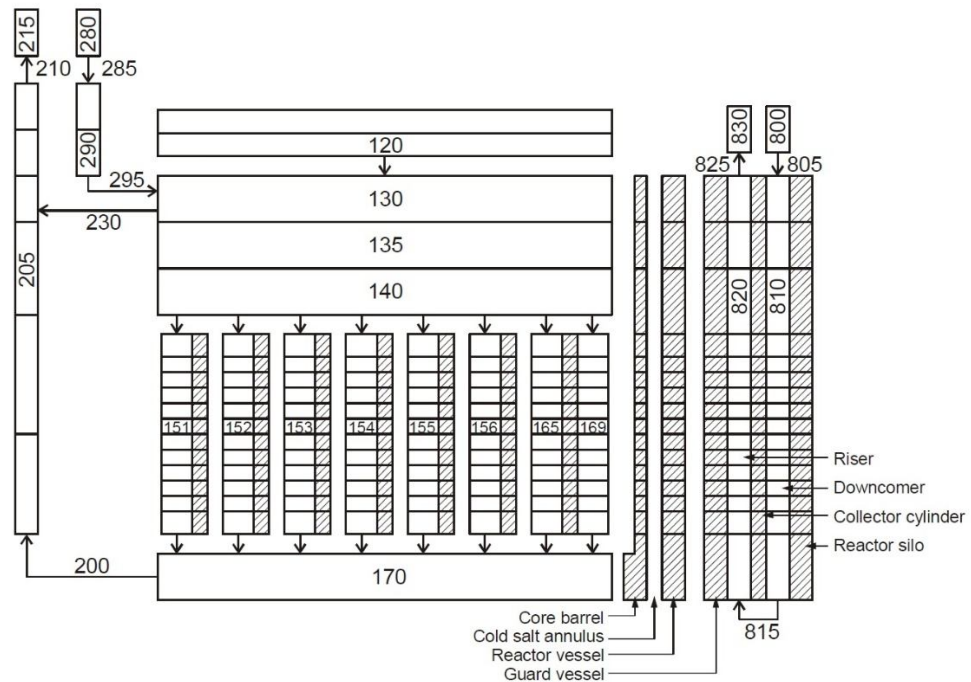
Figure 3-3. RELAP5-3D nodalization diagram of the LS-VHTR[14]

The reactor power is calculated with a point kinetics model. The decay heat is calculated from the ANS-5.1 standard [ANS, 1979] for the infinite operation of [235]U.

The reactor vessel auxiliary cooling system (RVACS), a completely passive decay heat removal system, was integrated in the model, based on the PRISM design. This system shows good performance for high temperature reactors and could be adopted for the AHTR, but a direct reactor auxiliary cooling system (DRACS) was selected in the 2011 AHTR baseline design.[6]

Radiation enclosure models are used to represent the heat transfer between the reactor and guard vessels and between the guard vessel and the collector cylinder; the emissivity of these surfaces was set to 0.75.

The RELAP5-3D model was used to determine the steady-state operating conditions for the LS-VHTR.

The RELAP5-3D model of the fuel block is based on a one-dimensional representation of a unit cell. The unit cell effectively contains one coolant channel and two fuel channels; the RELAP5-3D model of a channel is a single cylindrical pin equivalent, in terms of volume, to the real fuel assembly configuration, as it is shown in Figure 3-4.
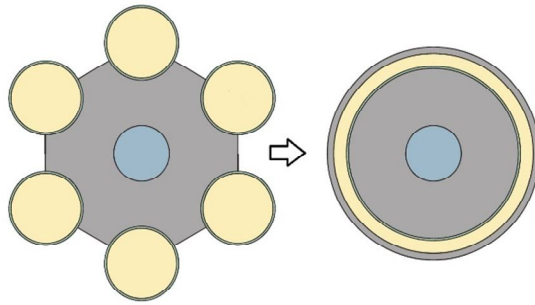
Figure 3-4. LS-VHTR coolant channel model[15]

This simplified model lead to a different fuel temperature profile than the real configuration, so some approximations were used to match the true fuel maximum and average temperatures. One of the main parameters to be determined was the heat transfer area in the unit cell, which varies between a minimum, which is based on the wetted perimeter of one coolant channel, to a maximum, that is similar to the one calculated from the wetted perimeter of two fuel channels. Since the selection of an optimal heat transfer area to use in a one-dimensional model is not obvious, detailed finite-element calculations were performed through the ABAQUS computer code. A similar procedure could be adopted for the AHTR modeling but the geometric configuration of the fuel is completely different (plate fuel design), so a simple cartesian mono-dimensional geometry, not cylindrical (as in the LS-VHTR case), could be more suitable.

The RELAP5-3D model was used to simulate a transient initiated by a loss of forced cooling (LOFC) accident. The transient was simulated by linearly reducing the flow in component 285 to 0 in 10 s. The reactor scram signal occurred at 1 s and the control rods were fully inserted 3 s later, shutting down the reactor. The RVACS was assumed to be the only system available for the decay heat removal.

Analysis of the calculated results showed that the radiation heat transfer between the reactor and guard vessels is more effective than the conduction through liquid salt.

The viability of the RVACS for passive cooling of the LS-VHTR in the presence of a reactor vessel leak will require relevant experiments or more detailed calculations.

Further calculations were performed to investigate the sensitivity of the results to various parameters, including the size of the coolant channels, the bypass flow fraction, the number of fueled rings in the core, the coolant outlet temperature, and radial/axial conduction in the core. Additional parametric calculations investigated the effects of enhanced RVACS design and a failure to scram.

Even with conservative data and analyses, the LS-VHTR has a strong passive safety performance and appears capable of surviving a LOFC, also with failure to scram. Significant natural convection of the coolant salt occurs, resulting in fuel temperatures below steady-state values and nearly uniform temperature distributions during the transient.

3.1.2   Small modular Advanced High Temperature Reactor (SmAHTR)

The SmAHTR is a 125 MW$_{th}$, integral primary system FHR concept. The design goals for SmAHTR are to deliver safe, affordable, and reliable high-temperature process heat and electricity from a small plant that can be easily transported to and assembled at remote sites.

The overall design parameters for the reactor are shown in Table 3-1, with a picture of the plant configuration (Figure 3-5).

Table 3-1. Sm AHTR design parameters

Parameter	Value	Units
Power	125 / 50+	MWt / MWe
Primary coolant	LiF-BeF$_2$	-
Fuel type, enrichment	TRISO, 19.75%	-
Number of assemblies, rings	19, 3	-
Primary Pressure	0.1 (1)	MPa, (atm)
Core inlet temperature	650	°C
Core outlet temperature	700	°C
Core coolant flow rate	~1000	kg/s
Heat removal-normal operation	3-50% loops	-
Passive Deacy Heat Removal (DRACS)	3 loops	-
Dimensions: height - diameter	9 - 3.5	m
Reactor vessel penetrations	none	-

SmAHTR employs three in-vessel primary heat exchangers (PHXs) and three DRACS heat exchangers. Each PHX is coupled with a main circulating pump. Except for the power level, the SmAHTR shows many similarities with respect to the AHTR, regarding the coolant features, the core structure and the safety system concept.

Several fuel and core design options for SmAHTR were investigated during the design evolution. These designs included solid cylindrical fuel "pins" in stringer fuel assemblies, hollow annular fuel pins in stringer fuel assemblies, and solid plate or "plank"-type fuel elements. The cylindrical fuel core consists of stacked prismatic blocks containing stringer fuel bundles. In the cylindrical fuel option, the TRISO particles are uniformly loaded at a 50% volumetric packing density into fuel cylinders. In the annular fuel SmAHTR core variant, the fuel is configured into annular compacts roughly 5 cm high that are strung along a carbon–carbon composite vertical tie rod. In the plank-fuel SmAHTR core design variant, the fuel is configured into full core height planks that are mounted into a carbon–carbon composite frame. The three variants are illustrated in Figure 3-6.

The SmAHTR concept introduces the plate fuel type, which will be the basis for the AHTR fuel design, with only few changes, regarding the number of plates (6 instead of 5) and the assembly dimensions.
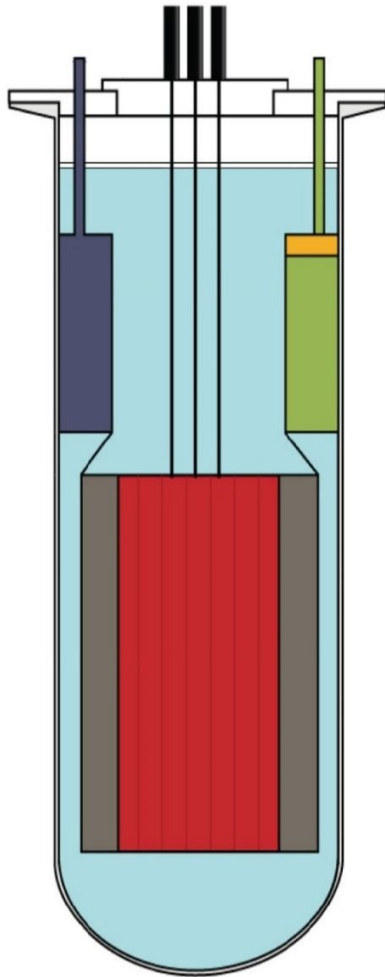
Figure 3-5. SmAHTR plant layout[3]
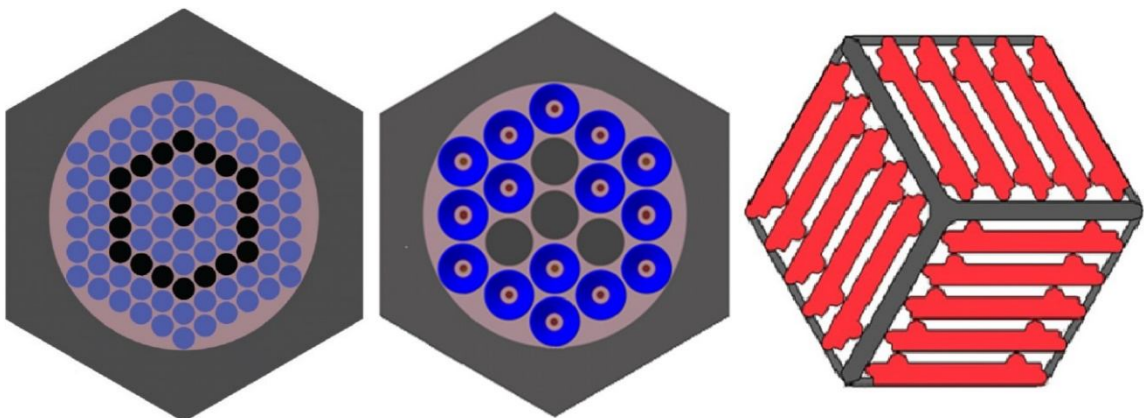
Figure 3-6. SmAHTR assembly layout[3]

All of the fixed fuel SmAHTR core mechanical configurations were analyzed in steady state conditions using RELAP5-3D, to evaluate their respective performance with respect to safety requirements.

3.1.2.a Direct Reactor Auxiliary Cooling System (DRACS)

The structure of the DRACS safety system is similar to the case of the AHTR, with different capabilities in terms of amount of power removed.

SmAHTR employs three DRACS loops, but the core decay heat is designed to be removed with only two of the three DRACS loops operating. Each DRACS loop removes decay heat passively to an outside natural draft air cooler. The salt selected for the coolant inside the tubes (the DRACS loop) is FLiNaK, which is a relatively low cost salt with good thermal performances. The DRACS heat exchanger (DHX) is located inside the vessel annulus and it is a single-pass, shell-and-tube cross flow heat exchanger. A vortex diode is located at the bottom of the heat exchanger to reduce reverse flow during normal operation.

A complete design for the AHTR's DRACS system is not yet available, so the SmAHTR design will provide the starting point in terms of heat exchanger's parameters, system layout and dimensions that will be used in this work for the modeling of the safety system.

A complete analysis of all the most relevant accident scenarios has not been performed; however, a preliminary analysis of the loss-of-flow transient has been completed.

A loss of forced flow with scram was analyzed to determine whether the DRACS system as designed could remove the decay heat during a loss-of-flow event; the RELAP5-3D model developed for this study is shown in Figure 3-7.
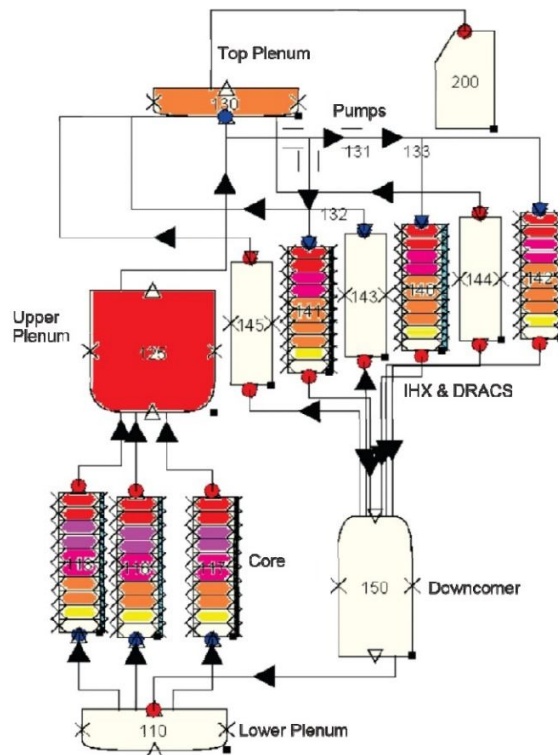
Figure 3-7. SmAHTR nodalization diagram for the primary system[3]

The results obtained from the RELAP5-3D model are satisfactory both for normal power operation and under decay heat operation, demonstrating the capability of the heat removal system to provide sufficient cooling.

3.1.3   Pebble bed Advanced High Temperature Reactor (Pb-AHTR)

The Pebble bed Advanced High Temperature Reactor is a liquid salt cooled high temperature reactor[16] which shows many similarities with the AHTR since it uses FLiBe as a primary coolant, graphite as moderator material, and has the same operational temperature range; the main difference consists of the pebble bed core. An overview of the plant is given in Figure 3-8.
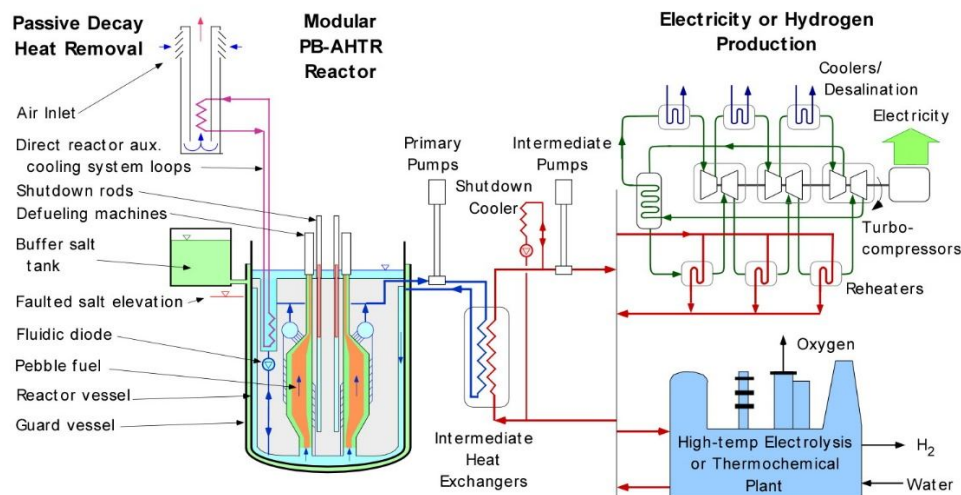
Figure 3-8. Plant overview[16]

The power output of this design is 900 MWth and the power density, similarly to the AHTR, is higher than the gas-cooled equivalent reactor because of the use of molten salts, a more effective coolant than helium. The outlet temperature is 704°C, the use of gas Brayton power conversion cycle is enabled and a high value of electrical conversion efficiency is reached (about 46%, equivalent to the AHTR). The use of FLiBe provides high safety features with low-pressure operation and fully passive decay heat rejection system; longer-term reactor scaling to higher power levels is possible, leading to improved economics.

The same fuel cycle option of the AHTR design is adopted (conventional low-enriched uranium), but many other options are available, including:

- Deep burn fuel cycle: destroy plutonium and transuranics;
- Once-through seed-blanket fuel cycle;
- Closed thorium fuel cycle.

3.1.3.a Safety features and RELAP5-3D modeling of the Pb-AHTR

The Pb-AHTR shows fully passive safety features which are obtained through a Pool Reactor Auxiliary Cooling System (PRACS): during a Loss Of Forced Cooling (LOFC) accident the pool, in which the core is contained, is heated by a natural circulation loop formed between the PHX modules and the hot salt coming out from the core. During the accident the temperature of the salt in the pool increases, due to the heat received from the PHX, so a DRACS system is integrated in the upper volume of the pool in order to remove the decay heat by cooling down the pool; the DRACS concept is similar to the AHTR design.

The LOFC transient for this reactor concept was accurately modeled and studied by Griveau;[17] the system failure occurs when one of the physical barrier for fission product release is broken, so the safety system must preserve the integrity of the containment layers by keeping the temperatures below the material constraints. In particular three limitations must be accounted for:

- Maximum fuel temperature lower than 1600°C; this is the limiting temperature for the TRISO silicon carbide layer integrity;
- Maximum piping alloy temperature lower than 980°C; this is the maximum temperature at which the Hastelloy N alloy can provide corrosion resistance;
- Maximum coolant temperature lower than 1400°C; this is the boiling temperature of FLiBe.

During the transient these thermal constraints must be respected; two different possible scenarios have been studied: the first is the LOFC, with normal scram occurring; the second is an Anticipated Transient Without Scram (ATWS), in which the scram does not occur and the temperature increase can potentially compromise the reactor integrity.

RELAP5-3D was used to model the reactor and to study the steady state as well as the transient during LOFC or ATWS. The nodalization diagram of the system is given in Figure 3-9; the hydrodynamic volumes are orange, while the heat structures are blue.

The core is divided into 4 rings and a particular correlation for the friction pressure loss coefficient is used in order to account for the pressure drop across the pebble bed. The primary circuit is not modeled as a closed loop but as an open circuit in which the flow is injected through junction 115 and an equal mass flow rate exits from the upper plenum through junction 171.

The LOFC transient is simulated as a ten seconds coast down of the mass flow rate injected by the inlet junction, from the nominal value to 0; the scram is actuated 3 seconds after the pump trip and the power profile assumed for the transient is the decay heat curve taken from previous calculations on the NGNP prismatic core.

No reactivity feedback is considered for the LOFC accident, while the point kinetics model is used for the ATWS transient; the coefficients obtained from the MCNP simulations are used in the kinetics equations definition.

The main aspects that are analyzed during the transient are the flow distribution inside the core, which is strongly affected by natural circulation effects, and the temperature variation with time, which shows that the system is very effective in heat removal.
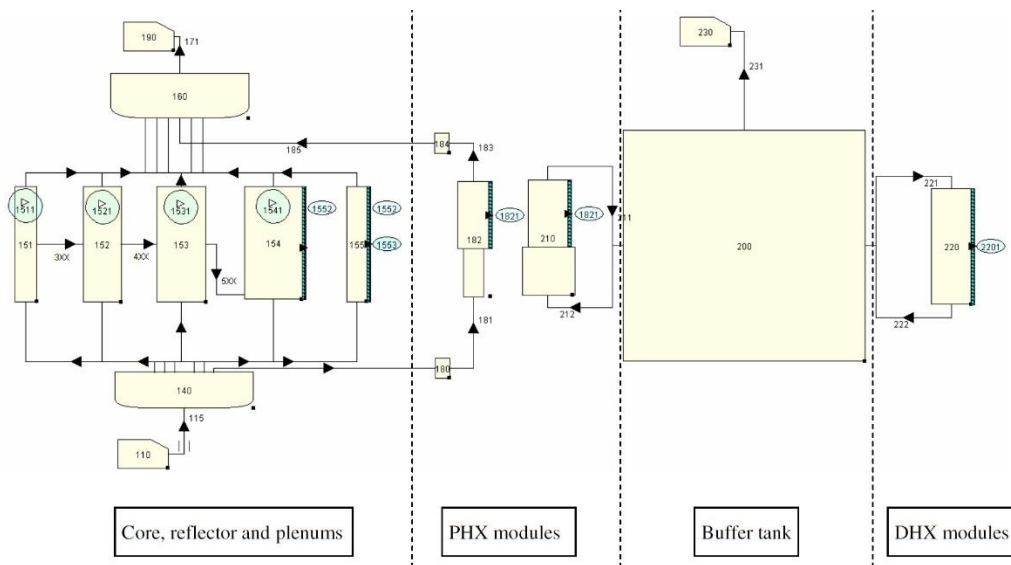
Figure 3-9. Nodalization diagram of the Pb-AHTR RELAP5 model[18]

3.2   Coolant features and thermal-hydraulic correlations

3.2.1   LS-VHTR and AHTR primary coolant: considerations

The effect of the coolant on the core physics was evaluated for the LS-VHTR; this effect is relatively small:

- Due to the excellent thermal properties of salt, the coolant fraction in the core can be relatively small, less than 7%;[14]
- The reference salt option, Flibe, has very small neutron cross sections;[14]

From the perspective of nuclear properties, the salt should have very little parasitic neutron capture and high moderating power. The coolant that best matches these characteristics is Flibe. The fluorine and highly enriched [7]Li have very small neutron cross sections and beryllium is an excellent moderator.

For these reasons the Flibe option has been selected also for the AHTR system, while for the intermediate loop and the safety systems the choice of the salt is dictated mainly by economic reasons.

3.2.2 Flow regime in the AHTR core

During steady-state operation and transients a variety of heat transfer and fluid mechanics phenomena occurs in the reactor core and an accurate description of these aspects needs to be modeled in order to obtain a precise transient response.

Assessing the flow condition of the primary coolant as well as the secondary coolant is important to determine the heat transfer coefficients and so the temperature distribution of the system, in particular the maximum fuel temperature during an accidental transient or the temperature difference between the primary and intermediate side of the DRACS exchanger, which determines the power removed by the safety system.

The AHTR is designed to have a Reynolds number for the intra-assembly channels higher than 5000[6] in order to guarantee a high value for the heat transfer coefficient; in this situation the flow regime is turbulent and the forced convection allows good heat exchange with the core.

When the forced cooling is lost, during an outage or an accident, the Reynolds number decreases and the flow regime enters the laminar or turbulent mixed convection mode.

The heat exchange coefficient is strongly affected by the flow regime and different correlations are implemented in RELAP5-3D for different flow conditions.

3.2.2.a RELAP5-3D correlations for the heat exchange coefficient evaluation

The heat exchange coefficient is calculated by the RELAP5-3D code starting from the Nusselt number:

$$Nu = \frac{hD}{k}$$

(3-1)

Where Nu is the Nusselt number, h is the heat exchange coefficient, D is the hydraulic diameter and k is the thermal conductivity of the coolant.

The calculation of the Nusselt number is performed by the following equation:

$$Nu = \max\left(Nu_{f-lam}, Nu_{f-turb}, Nu_{free}\right)$$

(3-2)

Where the three Nusselt numbers are the forced laminar, forced turbulent and natural convection Nusselt number, respectively.

The following equations are used to calculate each of the three Nusselt numbers:

- Laminar forced connection:

$$Nu_{f-lam} = 4.36$$

(3-3)

- Dittus-Boelter for turbulent forced convection:

$$Nu_{f-turb} = 0.023 Re^{0.8} Pr^n$$

(3-4)

n=0.4 for heating

n=0.3 for cooling

The Dittus-Boelter correlation has been experimentally confirmed for 0.7<Pr<160, Re>6000 and L/D>60.

- Churchill-Chu correlation for free convection:

$$Nu_{free} = \left(0.825 + 0.387 (Gr_d Pr)^{1/6} \left(1 + \left(\frac{0.492}{Pr} \right)^{9/16} \right)^{-8/27} \right)^2 \qquad (3\text{-}5)$$

Some effects are not accounted for in the code, such as entrance effects, laminar-turbulent transition and mixed forced, and free convection, so the evaluation of the heat transfer coefficient in certain conditions is approximated.

3.3 Nuclear reactor kinetics

The point reactor kinetics model is implemented in the RELAP5-3D model in order to describe the variation of the power of the system. This model is based on the following coupled equations:

$$\frac{dn(t)}{dt} = \frac{(\rho(t) - \beta)}{\Lambda} n(t) + \sum_{i=1}^{N_d} \lambda_i C_i(t) + S(t) \qquad (3\text{-}6)$$

$$\frac{dC_i(t)}{dt} = \frac{\beta_i}{\Lambda} n(t) - \lambda_i C_i(t) \qquad i = 1,2,\dots,N_d \qquad (3\text{-}7)$$

$$\rho(t) = \frac{k(t) - 1}{k(t)} \qquad (3\text{-}8)$$

In which t is the time, n is the neutron density [n/m³], C_i is the neutron precursor density in the group i [n/m³], ρ is the reactivity, k is the effective multiplication constant, β and β_i are the total and group precursor yeld, λ_i is the group decay constant [s⁻¹], S is the source rate density [n/(m³*s)] and N_d is the total number of precursor groups.

The reactivity is a function of time, but it can also depend on some of the physical features of the system, such as fuel temperature, coolant temperature and moderator density. To account for this dependence, the term ρ(t) in eq. (3-6) is determined by two components:

- Controlled reactivity insertion, due to control rod insertion;
- Reactivity feedback, which is the variation of reactivity due to the variation of the thermal-hydraulic and physical parameters of the core.

3.3.1 Reactivity feedback

The point kinetics model requires the availability of a reactivity feedback, which is the variation of the multiplicative factor k or the reactivity as functions of the main thermal-hydraulic parameters of the system, that is: temperatures, densities and void fractions.

Assuming a simple linear dependence of the reactivity on the parameters mentioned in the previous paragraph, we can introduce the reactivity coefficients as the slope of these functions. For safety reasons, these coefficients must show some particular trend, in order to avoid the reactor to reach undesired power levels, which could compromise the integrity of the system.

3.3.1.a LS-VHTR coolant void reactivity insertion

A major requirement of any nuclear reactor design is its favorable response to anticipated transients or severe accidents. One common aspect of many accident simulations is the loss of coolant.

Ideally, the coolant void reactivity (CVR) should be negative such that a voiding of coolant will lead to a reduction in reactivity, which effectively shuts down the reactor. Some parametric studies have been performed to evaluate the effect on CVR due to the following:

- Lithium enrichment and fuel burnup;
- Fuel temperature, enrichment and loading;
- Burnable poisons;
- Spectral effect;
- Core geometry (channel dimensions, pitch, clustered rods);
- Flibe molar ratio;

In the initial baseline LS-VHTR, a loss of coolant would lead to a slight reactivity insertion, but through the optimization of the previous parameters this effect can be reduced and controlled. A similar condition is expected for the AHTR.

3.3.1.b Pb-AHTR reactivity feedback calculations

In order to model the reactivity feedback in RELAP5-3D, feedback coefficients are required; the calculation of the reactivity coefficients was performed using MCNP and only the coefficients due to temperature variations of the fuel and the coolant was considered.

Two zones were considered (the fuel and the coolant), with a uniform temperature distribution; the temperatures of the two zones were changed and the k_{inf} variations were observed.

Only the TRISO/pebble heterogeneity level was modeled, in order to have a reasonable computational time; this approximation is reasonable since the neutron leakages from the core should not have a strong dependence on the temperature.

A similar approach will be adopted for the evaluation of the feedback for the AHTR, but a slightly different modeling of the TRISO particle will be implemented.

3.3.1.c AHTR reactivity feedback

Some results are available from ORNL, regarding the reactivity feedback evaluation of the AHTR;[2, 6] the main aspects to be underlined are the following:

- The isothermal coefficient is negative, increases with temperature and the average value is -4 pcm/K (BOC, no BPs);
- The effect of burnable poisons enhances safety, the coefficient becomes more negative;
- The effect of burnup enhances safety, the coefficient becomes more negative and decreases with temperature;
- The void reactivity coefficient can be slightly positive (for particular core configurations), decreases with temperature and the highest value (for low void fraction) is about +0.5 pcm/K.

If the overall temperature coefficient is negative and the potential voiding cannot lead to prompt criticality, a slightly positive void reactivity coefficient might be acceptable.

3.3.2 Reactivity feedback implementation in RELAP5-3D

For the point kinetics model, RELAP5-3D allows two types of reactivity feedback:

- Separable feedback model: the reactivity depends on fuel temperature, coolant density and coolant temperature and each variable is separable (linear dependence of the reactivity on each of the three parameters);
- Tabular feedback model: the reactivity depends on fuel temperature, coolant temperature and density; the reactivity is tabulated as a function of the three variables and linear interpolation is used to calculate the value of reactivity for a given condition.

The second mode was selected for this study, in order to account for eventual non-linear reactivity feedback. The implementation of the tabular feedback model in the RELAP5-3D code is performed through the following equations:

$$r(t) = r_0 - r_B + \sum_{i=1}^{n_s} r_{si}(t) + \sum_{i=1}^{n_c} V_{ci} + R(\bar{\rho}(t), \bar{T}_W(t), \bar{T}_F(t)) \qquad (\,3\text{-}9\,)$$

$$\bar{\rho}(t) = \sum_{i=1}^{n_p} W_{pi}\rho_i(t) \qquad (\,3\text{-}10\,)$$

$$\bar{T}_W(t) = \sum_{i=1}^{n_p} W_{pi}T_{Wi}(t) \qquad (\,3\text{-}11\,)$$

$$\bar{T}_F(t) = \sum_{i=1}^{n_F} W_{Fi}T_{Fi}(t) \qquad (\,3\text{-}12\,)$$

where r_0 is an input quantity that represents the reactivity corresponding to assumed steady-state reactor power at t=0, r_B is the bias reactivity such that $r(0)= r_0$, $r_{si}(t)$ is the input table component, V_{ci} is the control variable contribution, W_{pi} and W_{Fi} are averaging weights for the hydro-dynamic volumes and the heat structures, respectively, ρ and T_W are the coolant density and temperature, T_F is the fuel temperature.

3.4 Power density distribution

3.4.1 Radial power density profile

Since for simple thermal-hydraulic evaluations a 3D neutron kinetics model is not required, the profile of the fission density, which is proportionally related to the power density, must be determined or estimated.

The next paragraphs give a description of the power density distributions calculated from different simulations for the reactor concepts mentioned in the beginning of this chapter.

3.4.1.a LS-VHTR core: neutronic evaluations and power profiles

Parametric studies were performed for the LS-VHTR in order to ensure that the constraint on the fuel enrichment will be met for an assumed target cycle length of 18 months and target discharge burnup greater than 100 GWd/t; the linear reactivity model was used. The cycle length and discharge burnup were evaluated as a function of uranium enrichment, packing fraction, lithium enrichment, and number of batches.
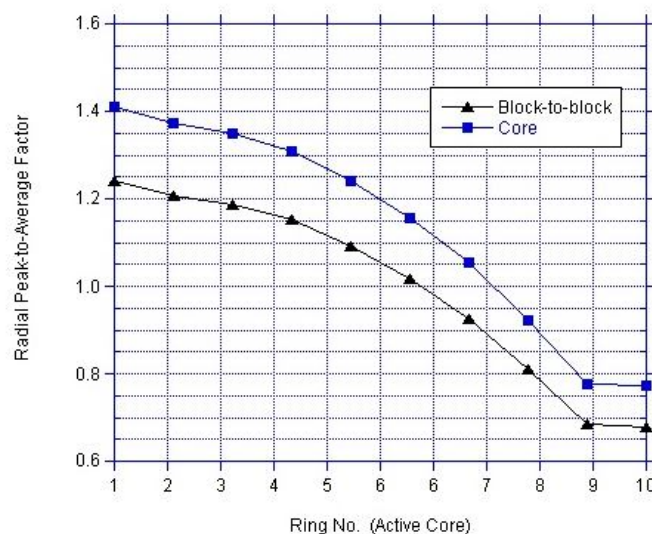
Figure 3-10. Radial relative power density distribution[14]

Radial power distributions were generated using the MCNP code and an explicit 1/12-core model for both a 10-ring and a 9-ring core layout. These distributions were needed to support the thermal-hydraulic and safety analyses. The 10-ring radial power profile is plotted in Figure 3-10 and it gives an idea of a typical radial power density distribution for a molten-salt cooled core.

3.4.1.b AHTR radial power distribution

The radial power distribution has been calculated by ORNL for a 10-ring and 5 axial levels core model performed through the SCALE 6.1 code. The evaluation is at BOL, the enrichment is 19.75% or 9% and the carbon-to-heavy metal ratio (CHM) is 200 or 400; also Eu poisons are used.
In Figure 3-11 radial power profiles are shown, together with the corresponding value of total peaking factor.
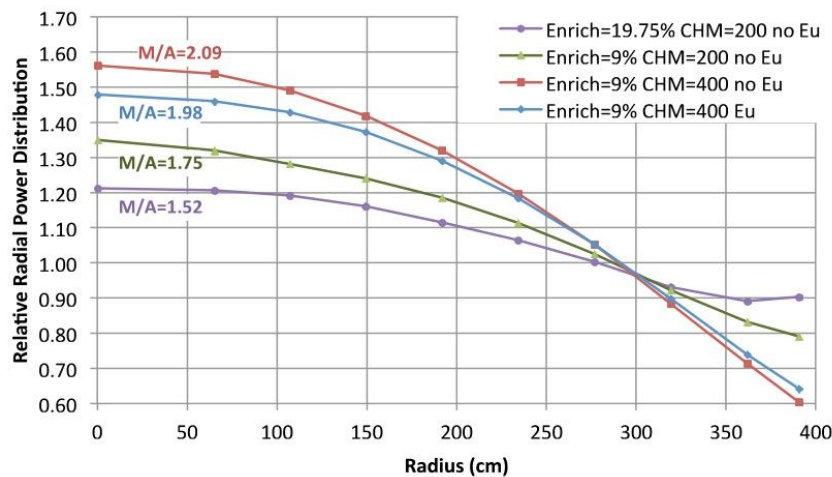
Figure 3-11. AHTR radial power distribution[2]

3.4.2 Axial profile

The axial power profile is expected to be similar to a chopped cosine profile, since the coolant density is almost uniform over the height of the core, but few numerical data are available, so further evaluations in the next chapters will provide an adequate evaluation regarding this aspect.

CHAPTER 4

MODELS AND PRELIMINARY STUDIES

4.1   Mono-dimensional steady-state MATLAB model

A MATLAB model to predict the temperature distribution along the channel and the fuel plate was developed, as a simple tool for preliminary studies. A mono-dimensional approach for the temperature distributions of the coolant and the fuel was used and the steady-state conditions were evaluated.

The following data were assumed, as reference values for the AHTR core:

Table 4-1. Reference parameters of the AHTR core

Parameter		Value	Units
Core thermal power	P	3400	MW
Inlet core temperature	T_{in}	650	°C
Outlet core temperature	T_{out}	700	°C
Specific heat	c_p	2415	J/(kg*K)
Power carried by intra-assembly flow	Pfract	95	%
Number of fuel assemblies	Nassy	252	
Number of fuel plates per assembly	Npl	18	

The specific heat can reasonably be considered constant[9] and the fraction of power carried by intra-flow is approximated at 95 %.[6] From these data it is possible to calculate the mass flow rate:

$$m = P/[c_p * (T_{out} - T_{in})] = 28157 \; kg/s \qquad (4\text{-}1)$$

Of this total mass flow rate only the 95% flows through the intra-assembly channels (5% flows through inter-assembly channels).

Table 4-2. Geometric parameters of the AHTR fuel assembly

Parameter		Value	Units
Flow area of one channel	Ach	15	cm²
Flow area inside one assembly	Ain1assy	279	cm²
Flow area outside one assembly	Aout1assy	135	cm²
Width of coolant channel	T	0.7	cm
Hydraulic diameter of one channel	hdch	1.35	cm
Hydraulic diameter inside one assembly	hdassy	1.16	cm
Hydraulic diameter outside one assembly	hdoutassy	3.46	cm

The geometric parameters of the fuel assembly and the coolant channels are given in section 2.4; neglecting the spacers, the data of Table 4-2 can be calculated from the previous geometric parameters. The average power produced into a single fuel plate is shared among two fuel stripes and is given by the following formula:

$$P_P = P * \frac{Pfract}{Nassy * Npl} = 712.11 \, kW \qquad (4\text{-}2)$$

The mass flow rate for a single channel is given by:

$$\dot{m}_{ch} = \dot{m} * \frac{Pfract}{Nassy * Npl} = 5.8972 \, kg/s \qquad (4\text{-}3)$$

4.1.1 Coolant characterization

The temperature profile of the coolant, as well as other coolant properties, were calculated with respect to the elevation in the core and the following paragraphs present the adopted approach. Given an array of z points, starting at the beginning of the fueled region (z=0 m) and finishing at the end of the fueled region (z=5.5 m), an array containing the fraction of total plate power delivered to every single z interval was calculated. In relation to the axial shape of the power distribution, a simple cosine profile was assumed for this initial evaluation.

This profile was then multiplied by P_p to obtain the power profile for the channel.

The temperature profile was calculated step by step for each z point, adding to the temperature of the previous z value the temperature increase dT_c obtained through the following equation:

$$\dot{m}_{ch} * c_p * dT_c(z) = dP_p(z) \qquad (4\text{-}4)$$

Where $dP_p(z)$ is the power delivered to the coolant in the axial interval located between z-dz and z.

The profile obtained is plotted in Figure 4-1.
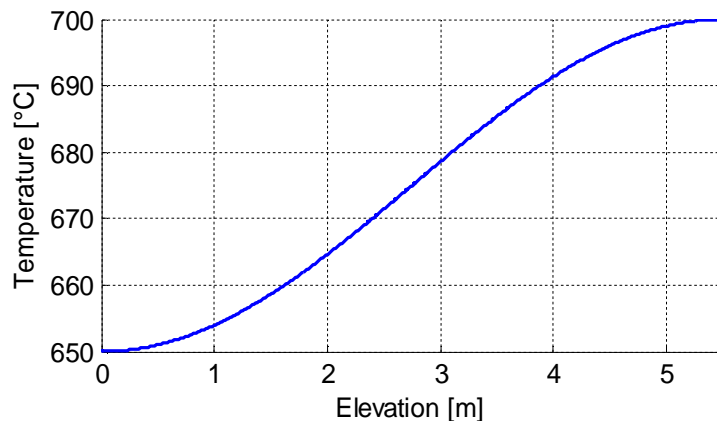
Figure 4-1. Temperature profile of the coolant in the average channel for a cosine axial power density distribution

37

Since the coolant temperature drop across the core is small (50°C), the coolant temperature gradient with respect to the axial direction is small, resulting in an axial conduction heat flux 2-3 orders of magnitude smaller than the transversal convective heat flux.

For this reason, as a first approximation, the contribution of the axial conduction to the energy balance presented in Eq. (4-4) was neglected.

As expected, since the specific heat is constant and the assumed axial power profile is a cosine, the profile has a sinusoidal trend.

4.1.1.a   Thermal-hydraulic coolant features

Other coolant features have been calculated, following the same step by step procedure, for each z interval, through the following passages:

- Once the T_c is calculated at a certain elevation, $\rho(T)$ and $\mu(T)$ can be calculated from eq. (2-5) and eq. (2-6);
- The flow velocity is given by: $v = \dot{m}_{ch}/[\rho * A_{ch}]$;
- The Reynolds number is given by: $Re = \rho * v * hdassy/\mu$; the assembly hydraulic diameter was used because we are interested in the overall pressure drop of the core;
- The Prandtl number is given by: $Pr = \mu * c_p/k$;
- The Nusselt number is given by: $Nu = 0.023 * Re^{0.8} * Pr^{0.4}$ (Dittus-Böelter correlation[6]);
- The convective heat transfer coefficient is given by: $h = Nu * k/hdassy$;
- The friction factor is given by: $f = 4 * 0.000791 * Re^{-0.25}$ (Blasius correlation[6]);
- The pressure drop of the interval is given by: $dp = 0.5 * \rho * v^2 * f * dz/hdassy$;

Some of the previous quantities are plotted in the following figures, as functions of the elevation.
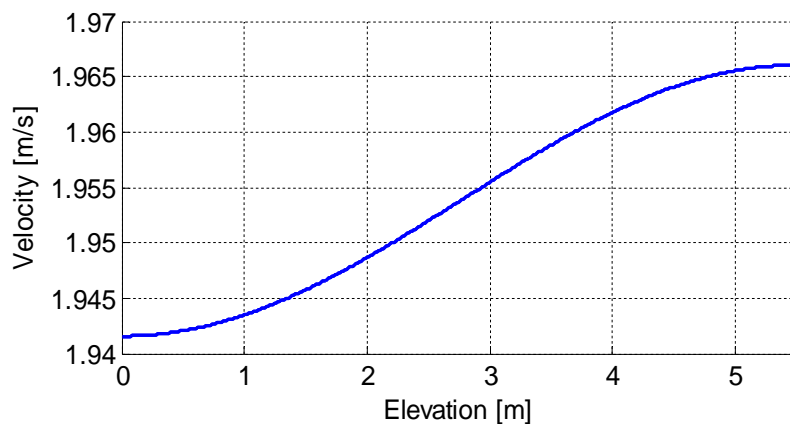
Figure 4-2. Axial profile of the coolant velocity in the average channel for a cosine axial power density distribution
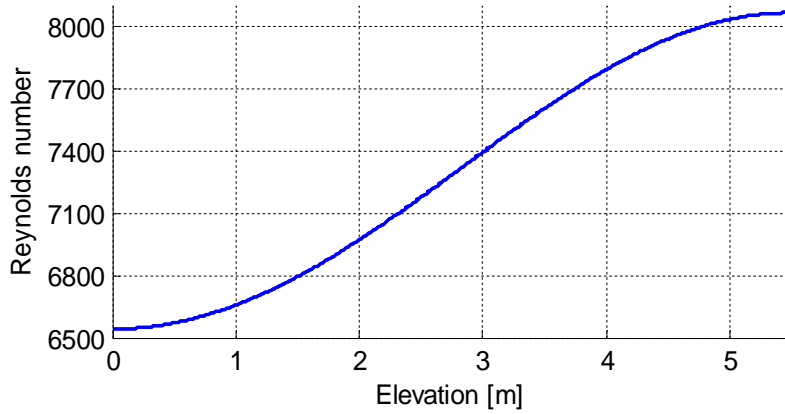
Figure 4-3. Axial profile of the Reynolds number in the average channel for a cosine axial power density distribution
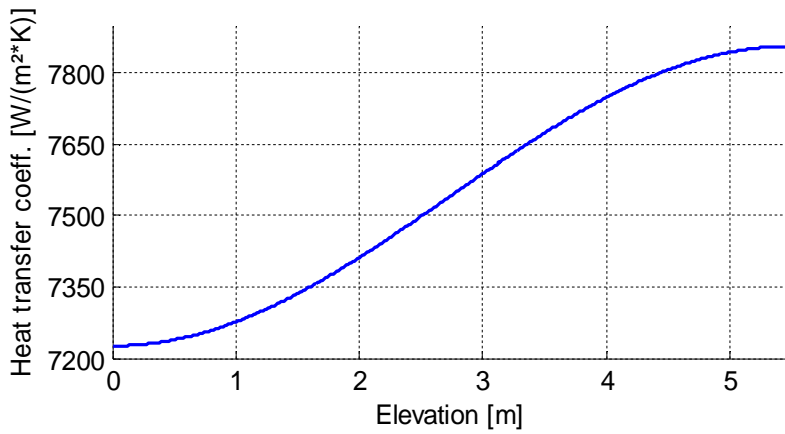
Figure 4-4. Axial profile of the heat transfer coefficient in the average channel for a cosine axial power density distribution
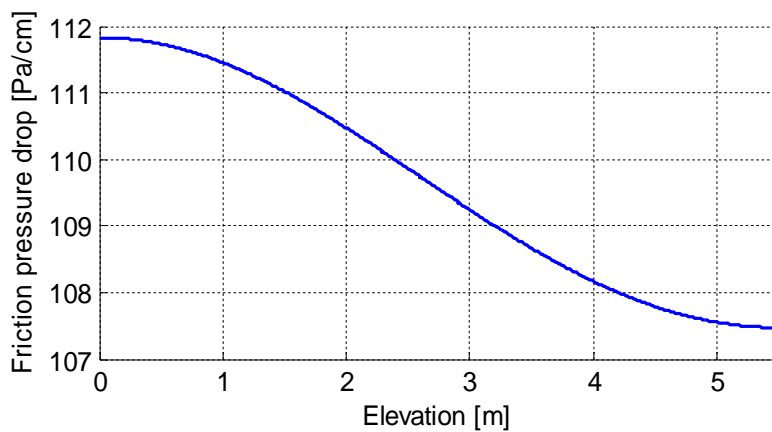
Figure 4-5. Axial profile of the friction pressure drop per cm in the average channel for a cosine axial power density distribution

Figure 4-2 shows that the velocity of the coolant is almost constant along the channel and the average value is 2 m/s; Figure 4-3 shows that the Reynolds number is relatively high (>5000)

39

and increases with the temperature, improving the efficiency of heat transfer (as shown in Figure 4-4).

The pressure drop profile (friction pressure drop per cm, Figure 4-5) shows that hotter FLiBe has lower friction pressure losses than colder FLiBe. The sum of all contributions gives the total core friction pressure drop: $\Delta p = 60279\ Pa = 0.5949\ atm$.

4.1.2   Fuel temperature distribution

For every z point the temperature distribution of the fuel plate was evaluated in the transversal (radial) direction, neglecting the axial conduction. The temperature profile for the coolant, calculated in section 4.1.1, was used as a starting point.

The following data were used as reference for the geometric configuration:

Table 4-3. Geometric and structural parameters of the fuel plate MATLAB model

Parameter		Value	Units
Thickness of the sleeve	ts	1	mm
Thickness of the fuel stripe	tf	6.2	mm
number of sleeve radial intervals	ns	10	-
number of fuel radial intervals	nf	200	-
Packing fraction	PF	40	%
Width of the fuel plate	wp	22.5	cm

The number of sleeve radial points can be increased if non-constant thermal conductivity is used, as in our case (section 2.5.2).

The following coordinate system is used:
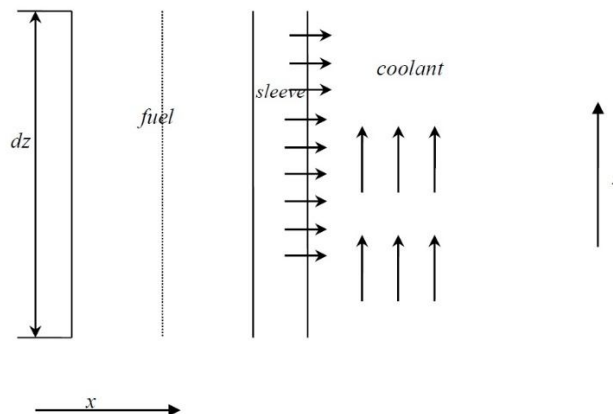
Figure 4-6. Reference frame and model layout for the temperature distribution calculation[6]

Considering the radial direction, from a simple mono-dimensional energy balance and the Fourier law for the heat flux, we have the following equation:

40

$$k(T) * \frac{d^2T}{dx^2} + q''' = 0 \qquad\qquad (4\text{-}5)$$

Assuming the following conditions:

- Fuel thickness equal to tf;
- Constant thermal conductivity k and power density q''';
- Boundary condition: $-k * \frac{dT}{dx}(tf) = q''$ (q'' is the heat flux on the surface between fuel and sleeve);

It can be shown that the temperature drop across the fuel is given by:

$$\Delta T = (q'' * tf - q''' * tf^2/2)/k \qquad\qquad (4\text{-}6)$$

Equation (4-6) allows to approximate the infinitesimal temperature drop dT across an infinitesimal length dx (in which q''' and k can be reasonably considered constant) through the following equation:

$$dT = (q'' * dx - q''' * dx^2/2)/k \qquad\qquad (4\text{-}7)$$

4.1.2.a   Calculation of the fuel temperature distribution

The axial power profile is the same profile used for the evaluation of the coolant temperature (section 4.1.1), but it is divided by a factor 2, since the power is shared between two fuel stripes. Each power value was divided by the heat exchange surface of the single interval, in order to obtain q''(z), which is the surface heat flux.

The q'''(z) is obtained simply by dividing the q''(z) by tf: for the initial case a uniform power density distribution was assumed for the radial direction, and no power generation was used for the coolant, the graphite sleeve and meat.

For each z point:

- The surface temperature was calculated as:

$$T_s(z) = T_c(z) + q''(z)/h(z) \qquad\qquad (4\text{-}8)$$

- For each radial step of the sleeve, k was calculated using the previous step's temperature and the temperature increment was obtained through Eq. (4-7), with q'''=0;
- For the fuel stripe, the same procedure was used, but with the q''' previously calculated, k scaled by a factor φ (equation (2-1)) and q'' varying with x (q'' must be the thermal flux as the right boundary of the volume, so it decreases with r decreasing, that is with step number increasing).

In Figure 4-7, radial temperature profiles for different core levels are plotted for the average assembly; z=300 cm corresponds approximately to the elevation at which the temperature reaches the maximum value (cyan line).
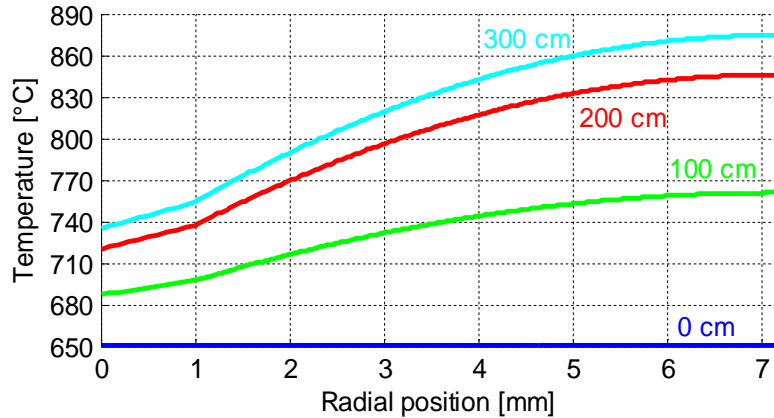
Figure 4-7. Transversal temperature profiles for different elevations in the average channel for a cosine axial power density distribution

The maximum fuel temperature is about 875°C, but we must take into account that the full cosine profile for the axial power density is probably not a good representation of the real power distribution, so we expect the real maximum temperature to be lower.

In Figure 4-8 the temperature distribution of the plate is plotted; the radial coordinate goes from 0 mm, which is the surface of the plate, to 7.2 mm, which is the inner surface of the fuel stripe (the graphite meat is neglected, since, with no power production, the temperature profile would be constant). The maximum temperature is located slightly above the mid-plane, corresponding to z=2.75 m, but we expect, with a more realistic (lower) axial peaking factor, the maximum to be lower and located at higher core elevation.
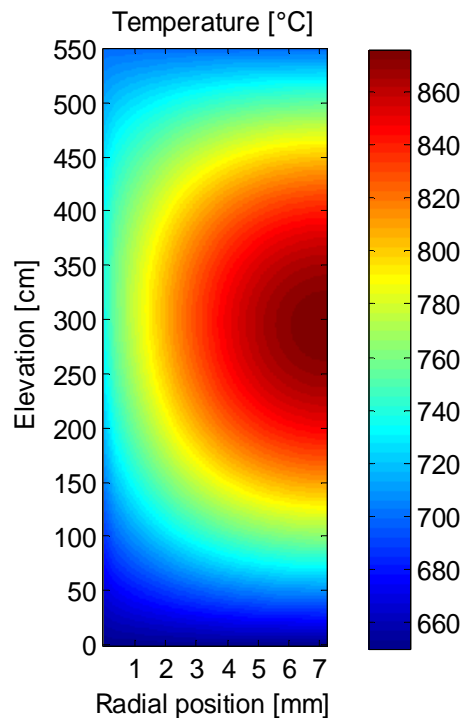
Figure 4-8. Temperature distribution of the fuel plate for a cosine power density profile in the average channel for a cosine axial power density distribution

42

4.1.3   Steady state operation and constraints

The reference steady state conditions for the average assembly are calculated assuming an axial power density distribution with a 1.3 peaking factor, as explained in section 4.3.1; the results obtained from the MATLAB model are shown in Table 4-4, with the respective limitations.

Table 4-4. Steady-state parameters and constraints[6] for the single-channel MATLAB model

Parameter	Value	Limit	Units
Fuel maximum temperature (average assembly)	843	<1000	°C
Fuel maximum temperature (hottest assembly)	951	<1250	°C
Average flow velocity	1.95	<3.00	m/s
Average Reynolds number inside assembly	7291	>5000	-
Friction pressure drop across the core	0.5949	<1.5	atm

Similar results are reported from ORNL for flow velocity, Reynolds number and pressure drop;[6] There are some differences in temperatures, since ORNL considered a bare cylindrical reactor (full cosine profile in the axial direction), while a chopped cosine profile was considered in this work; however, the difference is relatively small, since a lower average thermal conductivity of materials was implemented in the MATLAB model, leading to higher temperature profiles. The results show that the fuel assembly configuration of the AHTR is capable to fulfill all the main thermal-hydraulic requirements.

4.2   Neutronic evaluations: SCALE model

The neutronic evaluations are performed through the KENO-VI 3-D Monte Carlo code for nuclear criticality safety analyses, which is part of the SCALE (Standardized Computer Analyses for Licensing Evaluation) code system.

A SCALE model of the fuel assembly was developed in order to calculate the power density distributions and the reactivity feedback, needed as an input for the RELAP5-3D core model.

Two main fuel assembly designs have been proposed and studied by ORNL:[2, 6]

- The 2011 design has 19.75% enriched fuel and 32.91 MT of heavy metal loaded into the core; this results in a ~6 mm thick fuel stripe;
- The 2012 design has 9% enriched fuel and 17.48 MT of heavy metal loading into the core; the fuel stripe is thinner, about 2.5 mm.

Both of the two configurations have been considered for the evaluation of the feedback, but the 2011 case was selected for other purposes and evaluations.

4.2.1 Geometric configuration of the model

4.2.1.a Fuel assembly SCALE model configuration
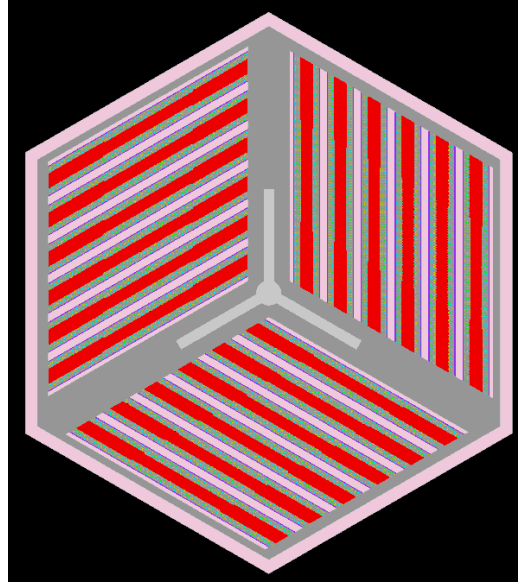
Figure 4-9. Cross-section of the SCALE fuel assembly model (Red and dark gray = graphite; light gray = void; green = fuel stripe; pink = FLiBe)

This section presents the structural and dimensional features of the model, mainly with reference to the initial (2011) AHTR design.[6] The geometric configuration does not change with respect to the elevation (z coordinate), so the cross-section views shown in the next pictures refer to the horizontal (x-y) plane.

Figure 4-9 shows a cross-section view of the SCALE assembly model.

The main dimensions and characteristics of the model, used for the reactivity feedback evaluation, are presented in Table 4-5.

Table 4-5. Main parameters of the fuel assembly SCALE model for the reactivity feedback evaluation

Parameter	Value	Units
Number of plates	18	-
Thickness of Y-shaped support	4	cm
Thickness of the control blade channel	1	cm
Thickness of the wall	1	cm
Thickness of the intra-assembly channel	7	mm
Thickness of the inter-assembly channel	0.875	cm
Height	10	cm
Boundary conditions	all reflective	-

The main dimensions of the fuel assembly are still the same for the 2012 core design; the only difference can be found in a thinner fuel stripe, as it is explained in section 4.2.1.b.

4.2.1.b   Fuel plate SCALE model configuration

The fuel plate configuration is shown in Figure 4-10 and Figure 4-11.
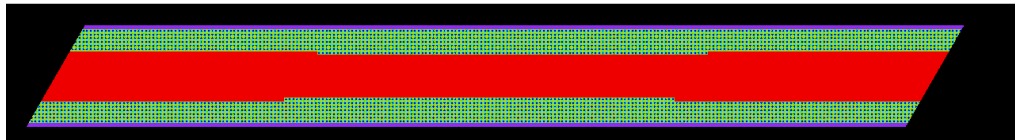
Figure 4-10. Fuel plate SCALE model configuration
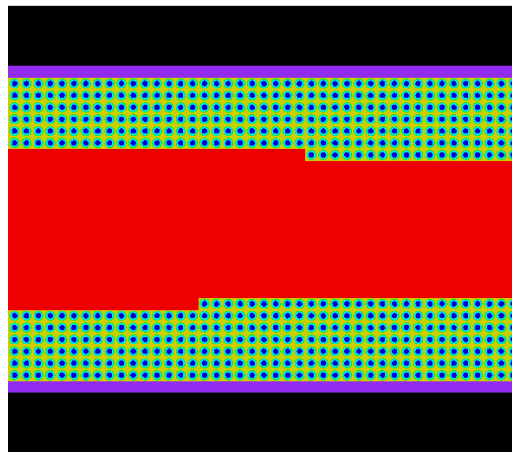
Figure 4-11. Enlarged view of the fuel plate SCALE model

The total plate thickness is 2.55 cm and the active width is 22.11 cm; the graphite sleeve thickness is ~1mm and the thickness of the fuel stripe is about 6 mm where the fuel stripe has six layers and about 7 mm where the fuel stripe is thicker (in the middle of the stripe: 7 layers). The 2012 design differs from the 2011 case in that the fuel stripe into the plate is thinner, since the heavy metal loading of the core is substantially lower; a plot of the 2011 plate model cross section is shown in the next figure.
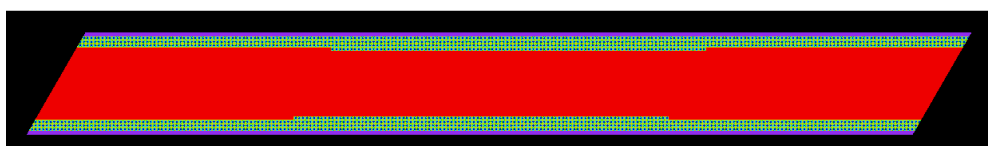
Figure 4-12. Fuel plate SCALE model configuration for the 2012 core design

4.2.1.c   TRISO particle and lattice configuration

Figure 4-13 shows the TRISO particle, the lattice and the main dimensions of the SCALE model of the fuel stripe.
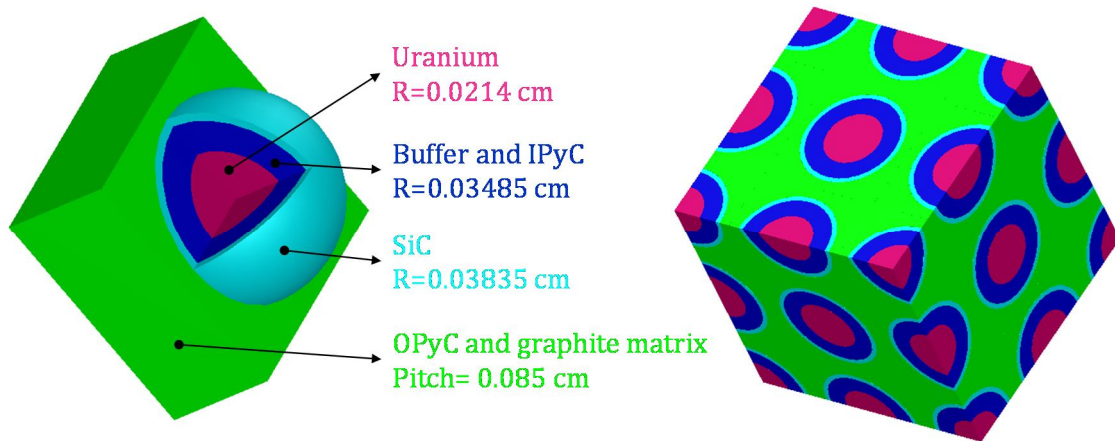
Figure 4-13. TRISO particle and lattice configuration in the SCALE model

The configuration presented in Figure 4-13 assumes a 40% packing fraction, which is the highest value that can be reliably obtained with currently available technologies.

A simple cubic lattice is implemented, even if a real TRISO fuel would probably present a random distribution of particles; we expect this issue to be negligible in relation to the purposes of this work.

A second approximation was adopted, which consists in the homogenization of the buffer layer with the inner pyrolitic carbon layer and the outer pyrolitic carbon layer with the graphite matrix.

4.2.2   Multigroup model

The evaluation of the reactivity was performed through the 3D Monte Carlo transport code implemented in SCALE (KENOIV).

The evaluation of the nuclear cross sections is required in order to calculate the reactivity of the fuel assembly and two options are available for the KENO model, the continuous energy library (ce_v7) and the multigroup library (v7-238).

Since no approximations for the cross-section evaluation are performed in the continuous energy mode, this would be the preferable solution, but the ce_v7 library gives cross-section functions only for few discrete temperature values (tipically 600K, 900K and 1200K) and SCALE does not allow cross section interpolation in the continuous energy mode.

So the multigroup mode was selected and the Dancoff factor for the TRISO particles was optimized through a comparison with the continuous energy model calculation.

The following procedure was used to estimate the Dancoff factor:

- A certain temperature distribution was selected, so that the cross sections were available both for the continuous energy and multigroup model;
- The continuous energy model was run; the multigroup model was also run with several different values for the Dancoff factor, within the expected range;
- The k resulting from the continuous energy model was interpolated into the fit of the multigroup results and the Dancoff factor was determined.

The results for the 2011 core design are shown in the next plots; the multigroup results are interpolated through a quadratic fit.
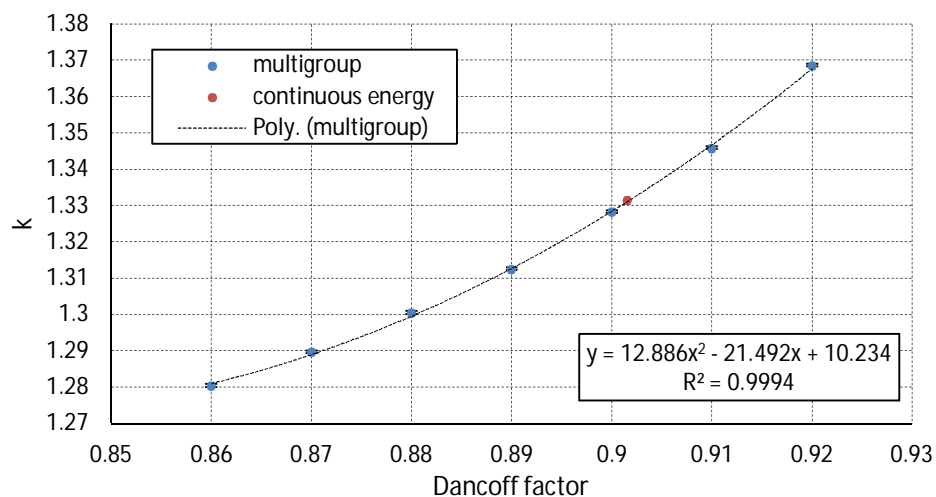
Figure 4-14. Dancoff factor interpolation for the multigroup model of the 2011 design

The same procedure was used for the 2012 case. The Dancoff factor obtained from the interpolation was used for the calculation of the reactivity feedback and the power distributions; for the 2011 case the obtained Dancoff factor was 0.90156, while for the 2012 thinner fuel stripe, the Dancoff factor was 0.88179.

4.2.3   Reactivity feedback

Two contributions to the reactivity feedback are evaluated in this work: the temperature of the fuel and the temperature of the coolant; a variation of the coolant temperature results also in a variation of the coolant density, so even the coolant density variation is accounted for in this modeling.

The evaluation of the reactivity feedback is performed trough the following steps:

- Selection of the range of fuel and coolant temperature variation;
- Calculation of the k for each possible set;
- Calculation of the reactivity for each point as (k-1)/k;
- Calculation of the reactivity coefficient as the slope of the interpolating line.

4.2.3.a   Reactivity feedback for the reference core design

The reactivity feedback was evaluated for the 2011 reference core design; the results are presented in the following paragraphs.

In order to calculate the reactivity feedback, the following range of temperatures was selected: from 900 K to 1100 K with a 100 K step for the coolant, from 900 K to 1500 K with a 100 K step for the fuel; for each possible combination the k was calculated and the results are shown in Table 4-6 and Figure 4-15.

Table 4-6. k-inf and uncertainty results for the 2011 reference design

k	Coolant temperature [K]			Uncertainty	Coolant temperature [K]		
	900	1000	1100		900	1000	1100
900	1.35466	1.35378	1.35281	900	0.0001	0.00012	0.00014
1000	1.34558	1.34485	1.34372	1000	0.00011	0.00011	0.00013
1100	1.33788	1.33691	1.33589	1100	0.00012	0.00011	0.00011
1200	1.33059	1.32988	1.32891	1200	0.00011	0.00012	0.00015
1300	1.32246	1.32149	1.32039	1300	0.00011	0.00015	0.00011
1400	1.31500	1.31382	1.31283	1400	0.00011	0.00011	0.00011
1500	1.30807	1.30705	1.3062	1500	0.0001	0.00012	0.00012

(Fuel temperature [K] labels the rows on the left side of each sub-table.)
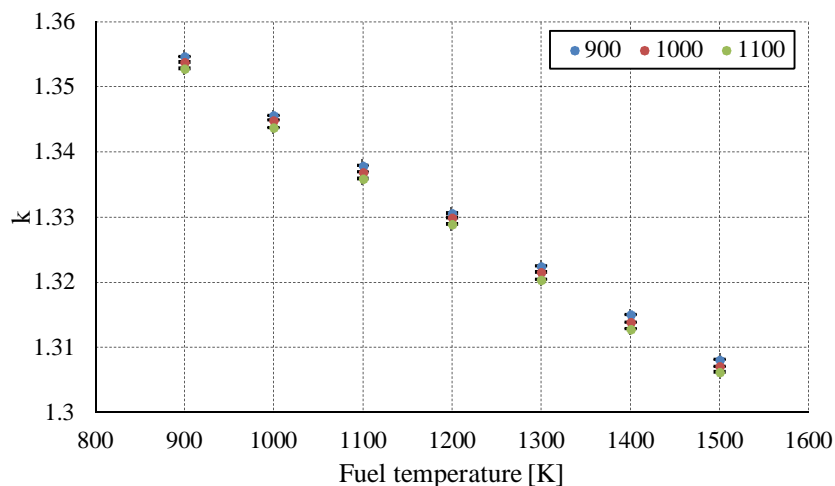
Figure 4-15. k-inf and uncertanty results for the 2011 core design

In relation to Figure 4-15, it is clear that the k-inf, and so the reactivity, depends mainly on the fuel temperature, while coolant temperature and density play a smaller role. We could expect

this, since the amount of coolant, in terms of volumetric fraction, into the core, is small, of the order of 10%. The reactivity insertion due to the increase of the coolant temperature is negative, providing adequate safety features for the power control.

From the k-inf values it is possible to calculate the reactivity of the system; the results are shown in the next table.

Table 4-7. Reactivity [pcm] for the 2011 reference design, as a function of fuel and coolant temperature

Reactivity [pcm]		Coolant temperature [K]		
		900	1000	1100
Fuel temperature [K]	900	26181	26133	26080
	1000	25683	25642	25580
	1100	25255	25201	25144
	1200	24845	24805	24750
	1300	24383	24328	24265
	1400	23954	23886	23829
	1500	23551	23492	23442

The reactivity shows an almost linear dependence on the two temperatures; the reactivity coefficients can be obtained by dividing the reactivity variation by the temperature increase for each step. The next figures show how the coefficients depend on the fuel and coolant temperature.
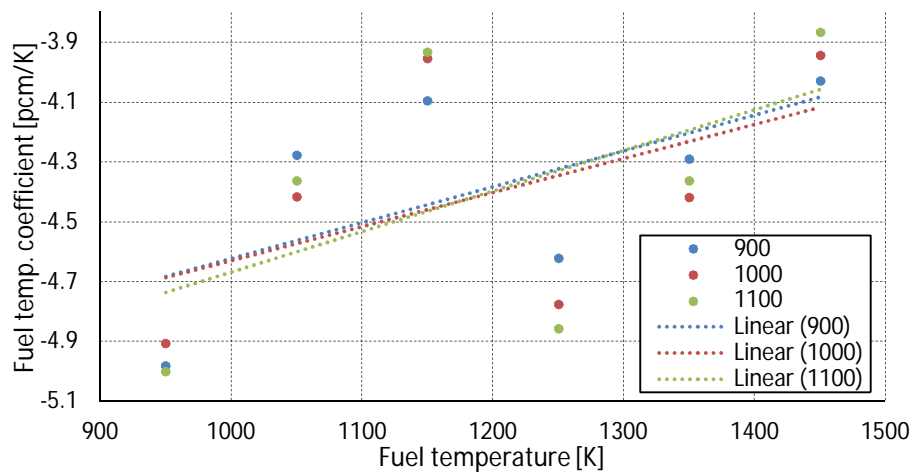
Figure 4-16. Fuel temperature reactivity coefficient for the 2011 reference case

In reference to Figure 4-16, we can see that for the beginning-of-life fuel configuration the coolant temperature reactivity feedback is negative with an average value of -4.5 pcm/°C and tends to become smaller (absolute value) when the fuel temperature increases.

Considering the coolant temperature reactivity feedback (Figure 4-17), the average value is negative, about -0.5 pcm/°C, and the temperature dependence is not clear. The coefficient is positive but it is relatively smaller than the fuel temperature coefficient.
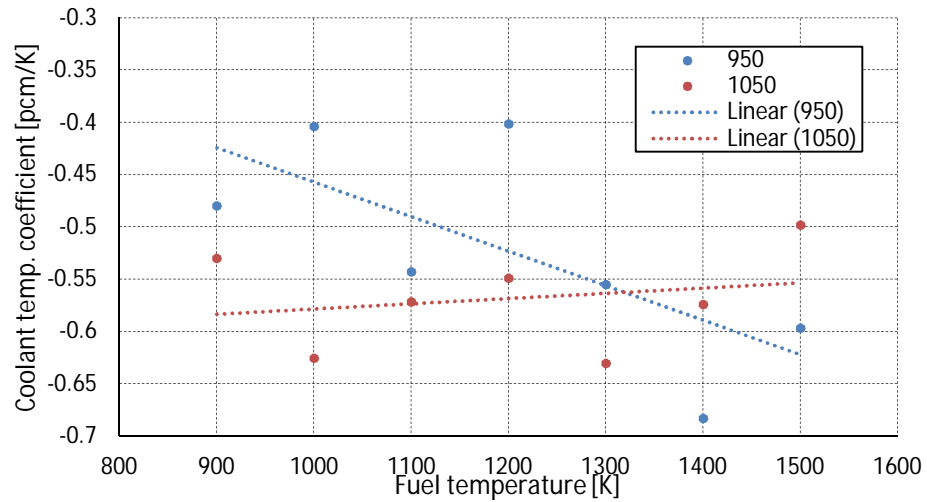
Figure 4-17. Fuel temperature reactivity coefficient for the 2011 reference design

4.2.3.b   Reactivity feedback for the low heavy metal loading core design

The reactivity feedback was evaluated for the 2012 AHTR design (low heavy metal loading design), using the same procedure presented in section 4.2.3.

The fuel temperature coefficient for the 2012 case is similar to the 2011 case; the average value is about -4.0 pcm/K and an increase in the fuel temperature makes the absolute value of the coefficient smaller.
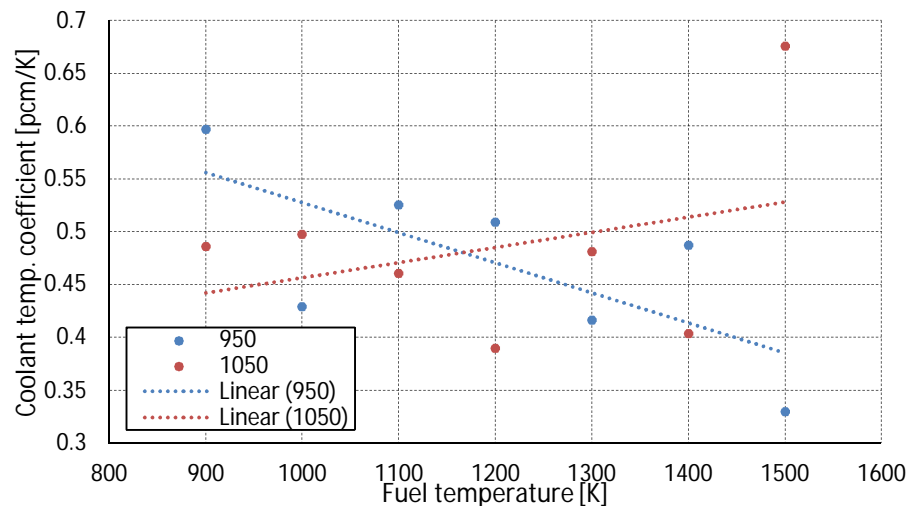
Figure 4-18. Fuel temperature reactivity coefficient for the low heavy metal loading design

The main difference with respect to the 2011 design is the value of the coolant temperature reactivity coefficient, which is small but positive, with an average value of +0.5 pcm/K, as we can see in Figure 4-18.

The reactivity insertion due to increasing coolant temperature is small but positive, so this could lead to safety issues, in case the reactivity insertion due to partial or total core voiding would make the system prompt critical. Anyway, since the coolant temperature coefficient is small and the fuel temperature coefficient is large, the overall power coefficient is negative and we expect the safety of the reactor not being compromised.

4.3   Power density distribution

The characterization of the power density distribution is a fundamental aspect of the core modeling. This section presents the evaluation of the power density distribution with respect to the axial direction and within the fuel stripe, performing the analysis at the fuel assembly level. The radial power distribution would require a full core model for neutronics, which is strongly demanding in terms of computational capabilities; for this reason, the data provided by ORNL[2] was assumed for the radial power profile modeling.

4.3.1   Axial power density distribution

The model developed with MATLAB was used to determine an approximated value for the extrapolated length of the power density profile. This profile is cosine-shaped, but the cosine is chopped at the beginning and at the end of the fueled region of the plate (in the axial direction).
As a reference value we can use a peaking factor of 1.3, which is a reasonable value for the beginning of life of a fresh LSCR core.
In Figure 3-11 we can see radial power profiles for different enrichments, BPs loading and CHM, obtained through a 10-rings core simulation.
For the 4 curves, we can see the radial peaking factor and the associated value of total peaking factor; the axial peaking factor can be obtained by dividing the total peaking factor by the radial factor; the values are shown in the next table:

Table 4-8. Peaking factors for different radial power density profiles

curve:	red	blue	green	purple
total peaking factor	2.09	1.98	1.75	1.52
radial peaking factor	1.56	1.48	1.36	1.21
axial peaking factor	1.34	1.34	1.29	1.26

A 1.3 value for the axial peaking factor is a reasonable assumption, even if in some studies for LS-VHTR[14] a value of 1.4 was used.

The initial peaking factor will decrease as the fuel is burned, so this configuration is representative of a fresh core and the maximum fuel temperature calculated in these conditions represents the maximum fuel temperature of all core's life, if the variation of other parameters, such as fuel conductivity, can be neglected.

The effect of the extrapolated length variation on the fuel assembly thermal hydraulic features was evaluated; Figure 4-19 shows the centerline temperature profile of the average fuel assembly and Figure 4-20 shows the coolant temperature profile of the average assembly.
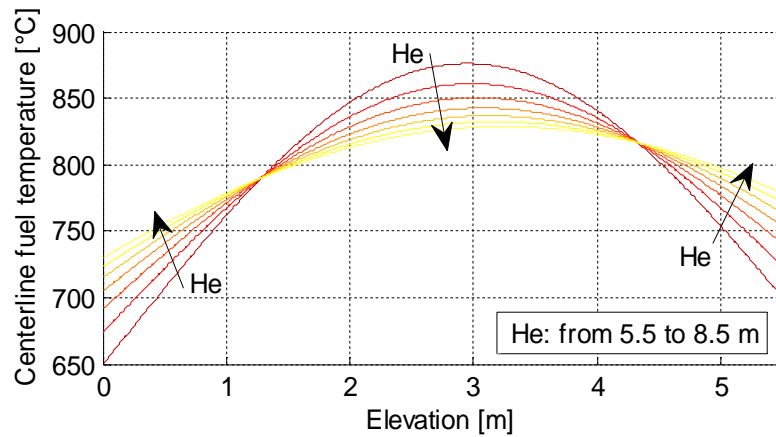
Figure 4-19. Centerline temperature profile for different values of extrapolated length He
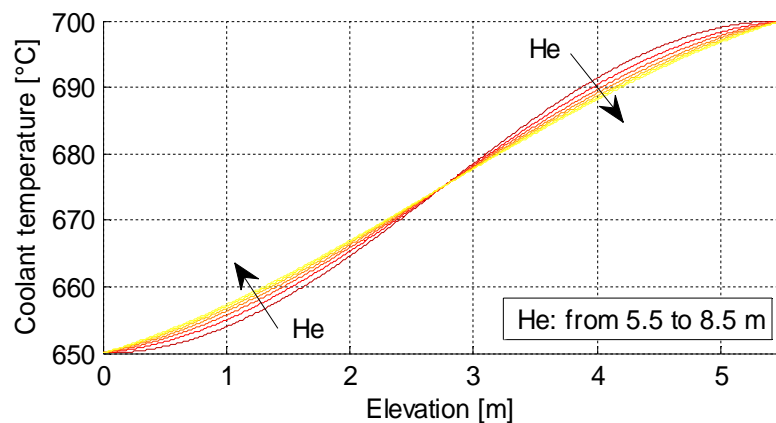
Figure 4-20. Coolant temperature profiles for different values of extrapolated length He

As we can see from Figure 4-19, the temperature profile is strongly affected by the extrapolation length, in both the position and the value of the maximum temperature; for small He the maximum temperature is located around the middle of the core, while for higher He values the elevation of the maximum increases and the value decreases.

Figure 4-20 shows that the temperature profile of the coolant is not strongly affected by the shape of the power profile; decreasing the peaking factor, the temperature profile goes from a sinusoidal shape to a straight line.

In the next Figure 4-21 the maximum temperature and peaking factor are plotted as functions of the extrapolated length He.
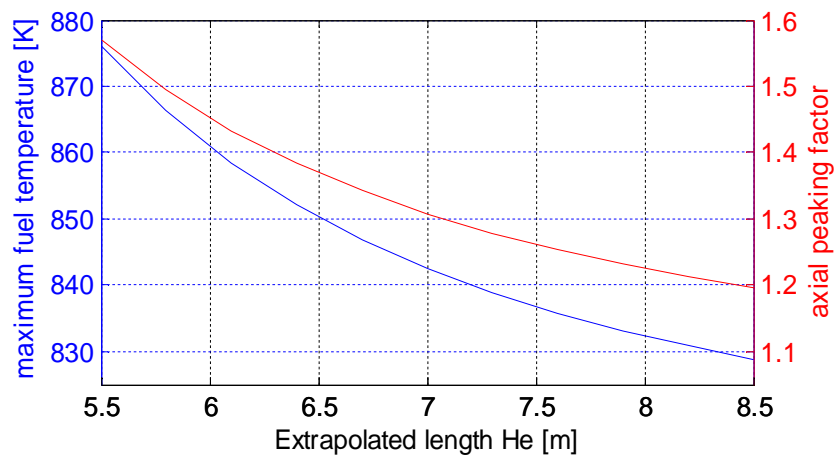
Figure 4-21. Maximum fuel temperature and radial peaking factor as functions of the extrapolated length He

In order to obtain a value of 1.3 for the peaking factor an extrapolated length of 7 m (1.5 m longer than the active height of the fuel, which is 5.5 m) must be selected.

The maximum fuel temperature of the average assembly decreases from 880°C (full cosine profile) to 845°C, when He is set to 7 m.

It can be shown that other parameters, like mean velocity, mean heat transfer coefficient and total pressure drop, are not affected by the value of extrapolated length.

For the previous reasons an extrapolated length He equal to 7 m was selected for the following studies in this work.

4.3.1.a   Evaluation of the axial power density distribution: SCALE model

The same SCALE model used for the reactivity feedback calculations was used as a starting point for the evaluation of the axial power density distribution. Ten axial intervals were defined and for each of these intervals the geometry and the materials were modeled; a block of reflector material and a block of FLiBe were added at the top and the bottom of the active height of the assembly. The boundary conditions were set all reflective, except the lower and upper faces of the structure, and the temperatures of the materials were set as in the average fuel assembly (data obtained from the RELAP model).

Figure 4-22 shows the normalized axial power density profile obtained from SCALE and its interpolation with a cosine function. The interpolation function has an extrapolated length of 9.1 m and a peaking factor of about 1.2. The values used for other simulations are 7 m and 1.3, respectively, so the peaking factor from SCALE is lower. Anyway, the use of a higher peaking

factor is acceptable since the maximum temperatures obtained would be more conservative from a safety standpoint.
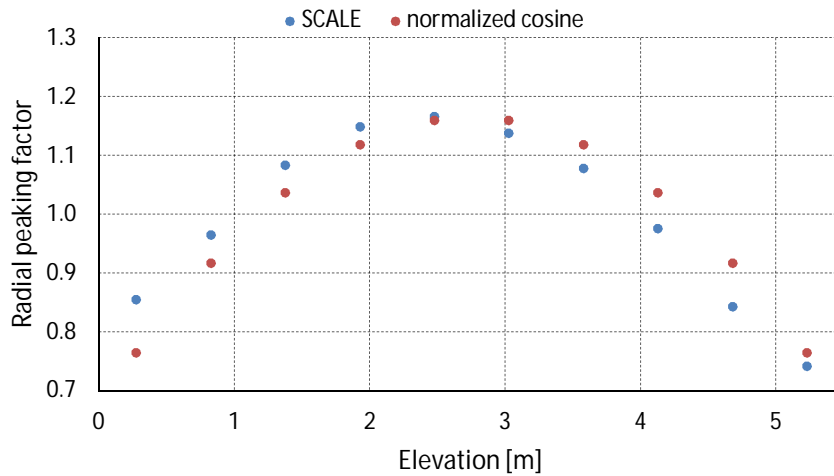
Figure 4-22. Normalized axial power density profile

4.3.2   Transversal power density distribution in the fuel stripe

The variation of power density distribution can affect the temperature profile in the direction transversal to the plate and also the value of the maximum fuel temperature. Some evaluations were performed in order to understand the effects of transversal power distribution variation.

The model used is the same MATLAB channel model used for preliminary calculations (but with a chopped cosine axial power profile and an extrapolation length equal to 7 m, as presented in the previous section); this model was slightly modified to take into account the fact that the transversal (with respect to the plate) power density profile is not uniform.

The axial profile is unchanged, which means that for each axial interval the total power produced in that volume is still the same, but it has a different transversal distribution; this transversal distribution is the same for each axial interval.
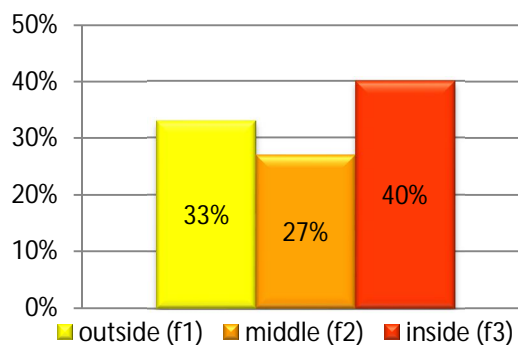
Figure 4-23. Example of power density distribution (3 layers of fuel stripe)

54

The transversal distribution was obtained by dividing the fuel stripe thickness into three equal intervals in which the power density is uniform and by giving, for each of these intervals, a relative factor used to determine the value of power density; an example of power distribution is given in Figure 4-23

In this condition we have that the three relative factors are equal to:

- 33% for the outside transversal interval of the fuel stripe (the one near to the sleeve);
- 27% for the middle interval;
- 40% for the inside interval (the one in contact with the graphite meat);

The sum of the three factors is 100%, which means that the total power delivered at a certain elevation of the plate is the same as in the uniform profile case, but the amount of power produced may be different from one radial segment to another.

We changed the three factors to give the desired shape to the transversal power profile.

In Figure 4-24, temperature profiles for different values of outside relative factor (f1) are plotted (f2 and f3 are equal).
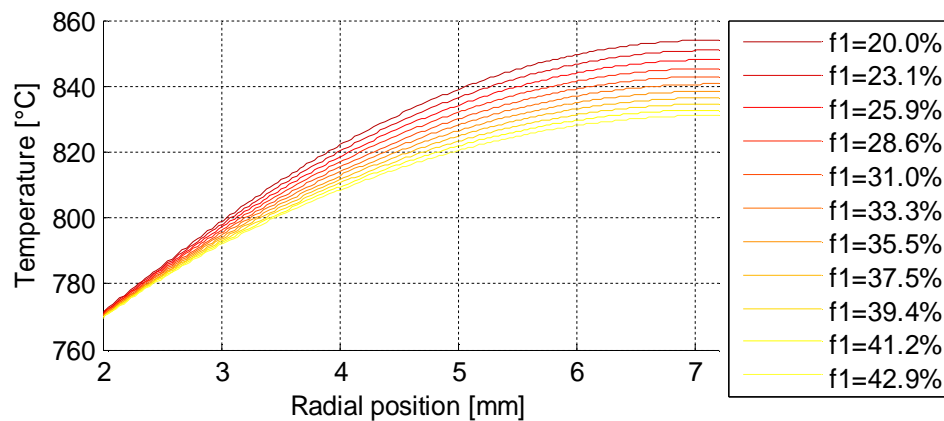
Figure 4-24. Radial temperature profile (at z=2.75 m) for different values of f1
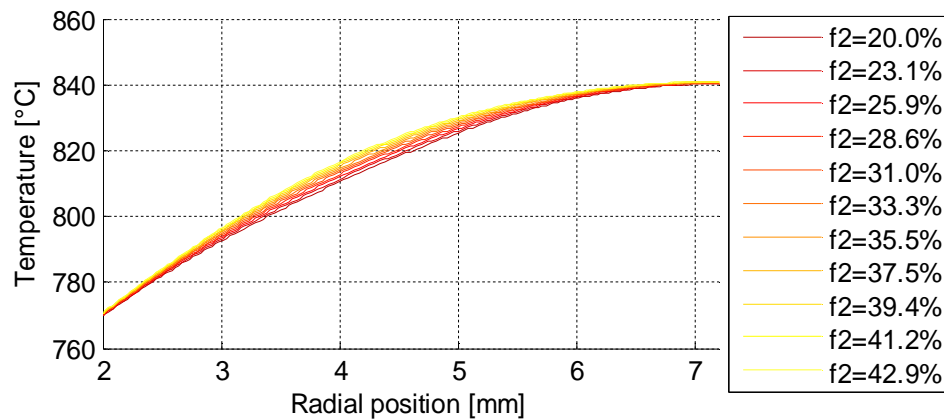
Figure 4-25. Radial temperature profile (at z=2.75 m) for different values of f2

The value of z at which the calculation is performed is not relevant, since we are interested in the radial temperature profile, but we decided to choose z=2.75 m (half the active height of the core) because, as we saw from preliminary calculations, the point of highest temperature within the fuel plate is not far from the mid-plane. As we can see from the previous plot, the shape of the profile does not change but the maximum temperature decreases from 855°C to 830°C (25°C variation) when f1 increases from 20% to 43%; the reason of this behavior lays in the fact that if f1 increases, higher power density is located closer to the coolant channel and so the plate can be more easily cooled.

The same analysis for the f2 factor gives the results presented in Figure 4-25.

Figure 4-25 shows that the maximum temperature does not depend on the relative factor f2: this is due to the fact that in this configuration while the power density changes, the average distance of power source distribution from the cooled surface does not change.

The temperature profile slightly changes: for high values of f2 the temperature in the middle of the fuel stripe increases of some degrees.

Finally, we can see the results for the variation of f3 in the next figure.
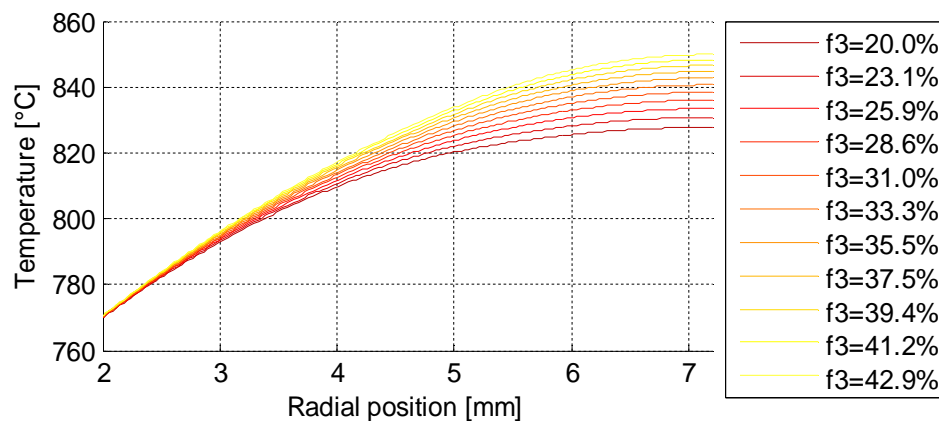
Figure 4-26. Radial temperature profile (at z=2.75 m) for different values of f3

We can see that the maximum temperature has a similar behavior to the f1 case, as well as the temperature profile.

Since the total power per axial interval is constant we have that the three factors f1, f2 and f3 are not independent, so we can neglect for example f1 and change the other two factors in order to understand how the maximum temperature variation depends on the power distribution. In Figure 4-27 the maximum temperature is plotted as a function of f2 and f3.

The temperature dependence from f2 and f3 is relatively weak: if we consider reasonably small variations of the power density distribution (increase of both factors by 5%), we find that the maximum temperature has a small variability range, about 10°C. Moreover, the contour lines can be approximated by straight lines and, for a given value of f1 (that is: for a given value of the sum

of f2 and f3), it is better to have f2 high and f3 low: this means that the plot (as we can see in Figure 4-27) is not symmetric with respect to the bisector.
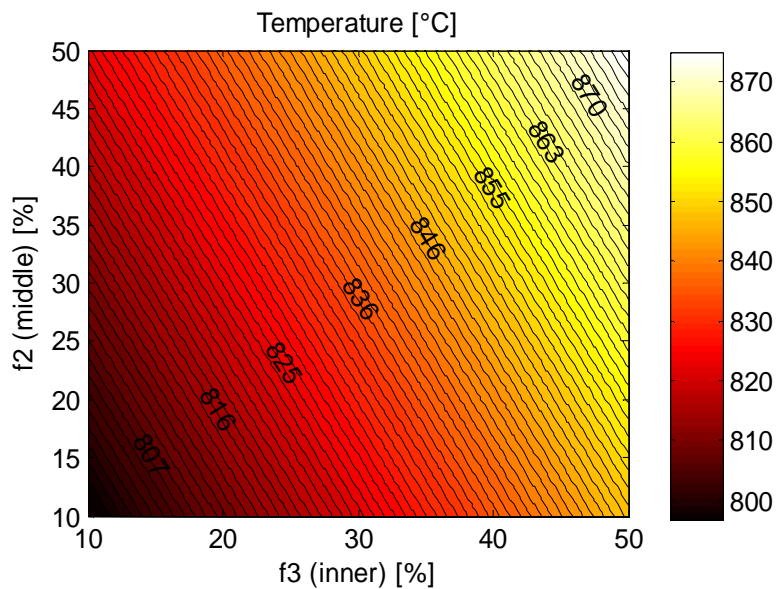
Figure 4-27. Maximum temperature of the fuel as a function of factors f2 and f3

A comparison was made between the case in which the power is uniformly distributed and a case in which the power has the profile shown in Figure 4-23.

The reference power density is the outside interval power density (33%, that is 1/3); the middle power density was set to 27% to account for the thermal neutron shielding by the outside and inside layers; the inside power density was set to 40% to account for the excess of moderation due to the inner graphite meat.

The radial temperature profile is shown in Figure 4-28.
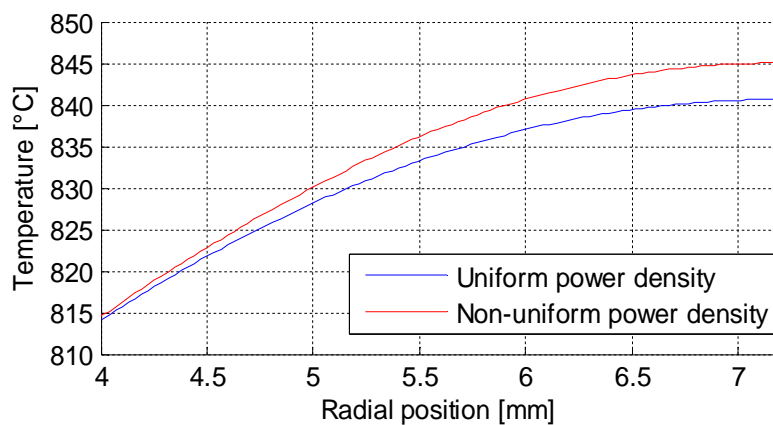
Figure 4-28. Transversal temperature profile for uniform and non-uniform radial power distribution at z=2.75 m

The non-uniform distribution leads to higher temperatures, but the difference is small: up to a depth of 4 mm from the plate surface the two profiles are similar and the maximum difference (at the inner surface of the fuel stripe) is less than 5°C.

4.3.2.a Evaluation of the transversal power density distribution: SCALE model

The SCALE model of the fuel plate, presented in section 4.2.1.b, was adapted for the evaluation of the transversal power density distribution; Figure 4-29 shows a cross section of the model.
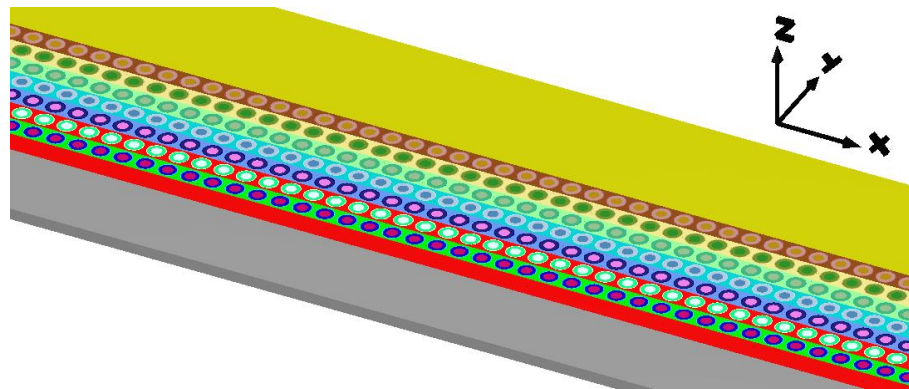
Figure 4-29. SCALE model for the transversal power profile calculation

The model presented in Figure 4-29 is symmetric with respect to the x and z directions; the structure of the model varies only with respect to the y coordinate. The following zones are defined: half coolant channel (grey), sleeve (red), 7 different fuel stripes, each ~1 mm thick, half graphite meat (yellow); the boundary conditions are reflective at all the six faces of the parallelepiped.

$$y = 0.0854x^2 - 0.0678x + 1.0105$$
$$R^2 = 0.9978$$
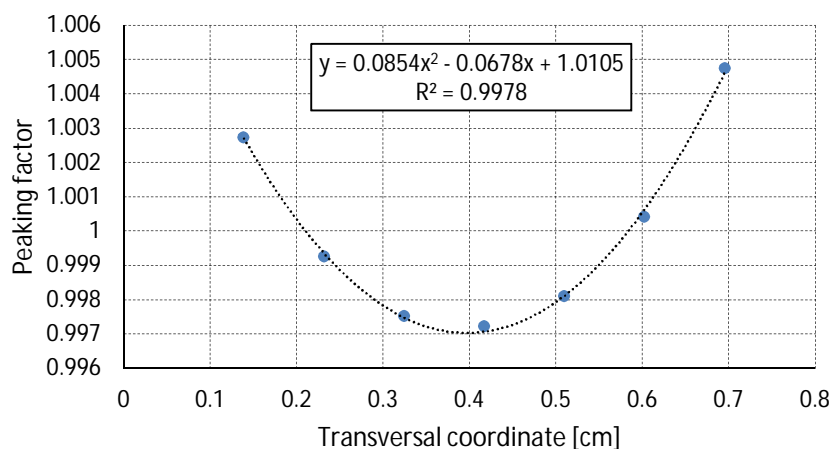
Figure 4-30. Normalized transversal power profile

The result from the SCALE simulation is the fission density for each of the 7 different TRISO particles belonging to one of the 7 stripes; the results were normalized with respect to the average value and presented in Figure 4-30. As we can see from Figure 4-30, the shape of the profile is quadratic and the fit is a good approximation of the results; the following aspects can be highlighted:

- The neutron flux depression causes the profile to be lower in the middle zone;
- High moderation from the graphite meat causes the fission density in the innermost layer to be higher than in the outermost, which is in contact with the sleeve and the coolant channel.

The overall peaking factor is about 1.005, which means that a flat power density profile in the fuel stripe is not far from the real condition.

4.3.2.b   Temperature profile with non-uniform power density profile

The results from the previous section were used to evaluate the difference, in terms of maximum temperature and temperature profile shape, between the uniform and non-uniform case.

First, the non-uniform distribution obtained for 7 points was adapted to the input of the MATLAB model, which requires only three transversal intervals; the results are:

- 33.35% for the outer layer;
- 33.25% for the middle layer;
- 33.40% for the inner layer.

These factors were used as input for the MATLAB model.
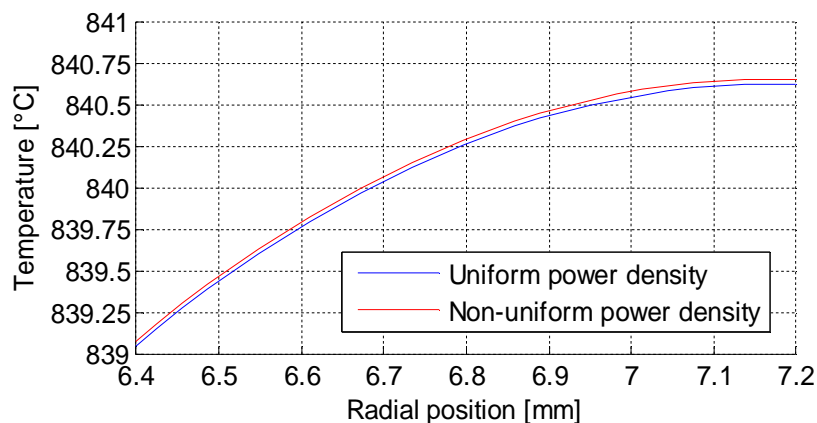
Figure 4-31. Temperature profiles for uniform and non-uniform power density at z=2.75 m

The last figure shows that the difference between the two cases is small: 0.03°C is the maximum temperature difference, for z=7.2 mm. This conclusion supports the adoption of a uniform power profile in the fuel stripe, which is a reasonable approximation of the real behavior.

59

4.4 RELAP5-3D single channel model

RELAP5-3D (Reactor Excursion and Leak Analysis Program) is a simulation tool that allows users to model the coupled behavior of the reactor coolant system and the core for various operational transients and postulated accidents that might occur in a nuclear reactor.

A simple RELAP5 model of the AHTR fuel plate and channel was developed in order to study the thermal-hydraulic features of the average fuel element, to prepare the base unit for the core model and to validate the results of the MATLAB model presented in the previous sections. Figure 4-32 shows the nodalization diagram of the model.
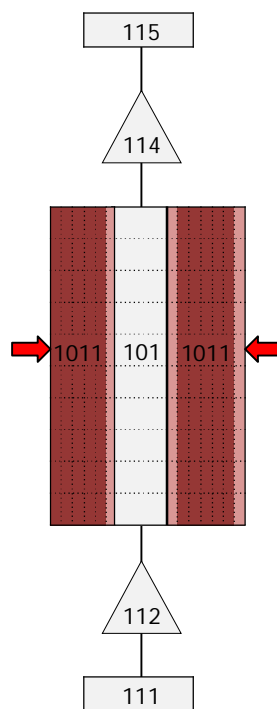
Figure 4-32. Nodalization diagram of the channel model

The salt mixture ms1, which corresponds to Flibe properties, was selected for the hydraulic system. The main component is the coolant channel (pipe 101); its features are shown in the next table:

Table 4-9. Geometric parameters of the coolant channel

Parameter	Value	Units
number of volumes	10	-
area	0.00155	m^2
length (per volume)	0.55	m
hydraulic diameter	11.64	mm

60

The hydraulic diameter selected for the model is the intra-assembly hydraulic diameter.

The coolant is pumped into the channel by a time-dependent junction (tmdpjun 112) with a mass flow rate of 5.8972 kg/s (obtained from the MATLAB model); the inlet flow temperature (650°C) is determined by a time-dependent volume (tmdpvol 111) located before the junction.

The outlet flow, through a single junction (sngljun 114), is collected in a time-dependent volume, which is needed to keep the atmospheric pressure constant (1 atm) at the top of the pipe.

The heat structure 1011 is a single plate with both the left and right boundaries connected to the pipe through a convective boundary condition: the two red arrows in Figure 4-32 show the contact surface between the two apparently detached parts of the same heat structure.

The real configuration of the heat structure is shown in Figure 4-33:
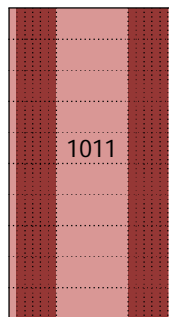
Figure 4-33. Real configuration of the heat structure modeling the fuel plate

The features of the heat structure 1011 are shown in the next table:

Table 4-10. Features of the heat structure modeling the fuel plate

Parameter	Value	Units
number of axial intervals	10	-
number of transversal nodes	14	-
Lateral heating area	0.12375	m^2
heating diameter	11.64	mm

The heat structure is composed of 13 transversal intervals: two outside small intervals to represent graphite sleeves, an inside wider interval for the graphite meat and 5 intervals (equally spaced) for each fuel stripe.

The power is distributed axially as a chopped cosine with a 7 m extrapolation length and transversely with a uniform profile, but only in the fueled intervals (graphite meat and sleeves don't generate power).

4.4.1 Comparison between MATLAB and RELAP5 single channel models

4.4.1.a Model validation: uniform power density

In order to check the differences between the two models developed with MATLAB and RELAP5, as a first case, a constant power distribution, in both axial and radial direction, was selected. Moreover, the RELAP model was tested with 10 axial intervals (which is the number that will be used for the core model) as well as with only one axial interval, in order to check the dependence of the accuracy of the model on the number of axial nodes.

The first aspect that must be tested is the temperature distribution of the coolant; the results for the steady state conditions are shown in the next figure.
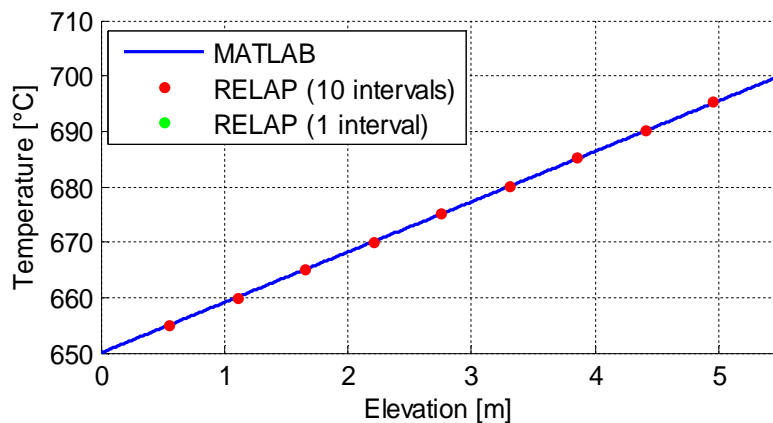
Figure 4-34. Coolant temperature profile (uniform axial power distribution)

As shown in Figure 4-34, the difference between the RELAP5 and MATLAB models is small, as expected, since the modeling of the coolant properties is the same for the two cases. Also, the green point in the plot shows that the single-interval model gives the same results as the 10 intervals model, but for the last interval only.

Other two features that can be evaluated, before going to the temperature distribution of the fuel plate, are the axial profiles of the heat flux and the heat transfer coefficient.

Figure 4-35 shows, as expected, that there is no difference between the three models in the value of the heat flux. The following aspect must be underlined: in this case a uniform power profile was selected, so there is no difference in the heat flux profile of the three models, but in a real case in which the power profile is not uniform (in our case, for example we will adopt a cosine power profile), there will be some difference in the heat flux profile of the RELAP and MATLAB model because of the RELAP5 coarser discretization, therefore the plate temperature distributions will be influenced by this factor.
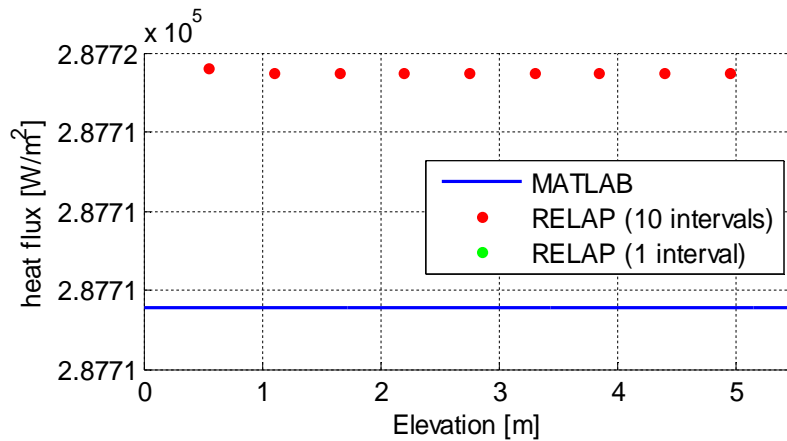
Figure 4-35. Heat flux at the plate surface (uniform axial power distribution)

The next figure shows the convective heat transfer coefficient as a function of the core elevation.
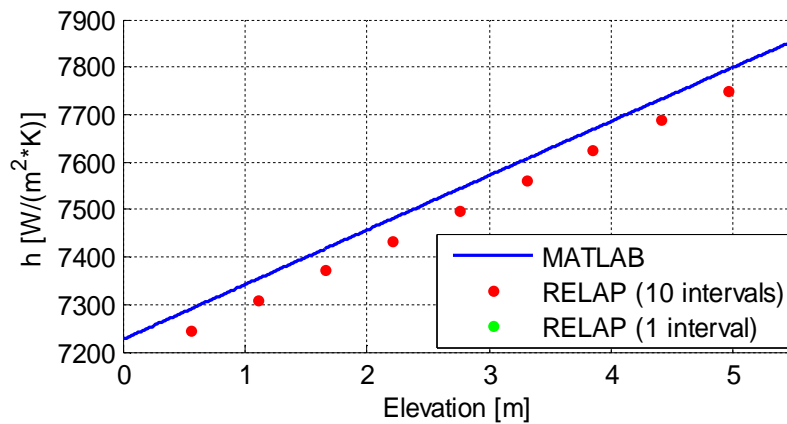
Figure 4-36. Heat transfer coefficient (uniform axial power distribution)

As we can see from the previous figure, the value of heat transfer coefficient differs from one model to the other by an amount equal to about 0.7%: this difference is not relevant, considering the fact that the temperature difference between the coolant and the surface of the plate is about 40°C and so the difference in the temperature drop between the two models would be less than 0.3°C.

In the next figures the description of the fuel plate temperature distribution is presented.

Figure 4-37 shows the temperature profile of the plate surface; the two temperature profiles are similar and just a small difference seems to come out for higher elevations, where the temperature is higher.

Figure 4-38 shows the temperature profile for the inner side of the fuel stripe, which is supposed to be the maximum radial temperature for a given elevation (since, for simplicity, no power generation in the graphite meat was modeled). Even in this case the maximum temperature difference is lower than 2°C, so we can say that the two models are in good agreement.

63
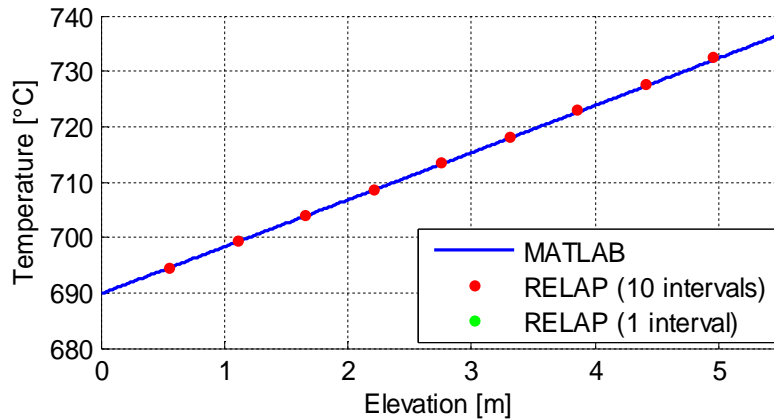
Figure 4-37. Plate surface temperature profile (uniform axial power distribution)
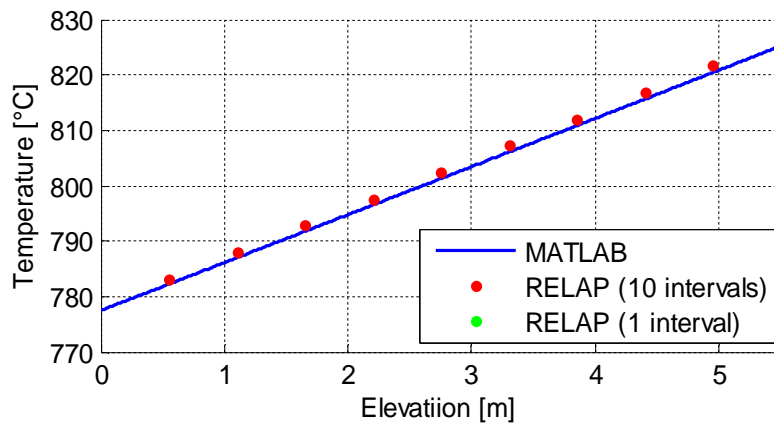
Figure 4-38. Plate centerline temperature profile (uniform axial power distribution)
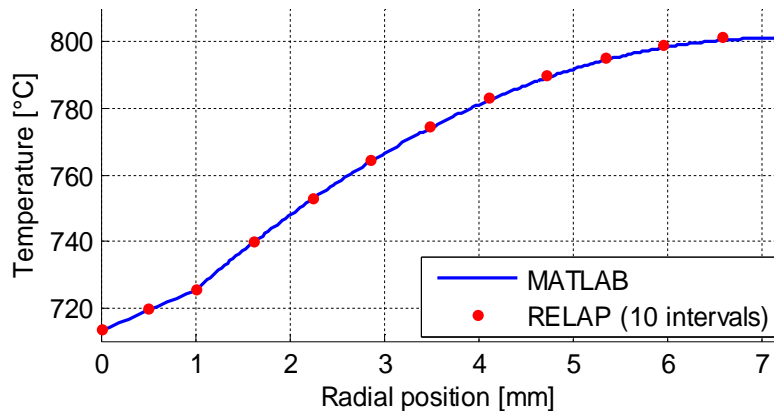
Figure 4-39. Plate radial temperature profile at z=2.75 m (uniform axial power distribution)

The last figure (Figure 4-39) shows the radial temperature profile at half core elevation (not far from the point in which the maximum fuel temperature is supposed to be): the difference is small for small x and increases as x increases, but still remains small and acceptable.

Considering the results presented in this section, the two models are in good agreement.

64

4.4.1.b   Chopped cosine axial power distribution, 10 axial intervals

A comparison has been performed between the MATLAB and RELAP5 model results for a chopped cosine power profile, simulating the real conditions of the average fuel assembly in the core. A first important premise must be considered: RELAP5 allows only a flat power profile within each interval, resulting in an approximated step cosine profile, as shown in the next figure.
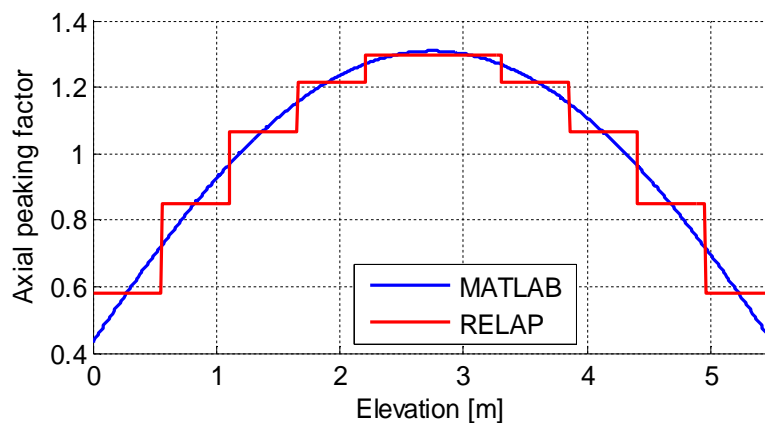
Figure 4-40. Normalized power profiles for the RELAP5 and MATLAB models (cosine power distribution, 10 axial intervals)

As shown in Figure 4-40, the two profiles are different so even the temperature distributions are expected to be different.

In Figure 4-41 the coolant temperature profile is plotted for the two models.
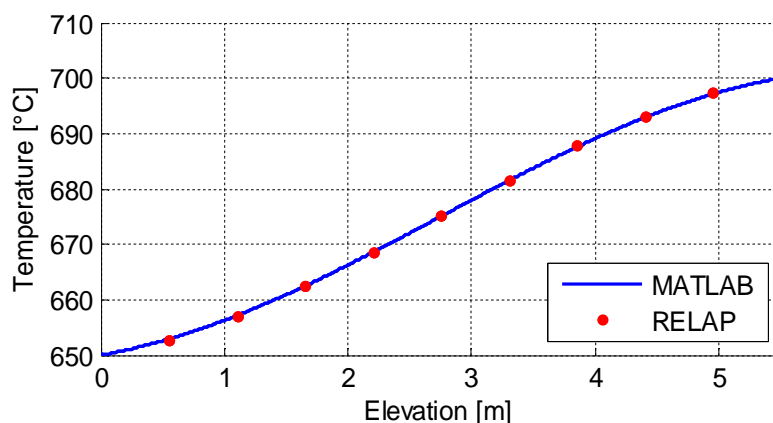
Figure 4-41. Coolant temperature profiles for the MATLAB and RELAP model (cosine power distribution, 10 axial intervals)

The two curves are almost coincident, as we expected, since the implementation of properties is the same. Even if the two power profiles are different, the coolant temperature profile is almost the same, because the coolant features are almost constant over the core elevation.

In the next figure the heat transfer coefficient is shown:
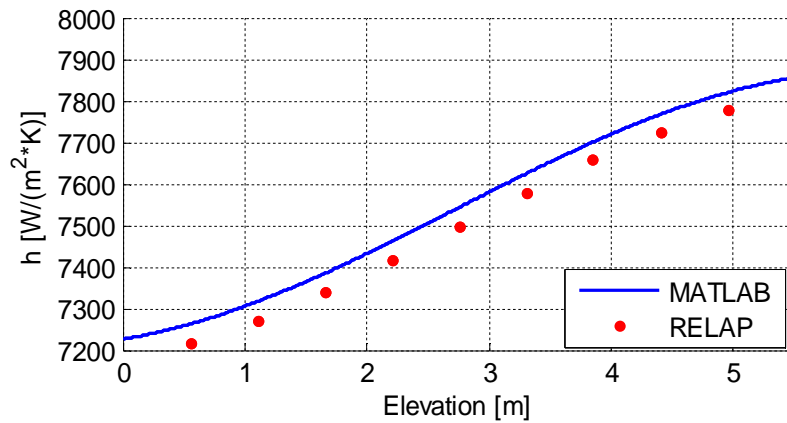
Figure 4-42. Heat transfer coefficient (cosine power distribution, 10 axial intervals)

We can see that the difference between the two curves is constant and equal to about 0.3% of the average value of the heat transfer coefficient: as in the uniform power distribution case, this error leads to a small error on the temperature drop between the coolant and the plate surface. The difference may be due to slightly different correlations used to calculate the coefficient. The next plot shows the surface heat flux:
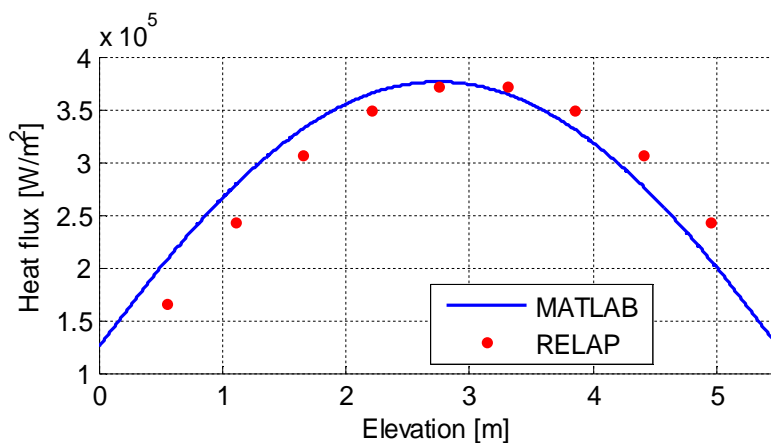
Figure 4-43. Heat flux at the plate surface (cosine power distribution, 10 axial intervals)

The two profiles are different and this difference is directly connected to the fact that the two models have a different axial power distribution.

In the next figures the temperature distribution of the plate is represented; in particular the plots show the temperature of the surface of the plate, the centerline temperature (maximum

temperature at a given elevation), and radial temperature profile at 2.75 m (half of the total core active height), not far from the maximum temperature location.
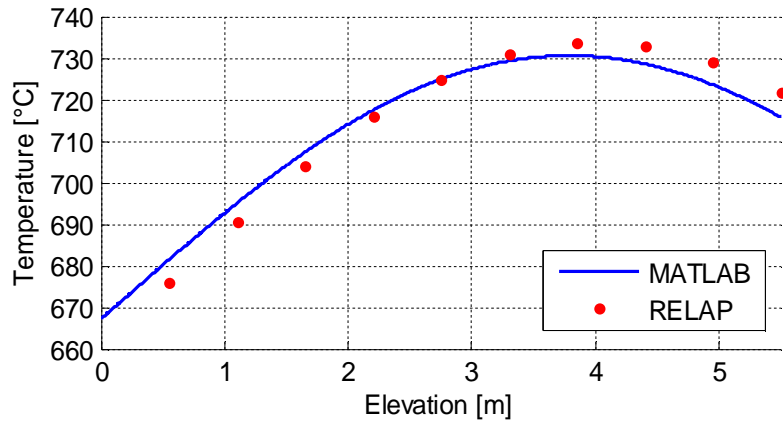
Figure 4-44. Temperature of the plate surface (cosine power distribution, 10 axial intervals)
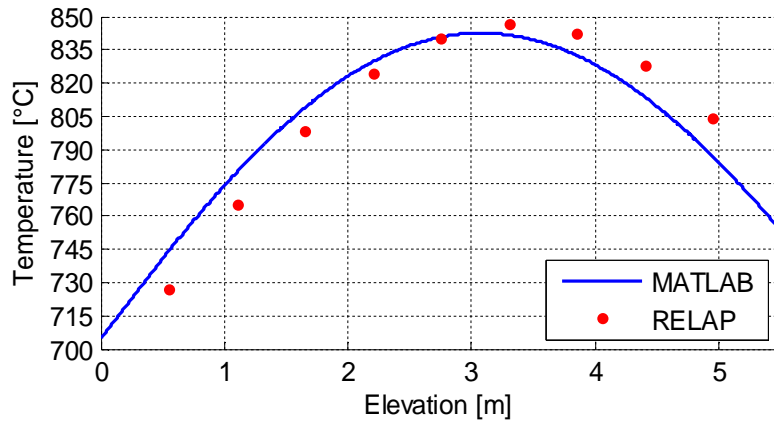
Figure 4-45. Centerline temperature of the fuel plate (cosine power distribution, 10 axial intervals)
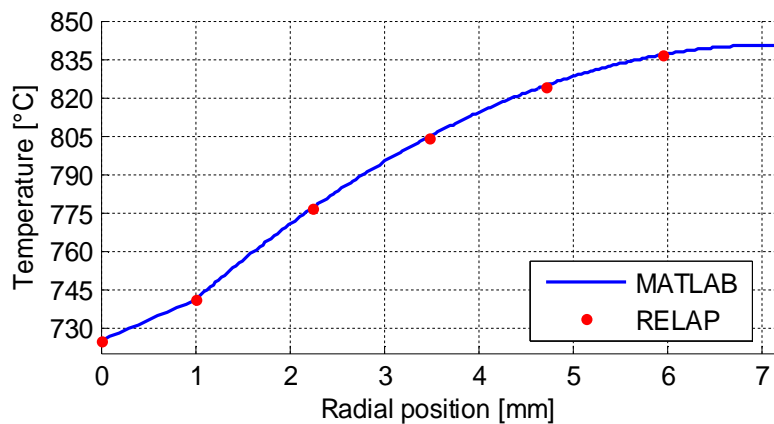
Figure 4-46. Radial temperature profile of the fuel plate (cosine power distribution, axial cosine profile)

Figure 4-46 shows the radial profile at 2.75 m elevation and the two profiles are similar, but this is because we selected a particular value for the elevation; for different values of elevation the

two profiles would not be coincident, since the power profile implemented in the two codes is different.

For the same reason (different power profile), the temperature profiles shown in Figure 4-44 and Figure 4-45 are different for the two codes; the different power profile explains also why the peak temperature for the RELAP5 model (for both the surface and centerline temperatures) is higher and located at higher elevation.

Despite the differences previously presented, this model was selected for a full core implementation, since the errors are considered acceptable with respect to the scope of this work.

4.4.1.c   Chopped cosine axial power distribution, 10 axial intervals, adapted MATLAB model

In order to check how much of the total difference is due to the difference in the axial power distribution, the power profile of the MATLAB model was modified and adapted to the profile used in the RELAP5 model, so that the two codes have the same power distribution, which is still an approximation of the "true" chopped cosine profile, as explained in section 4.4.1.b.

The next figure shows the centerline fuel temperature profile for the two models.
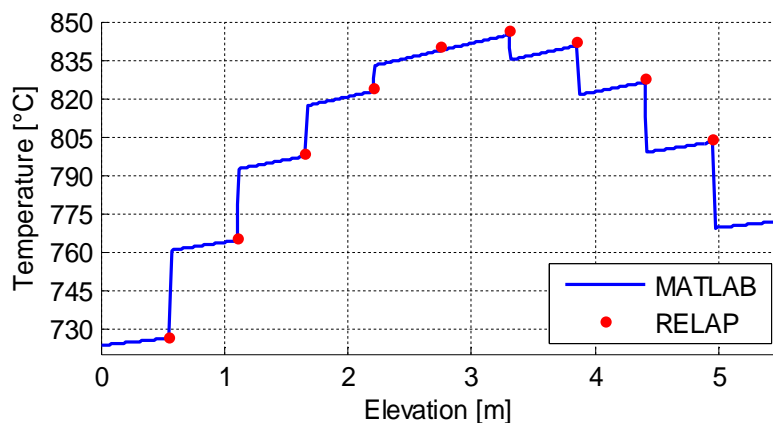
Figure 4-47. Centerline temperature profile (adapted MATLAB model)

The previous figure shows that the adapted MATLAB model is in good agreement with the results of the RELAP5 model.

The main component of the difference in the temperature profiles, in particular the location and the value of the maximum temperature of the plate, is mainly due to the difference in the power profile.

68

4.4.1.d   Chopped cosine axial power distribution, 20 axial intervals

Coming back to the MATLAB model with a continuous chopped cosine profile used in section 4.4.1.b, we expect that, if we increase the number of axial intervals, the difference between the two models should become smaller.

The following figure shows the centerline temperature profile for a RELAP5 model with 20 axial intervals.
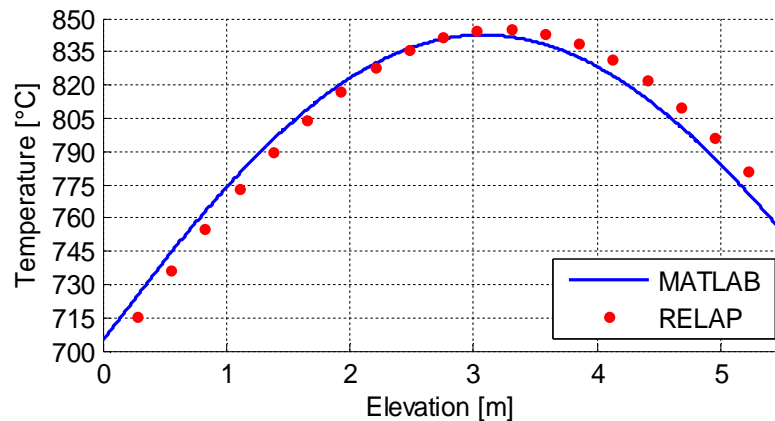
Figure 4-48. Centerline temperature profile (cosine power profile, 20 axial intervals)

As shown in the previous figure, the difference between the two models is smaller. Also the difference in the maximum temperature predicted by the two models is lower than 3°C and the difference in elevation is about 21 cm. However, the number of axial nodes was considered too high for a full core model implementation, which requires a simple base unit, so the 10-nodes model was selected.

4.5   Sensitivity studies

The MATLAB model was used to perform sensitivity studies on some of the main parameters of the AHTR fuel assembly: graphite conductivity, cladding thickness, meat thickness, TRISO particle packing fraction, coolant gap thickness. Further sensitivity studies were performed by assuming constant core pumping power or pressure drop, instead of constant core mass flow rate.

4.5.1   Thermal conductivity of graphite and irradiation effects

The maximum temperature of the fuel strongly depends on thermal conductivity of fuel and sleeve materials; the conductivity depends on temperature, usually decreasing for increasing

69

temperature. Moreover, the conductivity is partly determined by the neutron fluence, as it is shown in Figure 4-49; the conductivities presented in section 2.5 were used.

The following aspects must be highlighted:

- The increase in the maximum temperature from the beginning to the end of life due to conduction degradation is large, about 80°C;
- The increase of the maximum temperature is fast with respect to the neutron fluence, which is almost proportional to the residence time of the fuel assembly in the core.
- After the initial degradation the thermal conductivity reaches an asymptotic value.
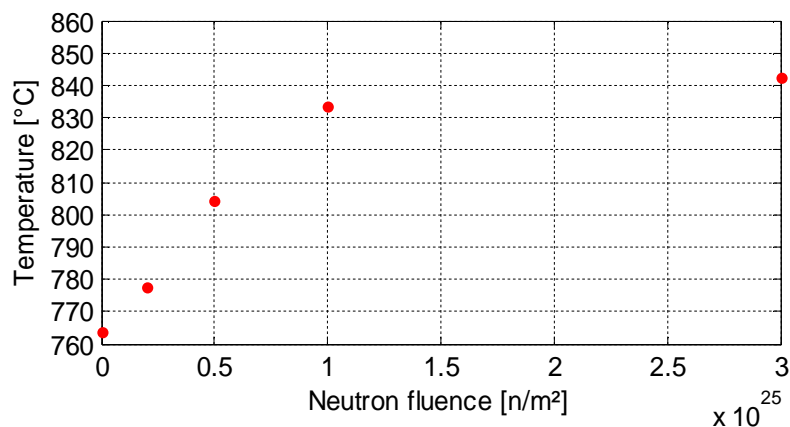
Figure 4-49. Maximum fuel temperature in the average assembly for different irradiations

In order to perform conservative evaluations, the worst case was considered in this work for thermal conductivity, by selecting the formula that accounts for temperature dependence and considers a high value of fast neutron fluence (above $3*10^{25}$ n/(m²)).

4.5.2   Sleeve thickness

The dependence of fuel maximum fuel temperature on the sleeve thickness was evaluated using the MATLAB model, for the average and the hottest assembly.

Values from 0.5 to 3 mm were considered. If the sleeve conductivity is constant the dependence is linear; in our model we considered temperature-dependent conductivity so the trend might not be perfectly linear. The results are shown in Figure 4-50. Even if the conductivity is temperature dependent, the profile is almost linear, as if conductivity were constant, so the temperature dependence of the sleeve material could be neglected. The maximum temperature has a relevant dependence on the sleeve thickness, about 15°C/mm for the average fuel assembly and 25°C/mm for the hottest assembly.

70

The reason for this strong dependence is the fact that all the power generated in the fuel must pass through the sleeve, before being removed by the coolant, producing a high temperature drop across the sleeve.
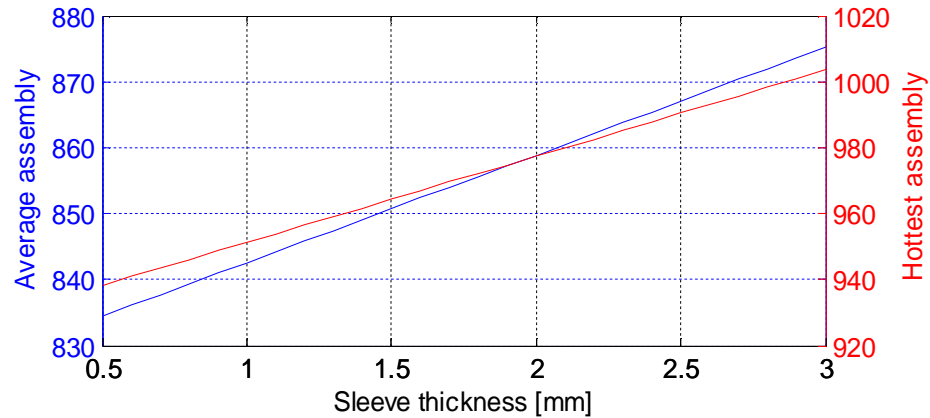
Figure 4-50. Maximum fuel temperature as a function of the sleeve thickness

A thin sleeve is desirable in order to reduce the maximum temperature, although the integrity of the fuel must not be compromised.

4.5.3   Fuel stripe thickness

The graphite and the fuel stripe thickness were then considered. The total thickness of the plate is kept constant (the sleeve thickness is 1 mm), so an increase of the graphite meat thickness corresponds to a decrease of the fuel stripe thickness, that is an increase of the CHM ratio or a decrease of the heavy metal loading into the core. The total power of the reactor is constant, so an increase in the fuel stripe thickness lead to a decrease of the average power density production or a decrease of the average neutron flux, since the material properties of the fuel (enrichment and packing fraction) remain unchanged.

A fuel stripe thickness of 11.75 mm corresponds to a fully loaded plate, while a thickness of 6.2 mm corresponds to the reference case. We expect that the maximum temperature increases as the thickness of the fuel stripe increases. The results are shown in Figure 4-51.

For the average fuel assembly, the variation of the maximum fuel temperature is ~16 °C/mm; this value is similar to the case of the cladding/sleeve (about 15°C/mm), but slightly smaller. Two aspects contribute to this effect:

- the maximum fuel temperature depends mainly on the average distance of the fuel from the surface, which is more sensitive on the sleeve thickness than on the fuel stripe thickness variation;
- the thermal conductivity of the fuel is lower than the conductivity of graphite.

From the previous considerations we can say that the maximum fuel temperature is partially affected by the fuel stripe thickness, if the power level of the reactor is considered constant, so the fuel stripe thickness should be optimized in order to obtain low fuel temperatures.
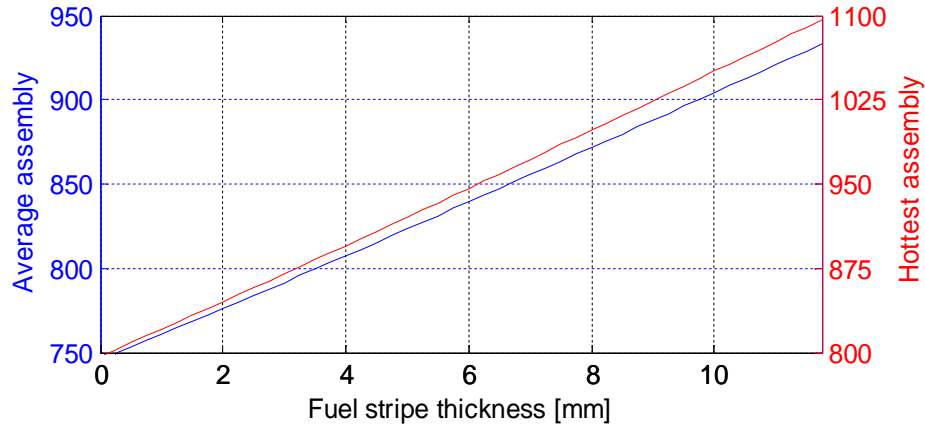
Figure 4-51. Maximum temperature as a function of the fuel stripe thickness (with constant plate thickness)

4.5.4   Packing fraction of the TRISO particles

The dependence of the maximum fuel temperature on the fuel packing fraction was evaluated. To preserve the same amount of fuel in the reactor (32.91 MT for the reference 2011 core design[6]), the fuel stripe thickness must vary when the fuel packing fraction is changed.

The reference packing fraction is 40%, the minimum packing fraction that would preserve the geometry features with this amount of fuel is approximately 21%.
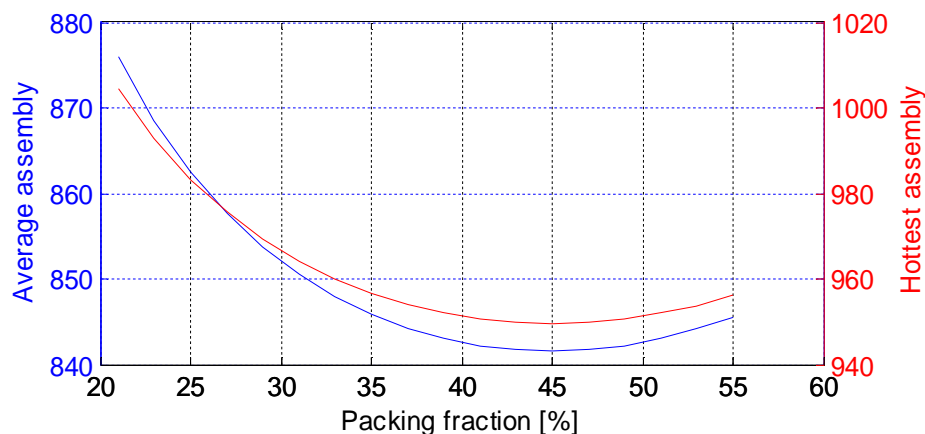
Figure 4-52. Maximum temperature dependence on TRISO particle packing fraction

Two aspects must be considered:

- When the packing fraction increases, the fuel thickness decreases;

- In relation to the modeling of the fuel conductivity, when the packing fraction increases, the conductivity of fuel decreases (section 2.5.1.a);

We can see that for low packing fraction up to a certain value (~45%) the first aspect prevails and the maximum temperature decreases, while above that value, since the second aspect is dominant, an increase in the packing fraction leads to higher fuel temperatures.

4.5.5   Coolant channel thickness

In relation to the fuel thermal performance, another important parameter to be evaluated is the coolant gap thickness. The reference value is 7 mm.

An increase in the coolant gap thickness corresponds to a decrease of the graphite meat and vice versa (the total mass of heavy metal must be conserved), which means that the thickness of fuel and sleeve is kept constant.

The maximum temperature dependence is shown in Figure 4-53.

Since this model assumes the capability of the primary pumps to force the nominal mass flow rate in any condition, a reduction of the channel dimensions has a positive effect on the temperature distribution (the Reynolds number and the heat transfer coefficient are higher), because the heat transfer is enhanced.

The negative effect can be found in the increase of the flow velocity and the pressure drop across the core, as we can see in Figure 4-54.

Since the requirements presented in section 4.1.3 (pressure drop lower than 1.5 atm and flow velocity less than 3 m/s) must be strictly followed, the coolant gap cannot be smaller than ~5 mm. The nominal value selected for the reference design (7 mm) is slightly above this value.
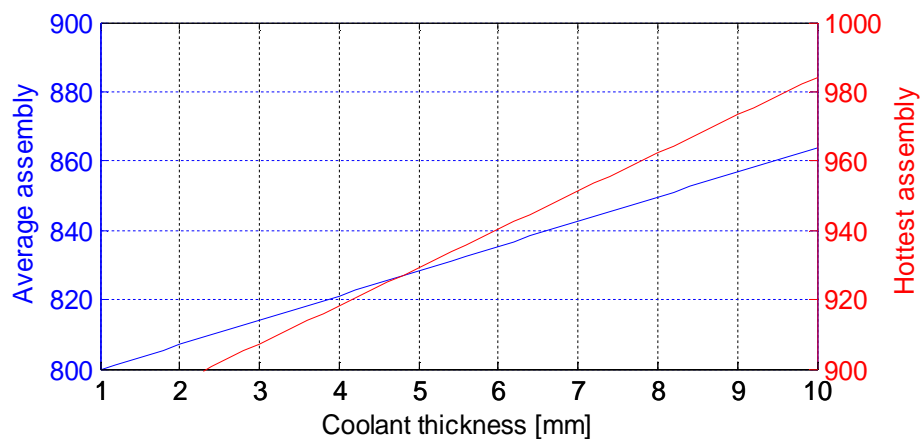
Figure 4-53. Maximum temperature as a function of the coolant gap thickness (constant fuel stripe and sleeve thickness)
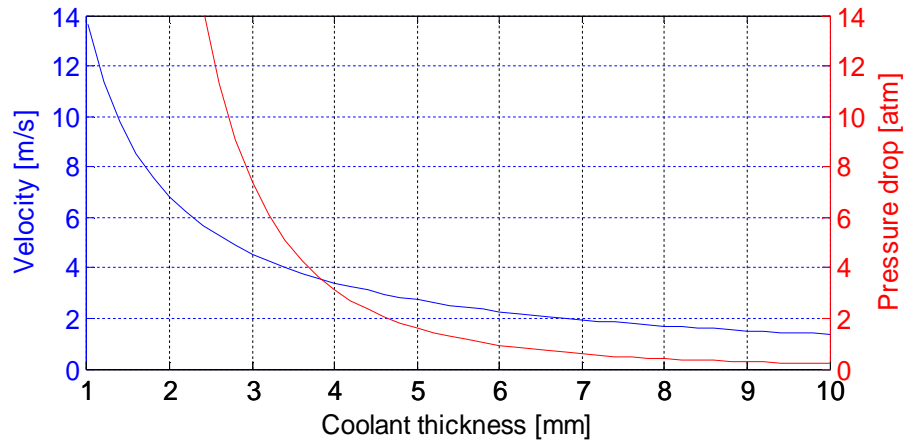
Figure 4-54. Flow average velocity and channel pressure drop as functions of the coolant gap thickness

4.5.6 Dependence on coolant gap and graphite meat thickness

Two-parameter sensitivity studies have been performed using the MATLAB model; two parameters were changed at the same time and the maximum fuel temperature was evaluated.

The two parameters considered for this study are the coolant gap thickness and the fuel stripe thickness; the total power produced by the plate was considered constant, as well as the sum of the plate and the coolant gap thickness, which is directly connected to the constant dimensions of the fuel assembly.

The range of variability of the two parameters is limited by the fact that the total fuel plate thickness must be lower than 2.55+0.7=3.25 cm: this limit is required to avoid the overlapping of adjacent plates.

Three different conditions have been considered: constant core mass flow rate, constant core pumping power and constant core pressure drop. Since the results for the last case were similar to the constant pumping power case, the constant pressure drop case is not presented in this section.

4.5.6.a Constant mass flow rate

Initially, a constant core mass flow rate was considered: the MATLAB model was developed assuming constant mass flow rate, so no modifications of the model were needed. This hypothesis is based on the assumption that the pump of the primary circuit can provide a constant mass flow rate, independently from the core pressure drop to be overcome.

The contour lines are straight lines and the importance of the fuel stripe thickness seems to be more relevant than the importance of the coolant gap thickness: the highest temperatures are obtained in the upper part of the plot shown in Figure 4-55, where the fuel stripe is thicker.

The maximum temperature changes by about 100°C when the fuel stripe thickness goes from 4 to 10 mm (the reference value is 6.2 mm[6]), so we can conclude that the optimization of the fuel stripe thickness is fundamental in order to obtain low operational temperatures.
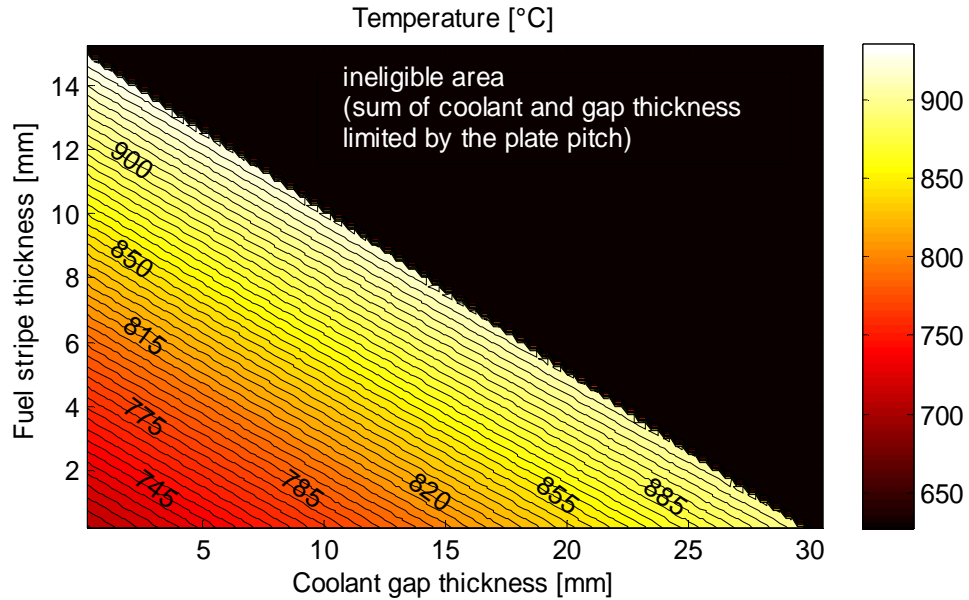
Figure 4-55. Maximum fuel temperature as a function of coolant gap and fuel stripe thickness (constant mass flow rate)
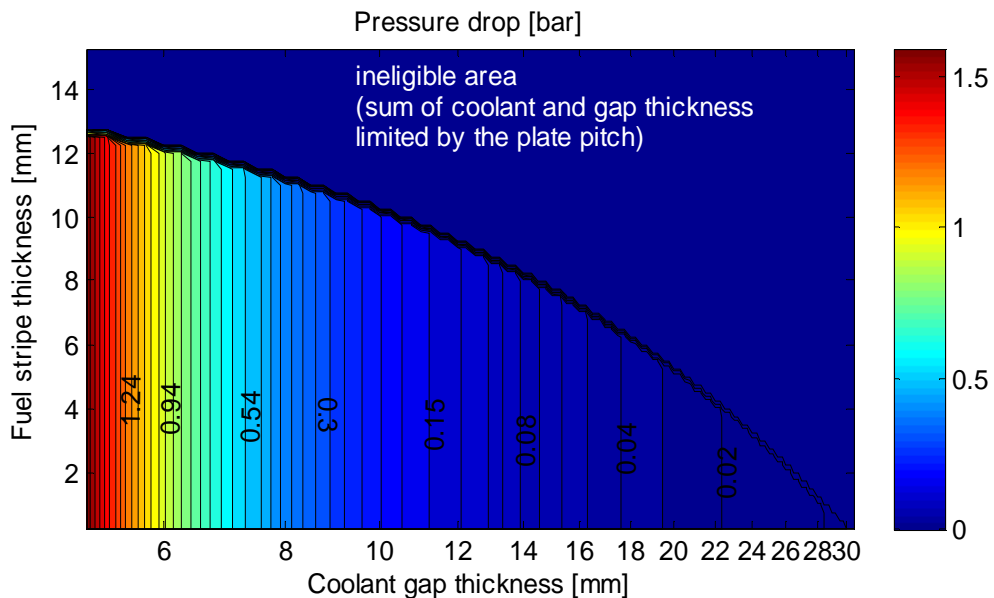
Figure 4-56. Core pressure drop as a function of coolant gap and fuel stripe thickness (constant mass flow rate)

The variation of maximum temperature when the coolant channel spans over the same range (4 to 10 mm, reference value: 7 mm[6]) is about 40°C, lower but still relevant, so even the coolant gap requires optimization in order to keep low core temperatures.

The negative effect of the fact that the mass flow rate is constant is the increase of the core pressure drop when the coolant gap is thinner (and the heat exchange coefficient is higher), as shown in Figure 4-56.

The pressure drop does not depend on the fuel stripe thickness but only on the coolant gap width, it increases when the gap becomes thinner and also for low values of the gap the variation of the pressure drop with the gap thickness is higher than for large gaps. Since the design goal for the AHTR is a core friction pressure drop lower than 1 atm, the plot shows that the limiting value for the gap thickness is about 6 mm (yellow stripe).

4.5.6.b   Constant pumping power

The same model was used to evaluate the maximum temperature of the fuel plate as a function of the coolant gap and the fuel stripe thickness when the power of the primary pumps is constant. In the MATLAB model a constant mass flow rate is given as a starting point for the calculation of all the other parameters and the pumping power is obtained as a result, but in our case we would like to have the opposite condition (given a certain pumping power, the mass flow rate is the result of the calculation). Since we did not want to change our model, we adopted the following procedure: for each couple of fuel stripe and coolant gap thickness, a certain number of iterations was run and the value of mass flow rate was adjusted until the relative error, that is the normalized difference between the actual and the desired value of pumping power, was reduced below a certain value (0.1%). The pumping power selected for this study was 1 MW[6] and the maximum temperature distribution is presented in Figure 4-57.
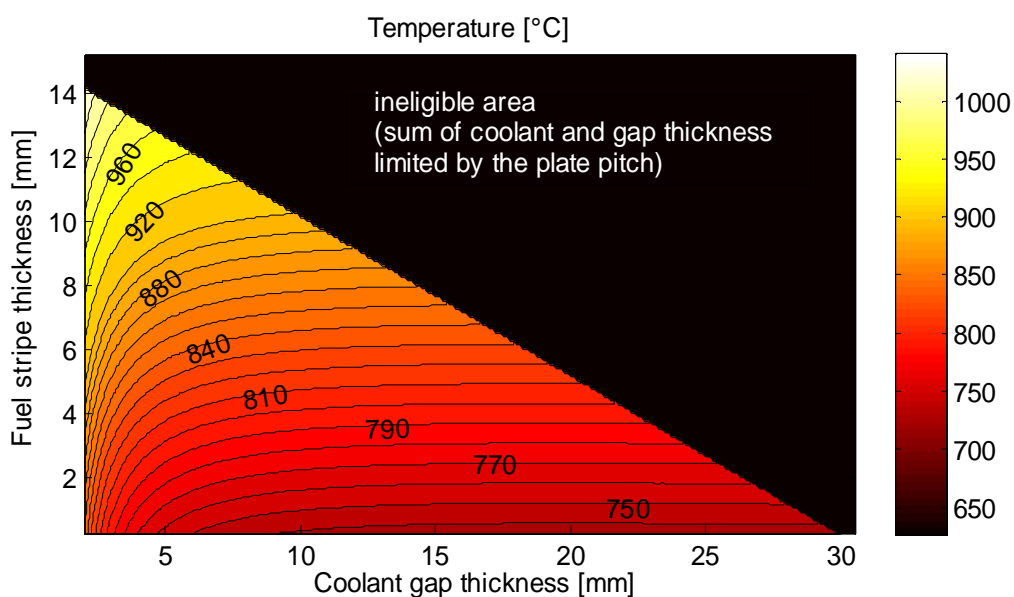
Figure 4-57. Maximum temperature distribution as a function of coolant gap and fuel stripe thickness (constant pumping power)

76

Comparing the previous figure to Figure 4-55, the results are now completely different: thinner coolant gap leads to higher fuel temperature. The dependence on the fuel stripe thickness was not changed: low thickness leads to lower temperatures.
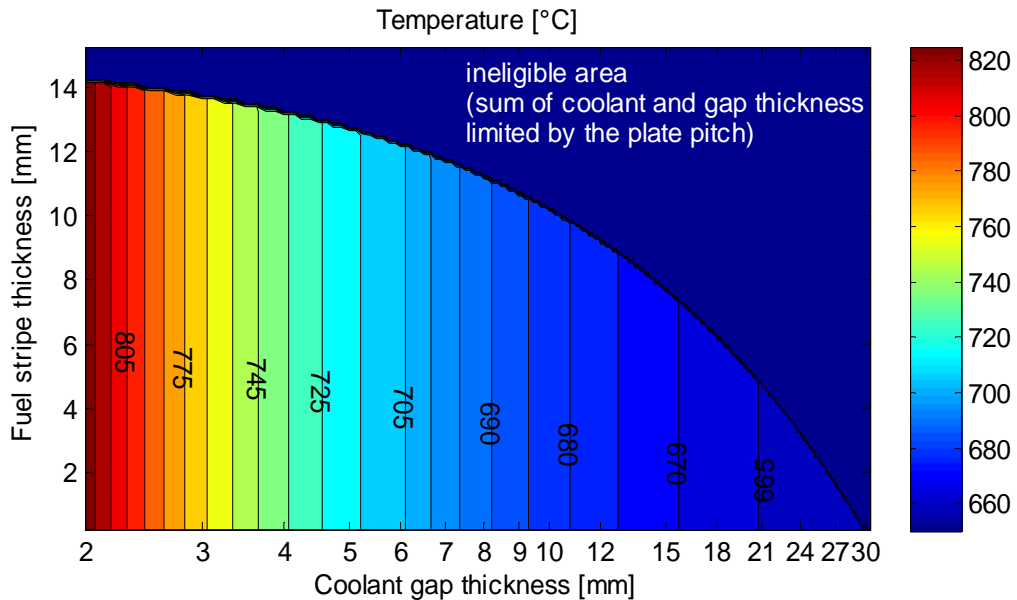
Figure 4-58. Coolant outlet temperature as a function of coolant gap and fuel stripe thickness (constant core pumping power)

In relation to the coolant gap thickness dependence, the reason for the fuel temperature increase when the gap decreases can be found in the reduction of mass flow rate through the core due to higher pressure drop. We can see that the maximum temperatures does not depend on the coolant gap thickness until the thickness is equal to or lower than ~5 mm, so in order to reduce the maximum fuel temperature and the amount of coolant required the selected thickness for the gap should not be too different from this value; in fact the nominal value of gap thickness selected for the reference design is 7 mm, which is in agreement with these results.

Since the total reactor power (3400 MW$_{th}$) is constant and the mass flow rate can change with the coolant thickness, the outlet coolant temperature is not constant. The outlet coolant temperature distribution is shown in Figure 4-58.

AHTR ASSEMBLY AND FULL CORE MODEL

5.1 Fuel assembly RELAP5-3D model

5.1.1 Structure of the RELAP5 assembly model

A RELAP5-3D model of one third of the AHTR fuel assembly was developed.
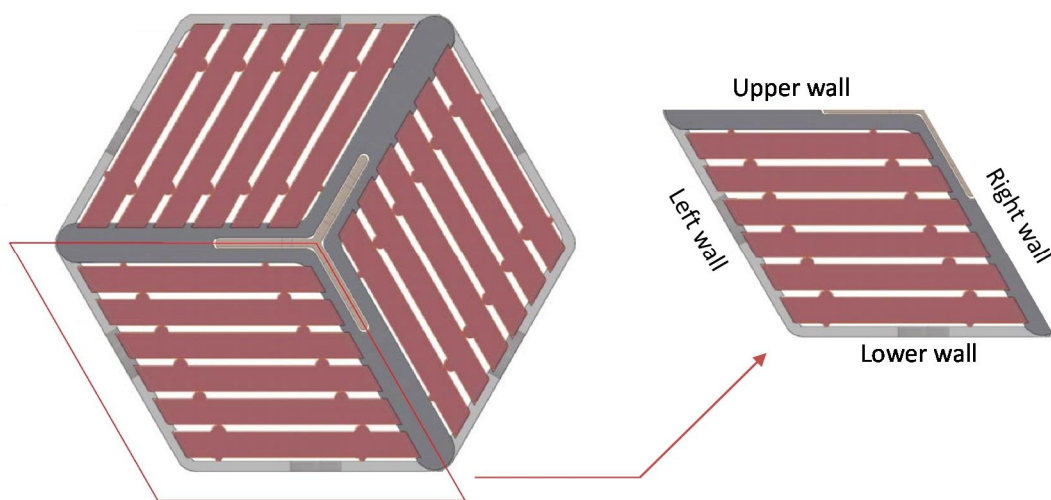
Figure 5-1. Cross section of the AHTR fuel assembly[6]

As shown Figure 5-1, the assembly has a three-fold symmetry, so we can consider just the part of the section which is contained within the red line: six fuel plates, seven intra-assembly coolant channels, two faces of the external hexagonal graphite wall, two half branches of the Y-shaped support and two inter-assembly coolant channels.

In Figure 5-2 the nodalization diagram of the model is shown.

The structure consists of:

- Inlet components: salt tank (time-dependent volume 112), pump (time-dependent junction 111) and inlet plenum (branch 110);
- Assembly: 7 intra-assembly coolant channels (pipe 101 to 107), 2 inter-assembly coolant channels (pipe 108, 109), 6 fuel plates (heat structures 1012, 1021, 1031, 1041, 1051, 1061), the lower box wall (heat structure 1011), the left box wall (heat structure 1091) and the Y-shape (heat structure 1071);
- Outlet components: outlet plenum (branch 113), connection to the outlet tank (single junction 114), outlet tank (time-dependent volume 115).

5.1.1.a   Hydrodynamic components

The salt tank keeps the inlet coolant temperature constant at 650°C. The dimensions and features of the tank are shown in Table 5-1.

The pump is modeled as a time-dependent junction for which the mass flow rate is set to 37.25 kg/s, equal to one third of the average mass flow rate per assembly.

The junction is connected to a branch which divides the mass flow between the channels; the arrows above the branch represent the connections (junctions) to the channels.

The branch has the same geometrical features of the inlet tank, but temperature and pressure can change in time.
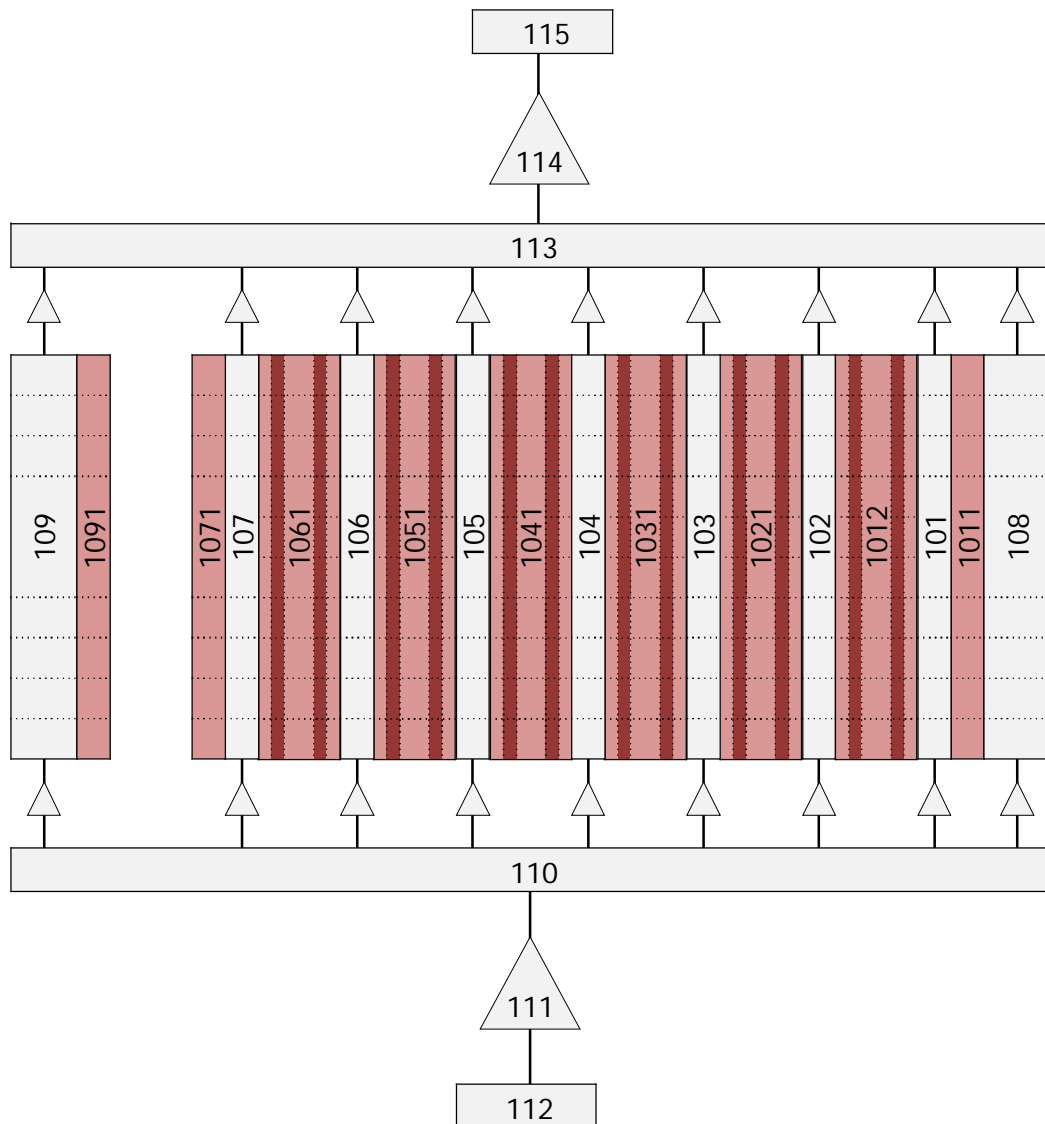
Figure 5-2. Nodalization diagram of the RELAP5-3D assembly model

Table 5-1. Parameters for the component 112 (salt tank)

Parameter	Value	Units
length	0.25	m
area	0.063	m²
roughness	1.00E-06	m
pressure	1	atm
temperature	650°C	mm

The form loss coefficient of the junctions of the branch is set to 0.25 for the 7 intra-assembly coolant channels and to 1500 for the two inter-assembly channels: this last value is fundamental since it determines the inter-assembly mass flow rate and the overall pressure drop of the core. The features of the coolant channel are shown in the next table.

Table 5-2. Parameters for the coolant channel

Parameter	Value	Units
length	6	m
area	15.5	cm²
number of intervals	12	-
roughness	1.00E-06	m
hydraulic diameter	13.5	mm

Channels 101 and 107 have the same features, but the cross section is equal to half the area from Table 5-2 and the hydraulic diameter is 6.9 mm; channels 108 and 109 (outside channels) have an area equal to 22.5 cm² and an hydraulic diameter equal to 34.6 mm.

The length of the 12 intervals is not constant since the first and the last represent the lower and upper reflector which is 25 cm long (while the other intervals are 55 cm long).

Above the channels, several junctions (one for each channel) connect the core to the outlet plenum, where the mass flows from each channel are mixed together; a single junction connects the plenum to the outlet tank.

The outlet tank is a time-dependent volume which keeps the pressure constant at 1 atm at the top of the assembly, so the pressure in the lower plenum is expected to be substantially higher than 1 atm.

5.1.1.b   Heat structures

Heat structures are used to model the fuel plates, the assembly box wall and the Y-shape.
A top view of the coolant channels and heat structures is given in Figure 5-3.

Each heat structure consists of 12 axial intervals (the first and the last are reflectors, the material is graphite); the total height is 6 m, the 1st and the 12th intervals are 25 cm high while the others are 55 cm (total active height: 5.5 m).

The width of the heat structures is 22.5 cm, so the lateral heat exchange area is 0.12375 m^2 for each interval, for each side (0.05625 m^2 for the two shorter segments, the first and the last with respect to the core elevation).

The fuel plate is divided into 14 transversal intervals with the following composition and dimensions:

- 1st interval: sleeve; total thickness: 1 mm; composition: graphite;
- 2nd to 6th: fuel stripe; total thickness: 6.2 mm; composition: fuel;
- 7th to 8th: graphite meat; total thickness: 11.1 mm; composition graphite;
- 9th to 13th: fuel stripe; total thickness: 6.2 mm; composition: fuel;
- 14th: sleeve; total thickness: 1 mm; composition: graphite;

Each fuel plate is connected to two different coolant channels, one for the right side and one for the left side.
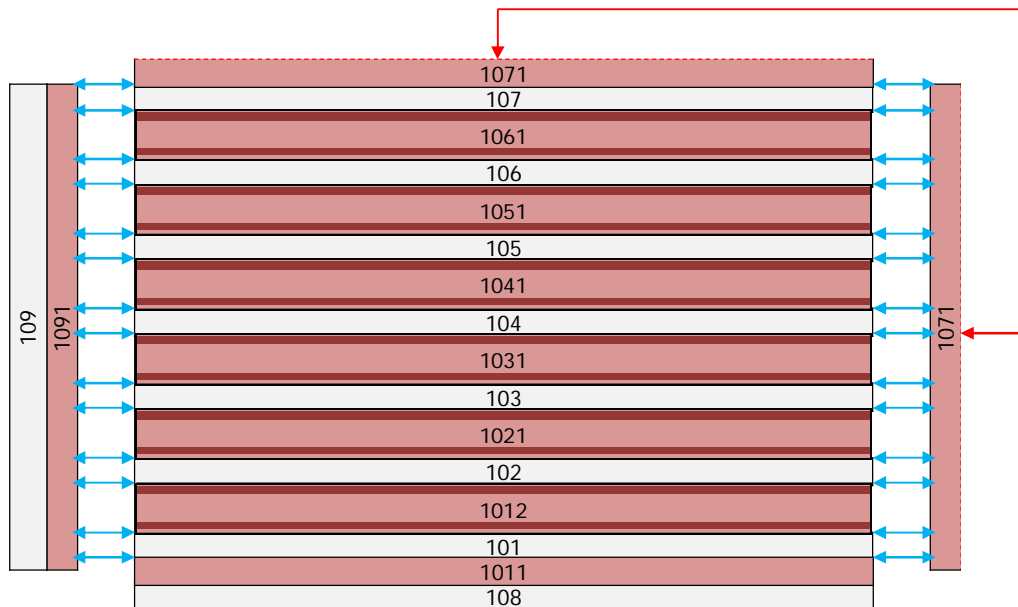
Figure 5-3. Top view of the nodalization diagram of the fuel assembly model

The heat structures 1091 and 1011 are the left and lower box wall; the thickness is 1 cm and 1.35 cm respectively (both divided into 5 transversal segments). The heat structure 1091 is connected to the outside coolant channel 109 on the left, while the right surface is heated by fuel plates through conduction. The heat structure 1011 is connected to the outside coolant channel 108 on the lower side and to the inside coolant channel 101 on the upper side.

The heat structure 1071 represents both the upper and the right Y-shape branches (the red arrow indicates the surface of connection between the two apparently detached heat structures), since the right boundary is connected to the inside coolant channel 107, while the left surface receives conduction heat from plates (blue arrows on the right part of Figure 5-3). The total thickness of this heat structure is 4 cm, divided into 8 transversal segments.

The conduction between surfaces in RELAP5 can be obtained through the definition of conduction enclosures.

A conduction enclosure is a group of surfaces that can exchange heat among themselves; for each surface belonging to the enclosure the following features require to be defined:

- Gap conductance [W/(m²*K)]; the RELAP5 manual suggests to calculate the conductance as $\frac{k_1*k_2}{(k_1+k_2)*dl}$, where dl is the distance between the two surfaces and k_1 and k_2 are the conductivities of the two surfaces;

- Area factors: fraction of the surface involved in heat conduction; for each surface, as many factors require to be defined, as the number of the surfaces belonging to the enclosure;

In this model a conduction enclosure for each axial level has been defined; the model does not account for axial conduction.

The surfaces involved in conduction exchange are indicated in Figure 5-3 by blue arrows: each blue arrow connects two surfaces that exchange heat one to the other; for example the upper surface of fuel plate 1031 exchanges heat with the right surface of 1091 and the left surface of 1071. As shown in Figure 5-3, 16 surfaces are involved in the heat exchange for each axial level, for each conduction enclosure.

Given that the gap conductance and the area factors are known, a strong approximation is assumed: the conduction heat exchange can occur only between external heat structure surfaces, not between internal mesh surfaces; anyway this is the only possibility through which RELAP5 can take into account heat conduction.

5.1.1.c   Power density distribution

The power is distributed in the axial direction as a chopped cosine with a 7 m extrapolated length; the reflectors do not generate power, so the total power of a plate is shared among 10 axial active intervals.

In relation to the horizontal power distribution, RELAP5 does not allow to account for the heat transfer due to nuclear radiation absorption, so some assumptions were adopted, regarding the fact that the power produced is deposited partly in fuel, partly in other structures and in the coolant. The following approximation was adopted: no power generation occurs in graphite

walls and Y-shape and no power is directly absorbed by the outside channels. This assumption is based on the following motivations:

- since both graphite and Flibe atoms are not substantially different in terms of atomic weight, as a first approximation, the amount of radiation absorption (which means power generation) depends only on the fraction of volume occupied;
- as shown in Figure 5-1, the volume fraction (which corresponds to the area fraction, since the structure does not change with the elevation) occupied by outside coolant channels, box walls and Y-shape is small, if compared to the area fraction occupied by plates and inner channels.

In this model the power is produced in fuel plates and coolant channels only.

The amount of power produced per plate was determined by dividing the core power by the number of assemblies (252) and plates per assembly (18).

With reference to a single plate, 2% of power is directly transferred to the coolant channels (1% on the left channel and 1% on the right channel), without passing through the heat structure; the remaining 98% is shared among fuel stripes (49% per stripe) and graphite meat (2%).

So, for each plate, the following power generation distribution is assumed:

- 96% in the fuel;
- 2% in the graphite meat;
- 2% directly in the coolant.

5.1.2   Features of the assembly model

This section presents the thermal-hydraulic features for the fuel assembly model. The gap conductance for the conduction enclosures was set to $3*10^4$ W/(m^2*K); the pressure loss coefficient for the two inlet junctions of the inter-assembly channels (pipes 108 and 109) was set to 1500.

The main results of a steady-state simulation are shown in Table 5-3.

As shown in the previous table, the outlet temperature of the smaller inside channels (101 and 107) is 20°C higher than the outlet temperature of other intra-assembly channels. This is due to the fact that, even if the flow area is half the flow area of the other channels, the mass flow rate is less than a half (about one third). This implies that the fuel plates closer to the Y-shape and the box wall (1061 and 1012, red points in Figure 5-4) will be hotter than other fuel plates (blue points in Figure 5-4).

The outlet temperature of the inter-assembly channels is 30 degrees lower than the outlet temperature of the intra-assembly channels; this model underestimates the amount of power

that is transferred through the box walls to the inter-assembly mass flow, for the following reasons:

- low value of gap conductance for the conduction enclosure model;
- only external surfaces involved in conduction; this means that the box wall cannot reach temperatures higher than the surface temperature of fuel plates;

Table 5-3. Coolant thermal-hydraulic features

Parameter	Value	Units
outlet plenum temperature	700	°C
channel 104 outlet temperature	700	°C
channel 101 outlet temperature	720	°C
channel 107 outlet temperature	723	°C
channel 108 outlet temperature	669	°C
channel 109 outlet temperature	672	°C
channel 104 mass flow rate	6.31	kg/s
channel 101 and 107 mass flow rate	1.99	kg/s
channel 108 and 109 mass flow rate	0.86	kg/s
channel 104 average flow velocity	2.09	m/s
pressure drop across the core	1.789	atm
friction pressure drop across the assembly	0.619	atm
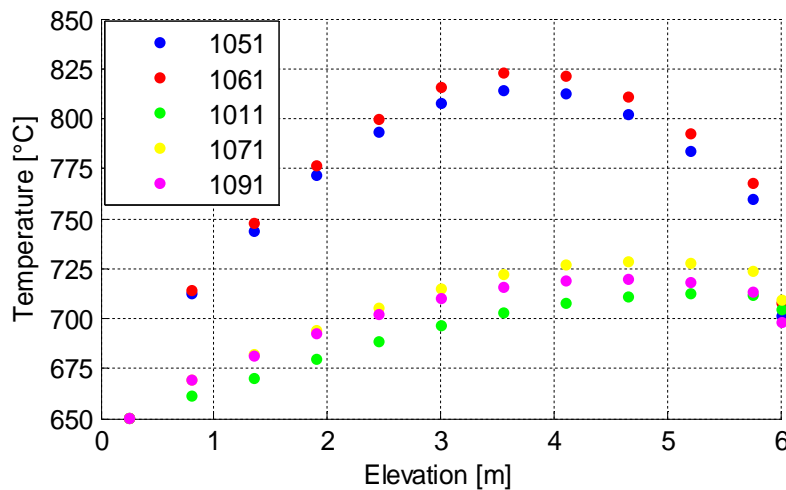
Figure 5-4. Axial profile of the average fuel temperature for different heat structures

Other hydraulic features, like flow mean velocity into the coolant channel and friction pressure drop across the assembly, are similar to what was obtained for the single channel model.

Figure 5-4 shows the average temperature profiles for box wall and Y-shape, compared to fuel plate temperature profiles; the average temperature of the structures (box wall and Y-shape) is 100°C lower than the average temperature of a fuel plate.

Figure 5-5 shows the centerline (maximum) temperature profile of the fuel plate 1041; in addition, the RELAP results are compared to the results obtained from the MATLAB model.

The MATLAB model presented in section 4.1 was slightly modified in order to account for the following aspects:

- the initial MATLAB model had a different total amount of power produced into the plate (we assumed that only 95% of the power is directly produced into the plate[6]), while in the RELAP model 96% comes from the fuel stripe, 2% from graphite meat and 2% is directly given to the coolant, so the total power produced into the plate is about 98%;

- different transversal power distribution: the initial MATLAB model did not account for power production into the graphite meat, so the transversal power profile of the new MATLAB model was modified and the power profile described in the previous bullet was implemented;

- different axial power profiles for the MATLAB (almost continuous chopped cosine) and the RELAP model (step "chopped cosine"), as explained in section 4.4.1.b.
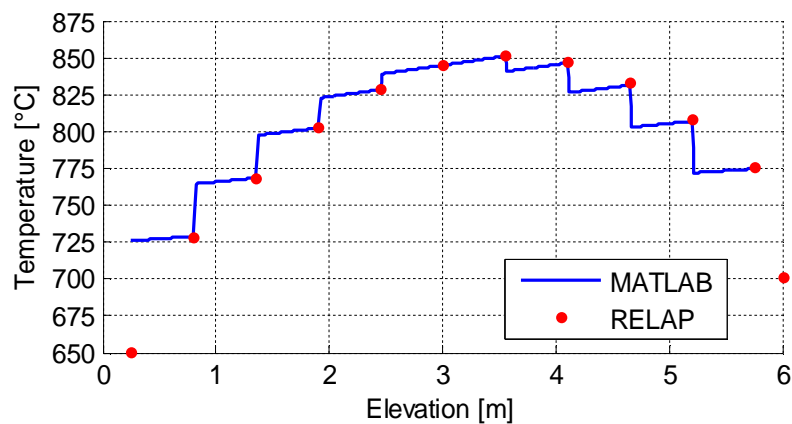
Figure 5-5. Centerline temperature profile of the fuel plate 1041
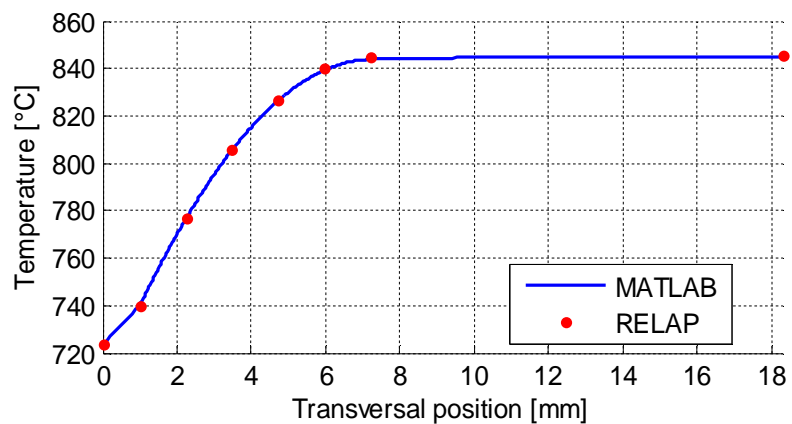
Figure 5-6. Transversal temperature profile for the heat structure 1041 at z=2.75 m

Figure 5-5 shows the axial centerline temperature profile for the heat structure (fuel plate) 1041. Figure 5-6 shows the transversal temperature profile for the heat structure (fuel plate) 1041 at z=2.75 m. As shown in Figure 5-6, the results from the adapted MATLAB model and the RELAP assembly model are in good agreement.

5.1.2.a   Pressure drop for the inter-assembly channel

The value of the form loss coefficient at the inlet of the inter-assembly channels, previously set to 1500, was then increased to reduce the mass flow rate and increase the outlet temperature of inter-assembly coolant.
The results are presented in the Table 5-4.
Despite the high increase in the form loss coefficient, the outlet temperature of the outer channels remains well below 700°C, which is the nominal average outlet temperature in the upper plenum.

Table 5-4. Results for different values of form loss coefficient

Form loss coefficient:		1500	2000	2500	3000	3500	5000	10000
outlet plenum temp.	°C	700	700	700	700	700	700	700
chann. 104 outlet temp.	°C	700	700	700	700	700	700	700
chann. 101 outlet temp.	°C	720	720	720	720	720	720	720
chann. 107 outlet temp.	°C	723	723	723	723	723	723	723
chann. 108 outlet temp.	°C	669	671	673	674	676	679	686
chann. 109 outlet temp.	°C	672	674	676	678	679	683	691
chann. 104 mass flow rate	kg/s	6.31	6.35	6.38	6.40	6.41	6.45	6.50
chann. 101, 107 mass flow rate	kg/s	1.99	2.00	2.01	2.01	2.02	2.03	2.04
chann. 108 109 mass flow rate	kg/s	0.86	0.74	0.67	0.61	0.57	0.48	0.34
chann. 104 flow velocity	m/s	2.09	2.10	2.11	2.12	2.12	2.13	2.15
friction pressure drop	atm	0.619	0.626	0.631	0.634	0.637	0.643	0.652

5.1.3   Heat conduction of the assembly structure

The assembly model presented in the previous sections is not capable of a realistic description of the heat conduction in the structures which form the fuel element, because the heat is transferred to the box wall through the external surfaces of the fuel plates only. Two possible solutions are proposed in the following sections: the homogenization of the sleeve with the fuel stripe, and the modification of the conductivity of the box wall.

5.1.3.a   Homogenized model

The fuel assembly model was slightly modified in order to be able to increase the gap conductance in the conduction enclosure definition, which is limited by the thickness of the heat structures. In fact, if the thickness of the heat structures is excessively small, RELAP5 might not be able to perform the calculation, due to potential numerical instabilities.[19]

As mentioned above, the transversal configuration of the fuel plate was modified in this way:

- 7.2 mm fuel (the sleeve is removed and 1mm is added to the fuel stripe to replace the sleeve); 1 interval;

- 11.1 mm graphite meat; 2 intervals;

- 7.2 mm fuel (the same as the one on the other side); 1 interval;

The power distribution was not modified; the value set for the gap conductance was set to 10^5 $W/(m^2*K)$. The results are shown in Table 5-5.

Table 5-5. Coolant thermal-hydraulic features for the homogenized assembly model

Parameter	Value	Units
outlet plenum temperature	700	°C
channel 104 outlet temperature	700	°C
channel 101 outlet temperature	720	°C
channel 107 outlet temperature	720	°C
channel 108 outlet temperature	672	°C
channel 109 outlet temperature	672	°C
channel 104 mass flow rate	6.31	kg/s
channel 101 and 107 mass flow rate	1.99	kg/s
channel 108 and 109 mass flow rate	0.85	kg/s
channel 104 average flow velocity	2.09	m/s
friction pressure drop across the assembly	0.619	atm

As presented in Table 5-5, the difference with respect to the normal assembly model is not relevant; an increase in the inter-assembly outlet temperature of only a few degrees is obtained, and only for channel 108.

Looking at the surface temperatures of the fuel plates and at the right surface temperature of the left box wall (the surface involved in conduction enclosures), the temperature of the wall appears to be close to the surface temperature of the plate, meaning that the effect of conduction is relevant and the issue does not depend on the gap conductance.

5.1.3.b   Higher graphite conductivity model

In the attempt to obtain higher inter-assembly coolant temperatures, a model with increased graphite conductivities of the box wall and the Y-shape was tested.

The same formula was used for thermal conductivity as the one used for the other models, but it was multiplied by a factor 10; the form loss coefficient for inter-assembly channels' inlet junction was set to 2000 and the gap conductance to $3*10^4$ W/(m^2*K).

Table 6 shows the results for this model.

Table 5-6. Coolant thermal-hydraulic features for the high conductivity model

Parameter	Value	Units
outlet plenum temperature	700	°C
channel 104 outlet temperature	699	°C
channel 101 outlet temperature	719	°C
channel 107 outlet temperature	723	°C
channel 108 outlet temperature	677	°C
channel 109 outlet temperature	684	°C
channel 104 mass flow rate	6.35	kg/s
channel 101 and 107 mass flow rate	2.00	kg/s
channel 108 and 109 mass flow rate	0.74	kg/s
channel 104 average flow velocity	2.10	m/s
friction pressure drop across the assembly	0.623	atm

The outlet temperature of outside channels now is higher but still about 20°C lower than the average outlet temperature (700°C). It can be shown that the power carried out by inter-assembly flow in this case is about 2.5% of the total power produced by an assembly.

5.1.3.c   Some considerations on the first models

The smaller inside channels (101 and 107) are always hotter (20°C) than the other inside channels; in addition, the channel 107 is 3-4°C hotter than the 101, because it is heated by the Y-shape, which is hotter than the outside lower box wall.

Consequently, the fuel plate near to the Y-shape is hotter than the other fuel plates.

The outside channels (108 and 109) are colder (20°C) than the inside channels and the channel 109 is hotter than the 108, since the left box wall (in direct contact with fuel plates) is hotter than the lower box wall.

The model (as well as its modifications presented in section 5.1.3) presents an issue regarding the modeling of the heat conduction and the heating of the box wall, which was not solved by the modifications of the model presented in section 5.1.3.

A substantial modification of the model is required, in order to be able to give a better description of the heat conduction in the assembly structure; this modification will be presented in the next section.

5.1.4 Assembly model: evaluation of the structure of the fuel plate

The previous RELAP5 model was characterized by an issue related to the fact that the heat conduction between fuel plates and box walls occurred through the outside surfaces of the heat structures.

This means that the inside wall surface is in contact with a 100°C cooler surface than the real condition, in which this surface is heated mainly by the lateral sides of the graphite meat.

Figure 5-6 shows an example of transversal temperature distribution (blue line): we can see that the average temperature is almost equal to the temperature of the graphite meat; for this reason it would be more realistic to connect the wall directly to the graphite meat boundaries and not to the plate surface. This is the improvement introduced in the new model: the conduction to the assembly walls is increased since they are connected directly to the graphite meat and not to the plate surfaces.

The overall structure of the new model is the same of the previous model, whose features are summarized in section 5.1.1 and a top view is given in Figure 5-3.

The fuel plate structure was modified as follows:

- The number of transversal intervals was unchanged;
- The number of heat structures was increased from 1 to 3: 1 for the left fuel stripe and associated sleeve; 1 for the graphite meat; 1 for the right fuel stripe and associated sleeve;
- The right surface of the left fuel stripe and the left surface of the graphite meat were connected in a conduction enclosure; the same approach was adopted for the right surface of the graphite meat and the left surface of the right fuel stripe;

Figure 5-7 shows the old and the new heat structure (blue arrows indicate surfaces connected in the same conduction enclosure).

In this new fuel plate model the graphite meat surfaces and the inner fuel stripes' surfaces, which were inner surfaces in the previous model and could not be connected to a conduction enclosure, now become external surfaces, to which we can connect the box walls.

Figure 5-8 shows how each fuel plate is connected to the box walls into a conduction enclosure.
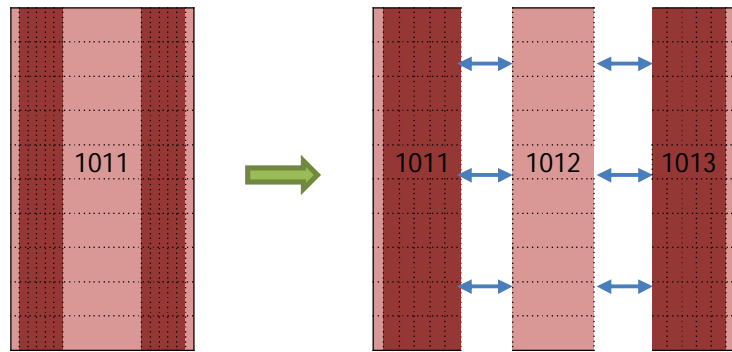
Figure 5-7. Axial view of the initial and modified fuel plate configuration
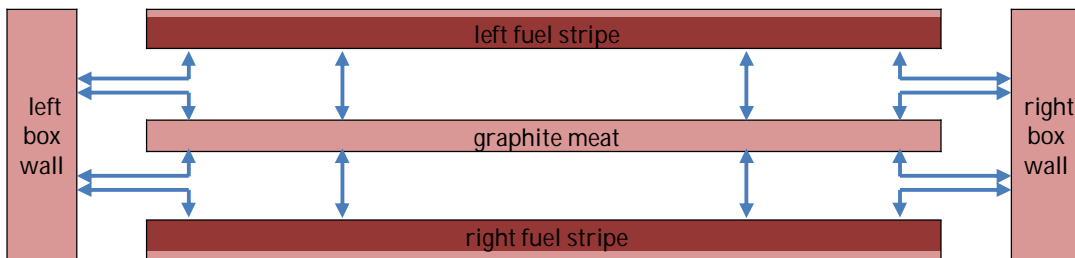
Figure 5-8. Top view of the conduction enclosure connections for a single fuel plate

This configuration is repeated for each fuel plate; other connections are then created to connect the following pairs of heat structures (unchanged with respect to the previous model):

- Left wall inner surface and lower wall inner surface;
- Left wall outer surface and lower wall outer surface;
- Right wall inner surface and lower wall inner surface;
- Right wall inner surface and lower wall outer surface;
- Right wall inner surface and upper wall lower surface;

The lower wall has double conductive connections, for both the inner and outer surface, in order to obtain a better modeling of conduction with the left and right walls.

5.1.5 Results for the modified assembly model

5.1.5.a Coolant thermal-hydraulic features

Table 5-7 shows the results for a steady-state simulation.

The thermal hydraulic features of the channels are substantially similar to the results from the previous assembly model.

As presented in Table 5-7, the mass flow rate of an intra-assembly channel (neither the first (101), nor the last (107), but one of the middle channels) is 6,3 kg/s. Since the flow area of the

first and the last channel is half the flow area of an intermediate channel, their flow rate is expected to be about half the flow rate of an intermediate channel, but Table 5-7 shows that it is 2.0 kg/s, 2/3 of the expected value. So the expected temperature drop across the first or the last channel will be 50% higher (multiplied by a factor equal to 3/2) than the reference temperature drop (50°C), that is to say that the outlet temperature of the first and last channel should be at least 725°C.

Table 5-7. Coolant thermal-hydraulic features (model with conduction through graphite meat)

Parameter	Value	Units
outlet plenum temperature	700	°C
channel 104 outlet temperature	697	°C
channel 101 outlet temperature	729	°C
channel 107 outlet temperature	734	°C
channel 108 outlet temperature	676	°C
channel 109 outlet temperature	695	°C
channel 104 mass flow rate	6.31	kg/s
channel 101 and 107 mass flow rate	2.00	kg/s
channel 108 and 109 mass flow rate	0.85	kg/s
channel 104 average flow velocity	2.09	m/s
pressure drop across the core	1.793	atm
friction pressure drop across the assembly	0.619	atm

Looking at Table 5-7, this condition is satisfied and the outlet temperature of these two channels is even higher. In fact there is another contribution that causes this outlet temperature to be even higher: the first and the last channel are heated by the respective fuel plate, but also by the lower and higher box walls, respectively. Furthermore, the outlet temperature of channel 107 is higher than the outlet temperature of channel 101, because the Y-shape is reasonably expected to be hotter than the lower box wall.

In relation to the inter-assembly channels (108 and 109), channel 108 reaches the same outlet temperature (~700°C) as the intra-assembly channels, while channel 109 is colder (outlet temperature equal to 676°C). This is due to the fact that in this model the left wall is hotter (directly heated by fuel plates) than the lower wall (heated by the left and right wall).

In a realistic situation the temperature of the two channels will not be really different: while in this model we are considering only a half of the inter-assembly channel (the other half is associated to the nearby fuel assembly), in the real core a hotter face of an assembly will be faced to a colder face of another assembly, so the temperature of the inter-assembly coolant would be averaged.

The power carried by inter-assembly flow can be obtained from Table 5-7 data; it can be shown that it is 3.4% of the total thermal power.

5.1.5.b   Temperature distribution of the main heat structures

The next tables show temperature values for the heat structures at the sixth axial level (mid-plane of the core).

Table 5-8. Wall temperatures [°C] at the sixth axial level (model with conduction through graphite meat)

	lower wall	right wall	upper wall	left wall
left/lower	704	819	-	750
right/upper	704	-	709	816

Table 5-9. Fuel plates' temperatures [°C] at the sixth level (model with conduction through graphite meat)

	plate 1	plate 2	plate 3	plate 4	plate 5	plate 6
lower surface	746	721	721	721	721	721
maximum	839	829	829	829	829	839
upper surface	721	721	721	721	721	747

Table 5-8 shows that the temperatures of the surfaces that are in contact with fuel plates are near to the maximum temperature of the fuel plate; the left wall is hotter than the lower wall and the lower wall has a similar value of temperature for the upper and lower surface.

The temperature drop across the Y-shape is approximately 100°C, while the temperature drop across the left wall is 76°C.

All the fuel plates have similar temperature values (consistent with those obtained through the MATLAB model, slightly lower because of the different power distribution and the effects of conduction enclosures), except the lower and the upper plate, which are in contact with hotter channels 101 and 107.

A similar behavior is expected for other axial levels.

5.1.5.c   Model with single inter-assembly channel

As previously mentioned, the temperature distribution of the two outside channels is almost the same (assuming normal operating conditions), since both of them are connected to similar heat structures.

This model considers only one third of the fuel assembly, so it does not account for the fact that there are other assemblies near to the reference one. A simple way to avoid this issue is to set up

a single channel with a full cross-sectional area, instead of two separated channels with half cross section.

The results for this model are presented in the final section (section 5.1.6.c).

5.1.6 Simplifications of the fuel assembly model

5.1.6.a Simplification #1: single fuel plate and inter-assembly channel

The previous sections showed that the six fuel plates have a similar behavior inside the box, so the first simplification consists of the use of a single larger (larger heat transfer area) fuel plate. This simplification is required in order to be able to make a model composed of more than one assembly or a core model, since RELAP5 allows using only up to 100 conduction enclosures (a way to reduce the number of conduction enclosures is needed).

Figure 5-9 shows the new configuration of the hydraulic components.
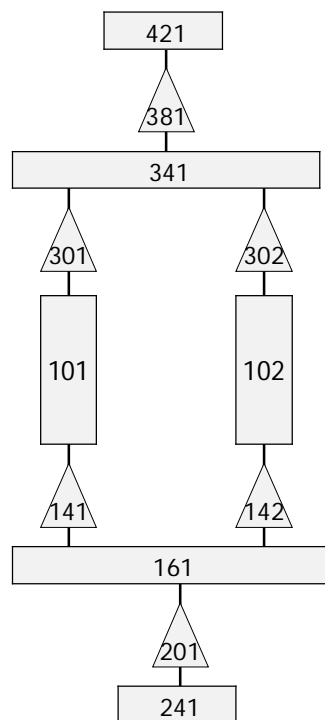
Figure 5-9. Nodalization diagram of the simplified model with single fuel plate and inter-assembly channel

The inside flow is represented through a single channel (101), whose flow area and hydraulic diameter are the intra-assembly flow area and the overall intra-assembly hydraulic diameter; channel 102 is the outside channel, connected with both the left and lower box wall; component 201 is a time-dependent junction which regulates the mass flow rate.

Figure 5-10 shows a top view of the model:

- The blue line connects a couple of surfaces belonging to the same conduction enclosure;
- The red line connects a surface to an hydrodynamic volume;
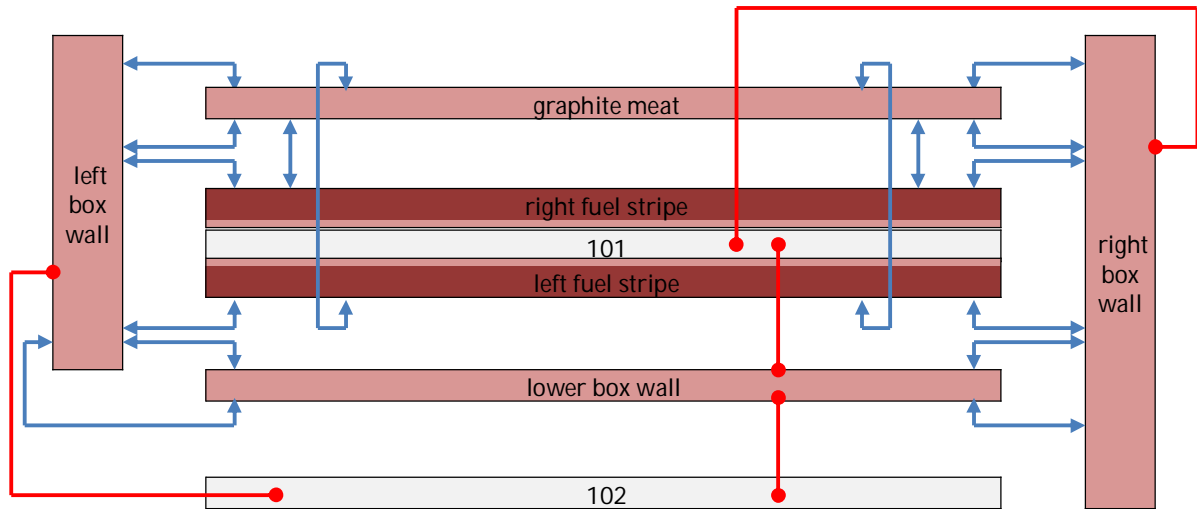
Figure 5-10. Top view of the simplified model with single fuel plate and inter-assembly channel

The results of the steady state simulation are presented in Table 5-10.

Table 5-10. Coolant thermal-hydraulic features for the simplified model with single fuel plate and inter-assembly channel

Parameter	Value	Units
outlet plenum temperature	700	°C
channel 101 outlet temperature	702	°C
channel 102 outlet temperature	682	°C
channel 101 mass flow rate	35.48	kg/s
channel 102 mass flow rate	1.75	kg/s
channel 101 average flow velocity	1.96	m/s
pressure drop across the core	1.831	atm
friction pressure drop across the assembly	0.669	atm

The outlet temperature of the inter-assembly channel is between the temperatures obtained for the two inter-assembly channels of the complete model; the mass flow rates are shared between the intra-assembly and inter-assembly flow in the same way as in the complete model.

The average velocity is lower than the velocity of a middle channel in the complete model: in the complete model the middle channels presented higher velocity than the lower and upper channels, but in this case all the mass flow rate must have the same average features, so the velocity value is an average value.

The pressure drop is slightly (0.05 bar) increased.

The power carried by inter-assembly flow is 2.9% of the total power produced (0.5% less than the complete model).

The next tables show temperature values for the heat structures at the sixth axial level.

Table 5-11.Wall temperatures [°C] at sixth level for the simplified model with single fuel plate and inter-assembly channel

	lower wall	right wall	upper wall	left wall
left/lower	699	821	-	747
right/upper	689	-	681	818

Table 5-12. Fuel plate temperatures [°C] at sixth axial level for the simplified model with single fuel plate and inter-assembly channel

	fuel plate
lower surface	724
maximum	832
upper surface	724

Table 5-12 shows the temperatures of the fuel plate, which are similar to the temperatures obtained for the complete model; since only one fuel plate is implemented in the model, the effect of overheating of the lower and upper plates is not detectable.

Table 5-11 shows the temperatures of the box wall; the main difference with the complete model is in the smaller value of the inner surface temperature of the lower and upper walls, in contact with the smaller (hotter) channels.

In order to solve this problem, eventually RELAP allows using a multiplicative factor to reduce the heat transfer coefficient for the inner boundary of the lower box wall. This would lead to a temperature profile, for the lower box wall, more similar to the profile obtained from the complete model of section 5.1.5.

5.1.6.b   Simplification #2: single fuel plate and single lower-left outside wall

Starting from the previous model, a simpler model was developed by joining the two heat structures that represent lower and left box wall into a single heat structure; all the other features were preserved.

The results obtained with this model were not satisfactory in both the two tested configurations:

1- In the first configuration the inner lower-left wall surface was completely joined to the channel: this means that the exchange surface between the coolant and the lower-left wall surface is higher than in the case of complete model, in which only the lower wall could exchange power directly with the coolant. The issue with this model was that,

since the convective heat transfer with the inner coolant was enhanced, the temperatures of fuel plates and inner walls were too low.

2- In the second configuration the inner-lower wall surface does not exchange power with the inner coolant. In this case the power carried by the inter-assembly coolant was found to be ~5%, higher than in the complete model case. This overcooling capacity of the outside channels might not be realistic.

5.1.6.c   Issues and possible solution: single outside channel

The complete model seems to give a good representation of the behavior of the assembly; further analysis is required to understand the following aspects:

- Relevance of the cross flow in the outside channels;
- Effects on the outside channel coolant due to the heating from two surfaces of two different assemblies.

In relation to the first issue, the difference, in terms of temperature and other properties, between two connected inter-assembly channels, for each axial level, will not be relevant, so we can assume that the cross-flow between two adjacent outside channels is negligible.

Even if it was not negligible, the amount of coolant going out of an inter-assembly channel would be compensated by an equal amount of coolant with similar thermal features incoming from the nearby inter-assembly channel and the overall result would be the same as if any cross-flow was present.

In relation to the second issue, with reference to the complete model, the inter-assembly channels were modeled as two separate channels (which is reasonable in terms of cross-flow) with a thickness which is a half of the inter-assembly gap; Figure 5-11 shows the configuration for the outside channels. As shown in Figure 5-11, channels 108 and 109 can reasonably be considered separately (the effective spacing between assemblies is smaller than in figure 7); however, channel 108 cannot be considered separate from channel 110, as well as channel 109 cannot be considered separately from channel 111. It can be observed that, since adjacent assemblies presumably have similar temperature distributions, channel 109 is similar to channel 110 (they receive heat from the hotter part of the box wall, the part attached to the fuel plates) and channel 108 is similar to channel 111 (colder box wall).

For this reason, in order to obtain a good modeling of the outside channels, it is reasonable to use a single outside channel, whose flow area is the sum of the flow area of channels 108 and 109, the hydraulic diameter remains the same, and the two box walls (the left, which is hotter, and the lower which is colder) are both connected to the channel.
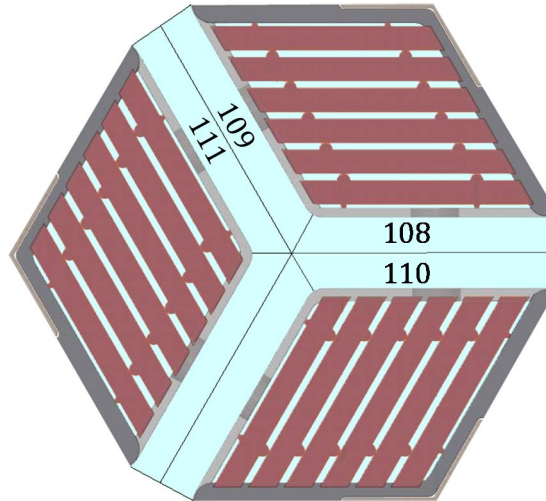
Figure 5-11. Inter-assembly channels configuration

In relation to the inter-assembly flow modeling, this is the same solution that was already adopted for the simplified model #1 in section 5.1.6.a, so the simplification #1 is expected to be a good approximation of the real behavior. In the following tables the results for the complete initial model, with only one outside channel, are shown.

Table 5-13. Coolant thermal-hydraulic features (complete model with single outside channel)

Parameter	Value	Units
outlet plenum temperature	700	°C
channel 104 outlet temperature	697	°C
channel 101 outlet temperature	730	°C
channel 107 outlet temperature	734	°C
channel 108 outlet temperature	686	°C
channel 104 mass flow rate	6.31	kg/s
channel 101 and 107 mass flow rate	2.00	kg/s
channel 108 mass flow rate	1.7	kg/s
channel 104 average flow velocity	2.09	m/s
pressure drop across the core	1.793	atm
friction pressure drop across the assembly	0.619	atm

Outlet temperature values (Table 5-13) are similar to the values obtained for the initial complete model; the outlet temperature of the outside channel is 686°C. The wall temperatures are shown in Table 5-14; the only difference with the previous model is the fact that the lower wall inside surface is now 2°C hotter and the left wall is few degrees colder. Table 5-15 shows the temperatures of fuel plates: there is no substantial difference with respect to the original model.

Table 5-14. Wall temperatures [°C] at 6th axial level (complete model with single outside channel)

	lower wall	right wall	upper wall	left wall
left/lower	706	819	-	747
right/upper	704	-	709	815

Table 5-15. Fuel plates' temperatures [°C] at 6th axial level (complete model with single outside channel)

	plate 1	plate 2	plate 3	plate 4	plate 5	plate 6
lower surface	746	721	721	721	721	721
maximum	839	829	829	829	829	839
upper surface	721	721	721	721	721	747

The total power carried by inter-assembly flow is, in this case, 3.28% of the total power produced.

This model gives a better description of the assembly behavior than the initial complete model, but it is still too complex to be used in a core model. As mentioned above, the simplification #1 is a good way to obtain a simpler model by reducing the number of plates from 6 to 1; results obtained in this way are very similar to those obtained in the last model, the only difference consists of the fact that the lower wall is colder in the simplified model and the power carried by the outside flow is 0.4% lower. This issue was solved through the reduction of the heat transfer coefficient of the inside surface of the lower wall, to account for the fact that the temperature of the coolant in the smaller channel of the complete model is 30°C higher than the average coolant temperature.

A multiplicative factor equal to 0.2 was adopted and the results were satisfactory:

- The outlet temperature of the outside channel was higher, about 685°C (for the complete model it is 686°C);
- The average temperature of the lower box wall was higher, similarly to what was obtained with the complete model.

5.1.7 Considerations on the fuel assembly model

The complete fuel assembly model presented in section 5.1.6.c gives a good description of the overall behavior of the fuel element. However, a simplified model is required for the implementation in a full core model, in order to reduce the computational demand. For this purpose, a simple and suitable model was identified and presented in section 5.1.6.a; the core model will be developed starting from this point.RELAP5-3D model of the AHTR core and systems.

5.2   Reactor modeling

A complete reactor system was modeled in order to account for all the factors that affect the transient behavior; in particular, the model includes the following components:

- Reactor core, core channels, permanent and removable radial reflector and lower and upper support plates;
- Lower and upper plenum;
- Barrel;
- Downcomer channels;
- Reactor vessel;
- Intermediate loop;
- DRACS loop and air circuit;

The following sections give a description of the modeling of these components.

5.2.1   Reactor core

The reactor core was modeled as a 9 annular-rings, and each annulus was modeled as a single fuel assembly; the heat exchange area of the heat structures and the cross-section of the channels were increased by a specific multiplicative factor in order to account for the fact that each modeled assembly represents more than one real assembly.

Each assembly is modeled as three units connected through the wall of the Y-shape and each unit has the following structure: a single coolant channel is heated by a single fuel plate (representing six different plates) and three heat structures are connected to the channel, two representing the outside wall and one the Y-shaped support. The features of this model are presented in section 5.1.6.a.

The new aspect that was introduced for a core model description, with respect to the assembly modeling, is the characterization of the inter-assembly flow. Three inter-assembly channels where associated to each ring:

- The first channel models the flow that is heated by the reference ring on one side and by the outer ring on the other side;
- The second channel is heated by the reference ring on both sides;
- The third ring is heated half by the reference ring and half by the inner ring.

Each of these inter-assembly channels has a specific flow area, and horizontal cross-flow between channels is allowed, since each channel is modeled as a 3D component.

Figure 5-12 shows a cross section of the reactor core.
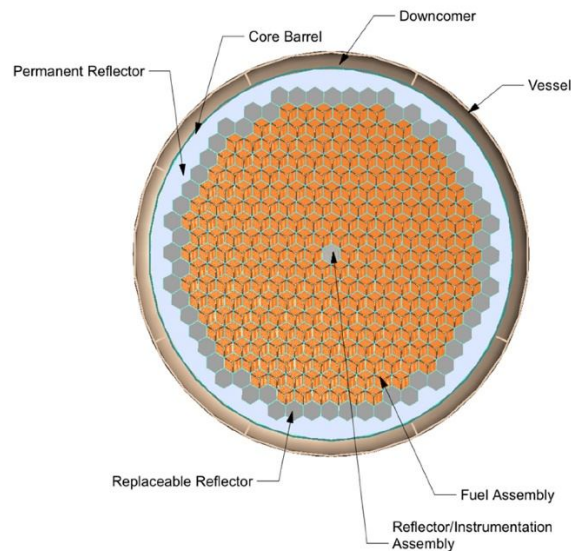
Figure 5-12. Cross section of the AHTR core[2]

5.2.2   Piping and structures

Various hydrodynamic volumes and heat structures are used to describe all the components that operate into the reactor vessel.

5.2.2.a   Hydrodynamic components

Starting from the bottom of the vessel, the inlet junctions of the core channels are connected to the lower plenum, a single volume component, shaped as a cylinder with a 10.4 m diameter and 1.2 m height; these dimensions are not reported by ORNL (the only available dimension is the outside diameter, 10.5 m), so the inside diameter was estimated by assuming a 5 cm vessel thickness and the plenum height by comparison with the pictures printed in the ORNL reports.[2]

The lower plenum is connected to the upper plenum through the intra-assembly channels, the inter-assembly channels and the channel associated to the replaceable and permanent reflector.

The part of the upper plenum contained into the barrel is modeled as a single volume cylinder with 9.58 m diameter and 6 m height; this volume is connected to the part of the upper plenum which is in contact with the Argon plenum: this component is still a cylinder, with a 1 m height and 10.4 m diameter (not limited by the barrel).

The downcomer region is divided into seven circular sections, and one channel is associated with each region; each downcomer channel is a 3D component characterized by an inner radius (4.81 m, outer vessel), an outer radius (5.2 m, inner vessel) and an angle (53.85° for the downcomer, 36.5° for the DRACS and 88.95° for the refueling lobe) which defines the arc of circumference.

100

The downcomer region has the following features:

- The DRACS channels are connected both to the upper and the lower plenum;

- The downcomer and refueling lobe channels are connected only to the lower plenum;

- For each downcomer channel, a pipe coming from the PHX injects the flow at the top of the channel;

- Each DRACS channel is partly connected to a DRACS heat exchanger.

5.2.2.b   Heat structures

Heat structures have been used to model the radial reflector, the barrel and the reactor vessel.

The radial reflector is composed of two heat structures, the innermost representing the replaceable reflector and the outermost representing the permanent reflector (Figure 5-12).

The replaceable reflector consists of a cylindrical heat structure with both inner and outer sides connected to a cooling channel; the inner radius is given by the equivalent core radius (3.905 m), which is the radius of the circle with area equal to the sum of the areas of all the assemblies and channels into the core; the outer radius is the equivalent radius of the fueled region plus the area of the 60 removable reflector assemblies and it is equal to 4.315m.

The permanent reflector is modeled as a hollow cylinder with inner diameter equal to the outside diameter of the removable reflector and outer diameter equal to the total core diameter, which is 9.56 m;[2] the inner side is connected to the removable reflector cooling channel, the outer side is connected to a 1 cm thick channel which separates it from the barrel.

The barrel is divided into seven sections, corresponding to the seven downcomer regions, and each surface is connected to the two adjacent surfaces through a conduction enclosure, in order to account for the heat conduction of the structure.

Each surface is approximated as a plate surface since the thickness, compared to the other dimensions, is small; the thickness is 2 cm and the width is 4.5 m for the downcomer region, 3.05 m for the DRACS region and 7.43 m for the refueling lobe (these values correspond to the angles given in the previous section for the downcomer channels). The total height of the barrel is 12.7 m: 6 m for the core, 0.7 m for the upper and lower support plate and 6 m for the upper plenum. Each section is connected on the left side to the permanent reflector channel and the upper plenum and on the right side to the correspondent downcomer channel.

The reactor vessel is modeled as a hollow cylinder with two rings: the inner ring is similar to the barrel, since it consists of seven angular sections connected through a conduction enclosure, but the width of the seven heat structures is larger because of the larger diameter (10.4 m); the outer ring is a single hollow cylinder.

The inner diameter of the first ring is 10.4 m, the outer diameter of the first ring is 10.44 m and the outer diameter of the second ring is 10.5 m, so the total vessel thickness is 5 cm; the connection between the two rings is modeled through a conduction enclosure.

The left surface of each section of the inner ring is connected to the respective downcomer channel and the outer surface of the outer ring has a zero flux boundary condition.

5.2.3   Heat removal system

The primary heat removal during normal reactor operation is provided by three PHX located in three different sections of the downcomer, which transfer the heat from the primary circuit to three intermediate loops.
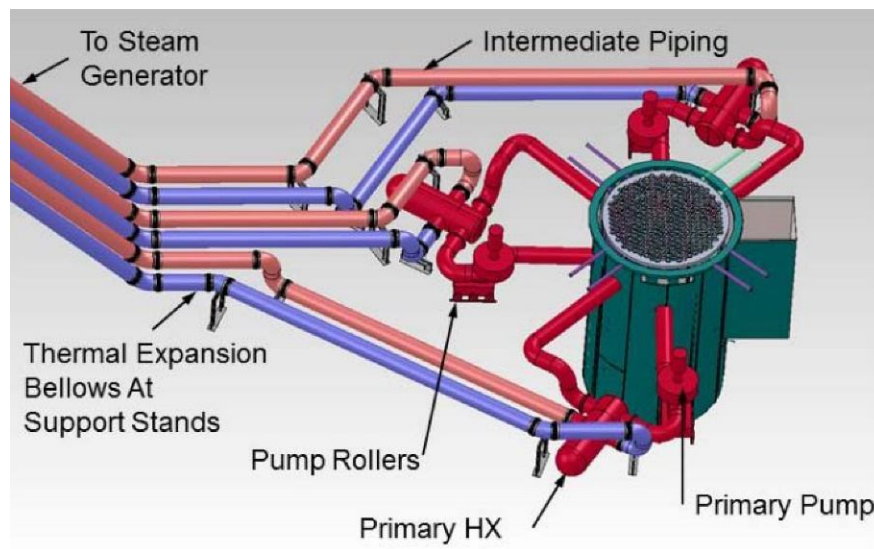
Figure 5-13. AHTR heat removal system layout[2]

The layout of the cooling system is shown in **Error! Reference source not found.**; considering a single loop, the following components are presented in the figure:

- Primary side (red), including outlet vessel pipe, PHX, pump and inlet vessel pipe
- Cold leg of the intermediate side (blue)
- Hot leg of the intermediate side (rose)

The primary piping interior diameter is 1.24 m and the pump, modeled as a time-dependent junction, is located in the middle of the outlet pipe of the exchanger (which is the vessel inlet pipe).

The heat exchanger is a straight-tube shell-and-tube counterflow horizontal type exchanger and the piping material is alloy 800H with Hastelloy N lining; the heat exchanger was modeled as a

cylindrical heat structure connecting the two sides (primary on the tube side and intermediate on the shell side) of the system.

An accurate design of the PHX is not yet available, so dimensions and number of tubes were estimated on the basis of the design of the PB-AHTR IHX[20] and the SmAHTR PHX[3].

The PB-AHTR IHX design has a small pipe diameter (OD=0.9525 cm), which results in a high pressure drop across the exchanger, so a larger value was selected; the SmAHTR PHX design has a large pipe diameter and thickness (2.54 cm and 0.16 cm, respectively), which results in a lower pressure drop but worse heat exchange performance, so a smaller value was selected.

The number of tubes was then optimized in order to obtain the correct amount of power removed by the cooling system, which is one third of the total core power per each intermediate loop; a summary of the PHX design features used for this study is given in Table 5.16.

Table 5.16. PHX modeling parameters

Parameter	Value	Units
Tube outer diameter	2	cm
Tube wall thickness	0.1	cm
Tube inner diameter	1.8	cm
pitch/tube outer diameter	1.25	-
pitch (triangular)	2.5	cm
Tube-side hydraulic diameter	1.8	cm
Shell-side hydraulic diameter	1.448	cm
Tube-side flow area	2.5434	m^2
Shell-side flow area	2.273	m^2
Tube height	22	m
Number of tubes	10000	-

Since KF-ZrF$_4$ properties are not implemented in RELAP5, a similar coolant, NaF-ZrF$_4$ (which is implemented in RELAP5), was selected for the intermediate loop.

The mass flow in the shell-side of the heat exchanger is driven by a pump (time-dependent junction), which takes the fluid from an inlet time-dependent volume; the outlet flow is collected into an outlet time-dependent volume. The intermediate heat exchanger (IHX) and the supercritical steam power loop are not modeled.

5.2.3.a   Test for the modeling of the cooling system

In the previous paragraph the main design parameters of the PHX were presented, as implemented in the core model; this model was tested by selecting one of the three loops and the following boundary conditions to simulate the reference steady state operation:

- Inlet salt tank (time-dependent volume) at 700°C and 1 atm (representing the upper plenum of the AHTR core), connected through a single junction to the inlet pipe of the PHX;

- Outlet salt tank (time-dependent volume) at 1 atm (representing the first volume of the downcomer channel); a single junction connects the pipe coming out from the pump to the tank.

The nodalization diagram of the model used to test the cooling system capability is shown in Figure 5-14.
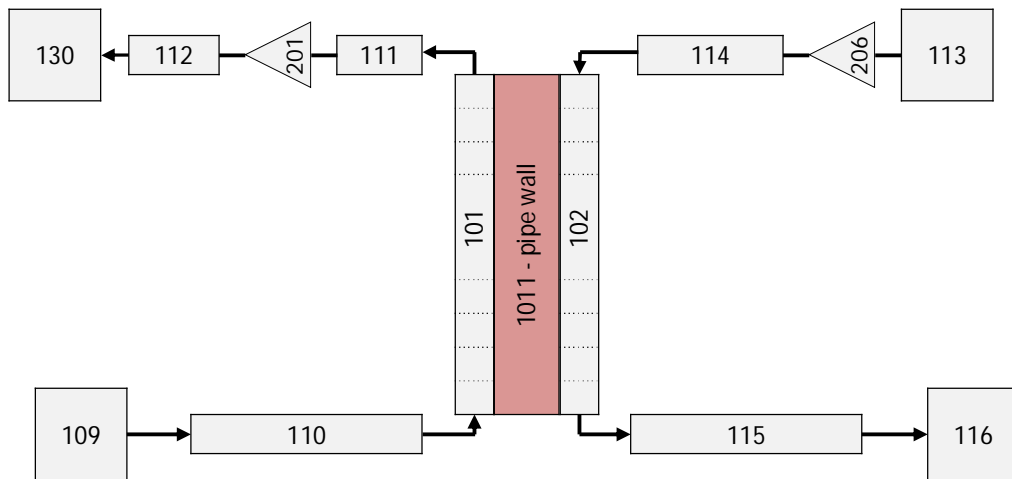
Figure 5-14. Nodalization diagram of the test model for the cooling loop and the PHX

The primary loop is formed by: a time-dependent volume (109) at 1 atm and 700°C, a pipe (110), the tube-side of the PHX (pipe 101), a pipe (111), the primary pump (time-dependent junction 201, 9400 kg/s), a pipe (112) and the outlet tank (time-dependent volume 130 at 1 atm).

The pipe wall separates the primary loop from the intermediate loop, which is formed by: an inlet tank (time-dependent volume at 1 atm and 600°C), a pump (time-dependent junction 206, 12800 kg/s), a pipe (114), the shell-side of the PHX (pipe 102), a pipe (115) and the exit tank (time-dependent volume 116 at 1 atm).

The cooling loop as implemented in the complete core model is identical to the test model, except for the fact that the volume 109 is replaced by the upper plenum and the volume 130 is replaced by the top volume of the downcomer channel.

Since the objective of the study is the core system (not the intermediate loop) and in order to reduce the dimension of the output file, the following option was adopted for the core model: a single bigger intermediate loop was implemented, instead of three separated identical loops.

Figure 5-23 shows the typical temperature profiles obtained from a steady state simulation. The primary coolant (FLiBe) is cooled from 700°C to 650°C and the intermediate coolant is heated

from 600°C to 675°C; these values are in good agreement with the design values provided by ORNL.[6] The intermediate coolant used in this model is different from the coolant selected by ORNL, but the results presented in Figure 5-23 show that the difference is negligible, since the outlet temperature of the intermediate coolant is almost the same outlet temperature calculated for the reference fluid by ORNL.

5.2.4 DRACS

The DRACS provides heat removal during accidental transients; it is formed by the DRACS loop and the air circuit: the power is removed from the core by the DRACS exchangers, carried by the DRACS loop to the salt-to-air heat exchanger and transferred to the air circuit, which is the ultimate heat sink.

The design of the DRACS of the AHTR is still not well defined so the dimensional parameters were determined looking at the overall description of the system given by ORNL[2, 6] and at the design parameters of the DRACS of the SmAHTR[3].

Neither KF-ZrF$_4$ nor atmospheric air are implemented in RELAP5, so NaF-ZrF$_4$ (the same as the intermediate loop) and pure nitrogen were selected as working fluids for the DRACS and air loop, respectively.

The pipe diameter for the DRACS loop is 0.62 m (half of the primary piping diameter); the DRACS exchanger is a straight-tube shell-and-tube counterflow vertical type exchanger, with primary fluid (FLiBe) on the shell side and intermediate fluid on the tube side.

The dimensional parameters of the DRACS exchanger are given in Table 5.17.

Table 5.17. DRACS exchanger modeling parameters

Parameter	Value	Units
Tube outer diameter	1.27	cm
Tube wall thickness	0.1245	cm
Tube inner diameter	1.021	cm
pitch/tube outer diameter	1.25	-
pitch (triangular)	1.5875	cm
Tube-side hydraulic diameter	1.021	cm
Shell-side hydraulic diameter	0.9192	cm
Tube height	3.5	m
Number of tubes	5468	-

The salt coming out from the DRACS exchanger flows up to the salt-to-air exchanger through a 12 m high pipe which provides the gravitational pressure difference required for natural circulation operation; then it flows downward through the 2 m high salt-to-air exchanger and finally it is injected at the entrance of the DRACS exchanger, closing the loop.

The air circuit consists of two time-dependent volumes, two pipes and the exchanger. The two time-dependent volumes are located at the same height (12 m, which is the height of the cooling tower) with respect to the lower face of the salt-to-air exchanger and serve to keep the pressure and the temperature of the air outside the DRACS cooling tower at 1 atm and 20°C, respectively. One of the two volumes is connected to the inlet of the salt-to-air exchanger, on the shell-side, while the other volume is connected to the outlet of the shell-side.

The dimensional parameters of the salt-to-air exchanger are given in Table 5.18.

Table 5.18. Salt-to-air exchanger modeling parameters

Parameter	Value	Units
Tube outer diameter	1.995	cm
Tube wall thickness	0.1652	cm
Tube inner diameter	1.6646	cm
pitch/tube outer diameter	1.25	-
pitch (triangular)	2.49375	cm
Tube-side hydraulic diameter	1.6646	cm
Shell-side hydraulic diameter	1.4439	cm
Tube height	2	m
Number of tubes	15000	-

Air flows upward in the shell-side and salt flows downward in the tube-side; the system was set so that, when the temperature of the primary coolant in the downcomer DRACS channel is 700°C, the power removed is about 8 MW per loop.

5.2.4.a   Test for the modeling of the DRACS

A single DRACS loop is required to remove a maximum of 8.75 MW,[6] so the geometric parameters were adjusted in order to obtain this condition.

The single loop model described in the last section was integrated with a simplified model of the core and the downcomer channel; Figure 5-15 shows the nodalization diagram of the model used for the test.

Hydrodynamic components from 101 to 106 represent the simplified primary system: the core (channel 105) with the power source (1011), the salt volume over the core (106), the downcomer channel (103) as modeled for the complete core model, the upper (101) and lower (104) plenums and a time-dependent volume that keeps the pressure in the upper part of the vessel at 1 atm. The remaining part of the model (from the DRACS exchanger to the air loop) is structured as described in the previous section 5.2.4.

Different simulations were run in order to test the capability of heat removal; the initial condition of the core system is the steady-state operating condition. Different power levels were considered, but the initial selected value was 8.75 MW (per loop).
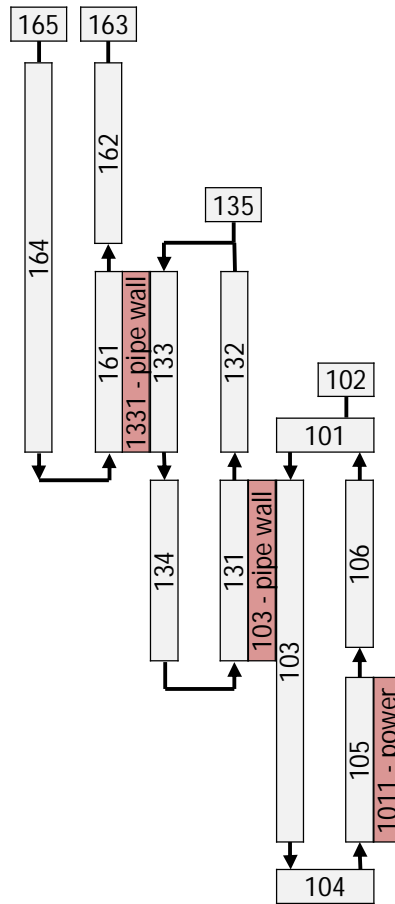

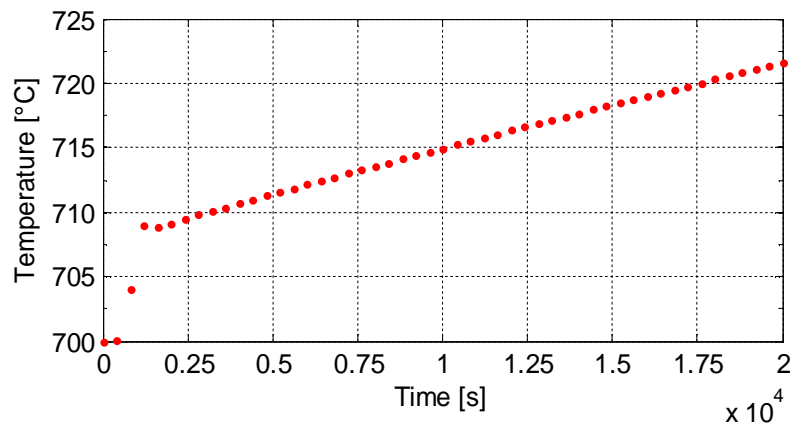**Figure 5-15. Nodalization diagram of the DRACS test model**

Figure 5-16. Temperature variation in the upper plenum

Figure 5-16 shows the temperature variation in the upper plenum when the power produced in the core is 8.75 MW. As shown in the figure, the temperature increases by about 1°C every 1000 s, but two aspects must be considered:

- 8.75 MW is the maximum heat removal capability expected for this design, but a lower value could be tolerated;

- In this simulation the power is constant, but in a real situation the decay power is not, so it is acceptable the fact that, at least in the first period of the transient, the power removed by the system is lower than the power produced in the core.

A similar simulation was run and the power level was changed to 8 MW; in this condition the temperature of the upper plenum decreases, so this means that the optimum value of maximum power that can be removed by the system, as it is structured in our model, is located between 8 and 8.75 MW.

For the last reason the model was considered suitable to be used in the complete core model, even if the requirements are not fully met. In the next figures the typical temperature profiles in the two heat exchangers of the system are shown, after 20000s at 8.75 MW.
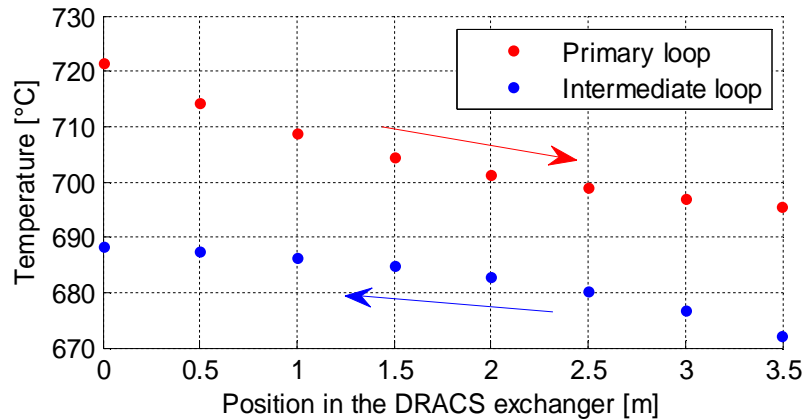

Figure 5-17. Temperature profiles in the DRACS exchangers (20000 s, 8.75 MW constant power)
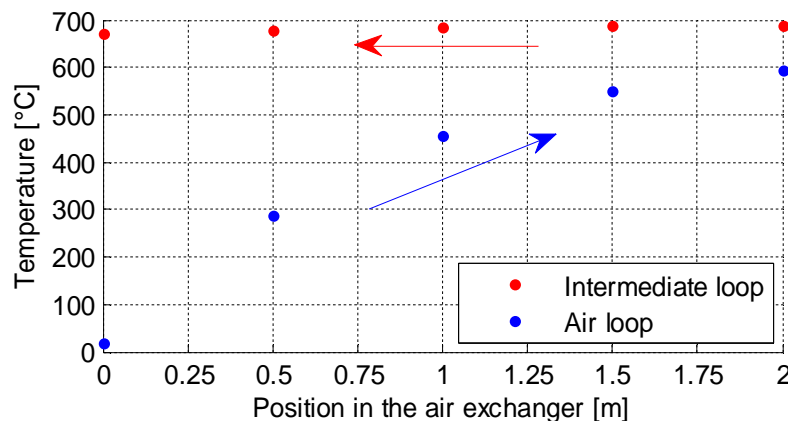

Figure 5-18. Temperature profiles for the air exchanger (20000 s, 8.75 MW constant power)

The mass flow rates circulating in the three loops (after 20000 s) are: 136 kg/s in the primary loop (1/3 of the total core flow rate), 450 kg/s in the intermediate loop and 13.2 kg/s in the air loop.

5.3   RELAP5-3D model of the AHTR reactor: steady state conditions

The model was run for 100000 s (27.8 h) at constant thermal and pumping power, in order to evaluate the steady-state conditions of the system.

Regarding the coolant features, Figure 5-19 shows the temperature distribution of the coolant, with respect to the axial and radial positions within the core; the plotted distribution is a 2D interpolation of the RELAP5 steady state simulation results.
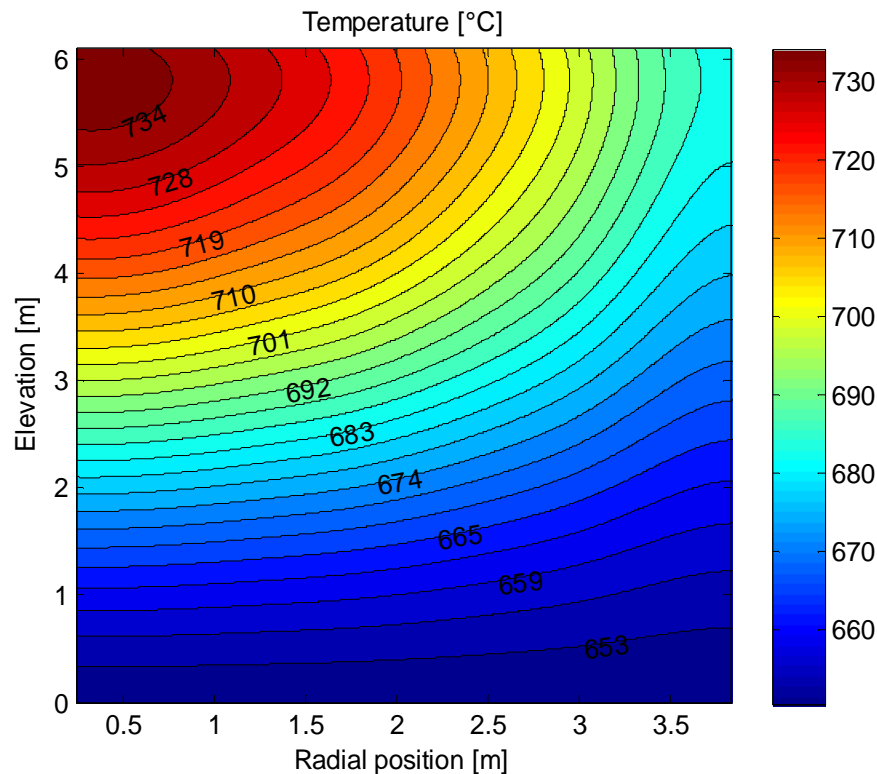
Figure 5-19. Interpolated coolant temperature distribution (steady-state conditions)

As we can see in Figure 5-19, the outlet temperature of the core is not uniform; it spans from 685°C for the outermost channel to 735°C for the central channel. While the outlet temperature depends on the radial position, the temperature profile is not affected by the distance from the centerline of the core.

Although the outlet temperature is not uniform, it spans over a relatively small range (~50°C) of temperatures, which means that a redistribution of the mass flow rate might not be required.

Figure 5-20 shows the flow velocity and the mass flow rate as functions of the radial position. Both quantities have an almost constant profile, which slightly increases from the outermost to the central ring, where the coolant is hotter and the buoyancy effects are stronger. In relation to the results obtained from single-assembly or single-channel model studies, the average value for the flow velocity obtained from the reactor model is lower (~1.8 m/s, while for the single-channel model it was ~1.96 m/s), because a certain fraction of the total reactor mass flow rate does not pass through the core, but forms a by-pass flow through the DRACS downcomer channels.
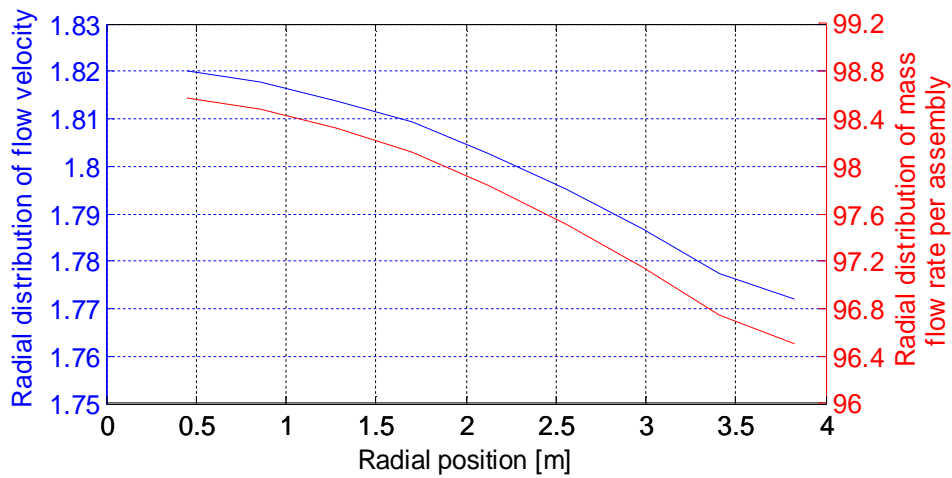
Figure 5-20. Radial profiles for the flow velocity and mass flow rate

The core pressure distribution is shown in Figure 5-21.
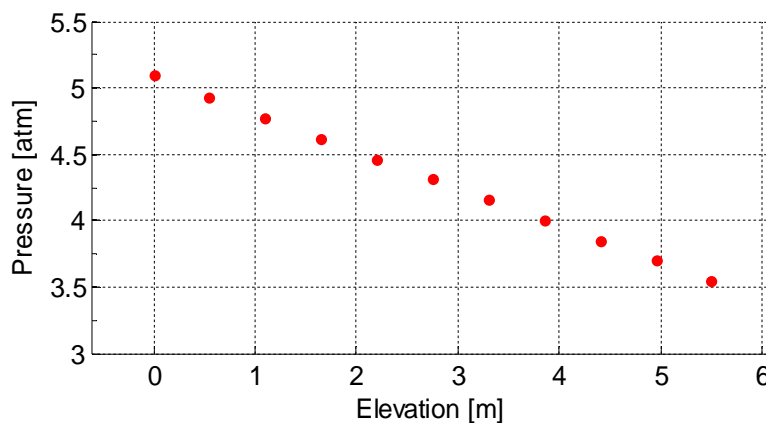
Figure 5-21. Pressure distribution with respect to the elevation from the bottom of the core

The previous figure shows that the pressure of the core has a linear dependence on the elevation; the pressure drop across the core is about 1.75 atm, of which 1.15 atm is the gravitational pressure drop and 0.6 atm is the friction pressure drop. The pressure at the

entrance of the core is relatively high because of the height of the salt plenum above the core and the high density of FLiBe, twice the density of water (5.3 m are required to increase the pressure by one atmosphere).

Figure 5-22 shows the fuel temperature of the plate as a function of the radial and axial position; for a given radial and axial position the value of temperature located at the inner face of the fuel stripe is considered, which is the maximum temperature in the direction transversal to the plate.
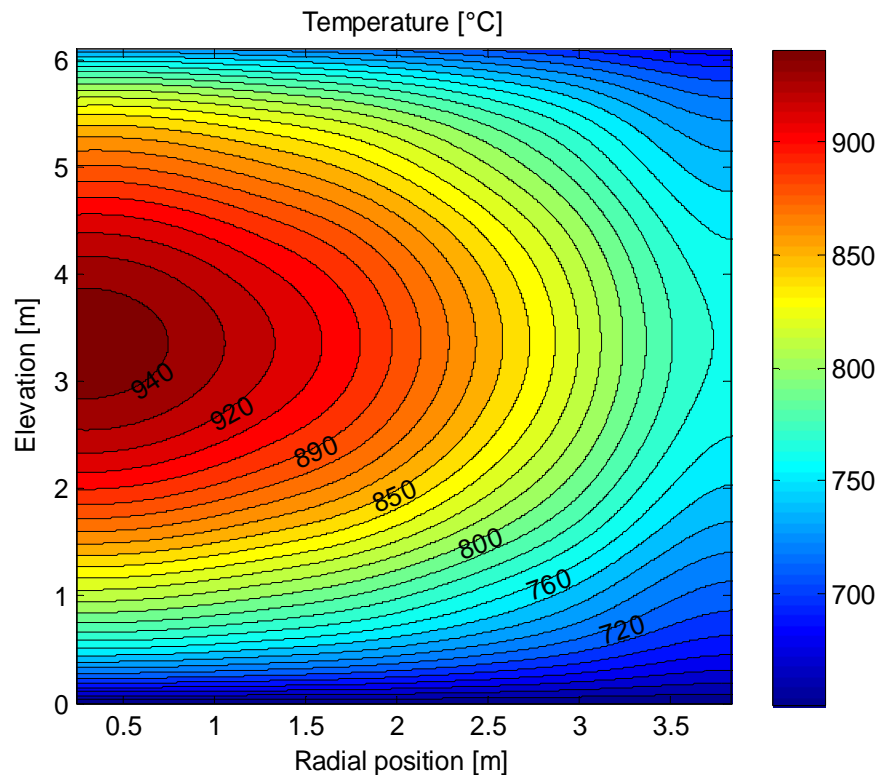

Figure 5-22. Interpolated maximum transversal fuel temperature

As it is shown in Figure 5-22, the maximum fuel temperature, in the radial direction goes from ~770°C for the outermost ring, to ~940°C for the central ring (the maximum fuel temperature for the average assembly was found to be ~843°C). The location of the axial maximum fuel temperature is not strongly affected by the radial coordinate and it is slightly above the middle of the core.

Figure 5-23 shows the temperature profiles for the primary and intermediate coolant in the PHX. The inlet and outlet temperatures for both sides of the exchanger are consistent with the nominal values given by ORNL reports.[6]

Figure 5-24 shows the temperature profiles for the primary and intermediate coolant in the DRACS exchanger. During normal operating conditions (as in this case), the flow in the DRACS downcomer channels is directed upward, so the exchanger works in parallel flow configuration, while, when the primary pumps do not work and natural circulation is activated, it works as a

counter flow exchanger. The mass flow rate in the primary side is 570 kg/s per channel, which means, considering three channels, a 1710 kg/s by-pass flow (~6% of the total mass flow rate).
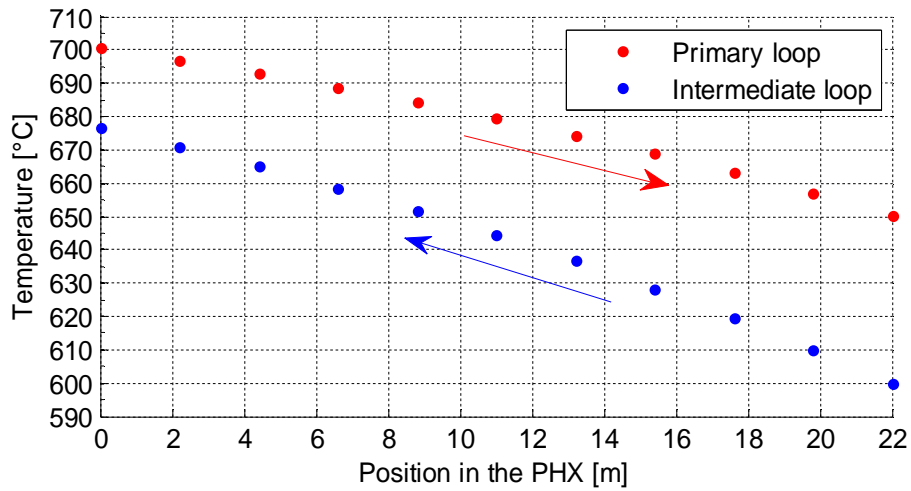
Figure 5-23. Temperature profiles for primary and intermediate coolant into the PHX
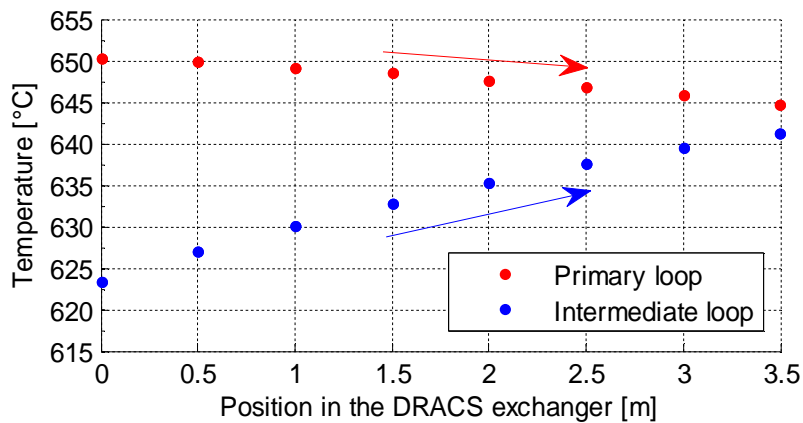
Figure 5-24. Temperature profiles for the primary and intermediate coolant into the DRACS exchanger

In the intermediate loop, the mass flow rate is 460 kg/s per channel, for a total of 1380 kg/s. Figure 5-25 shows the temperature profiles for the intermediate coolant and air in the salt-to-air exchanger. This exchanger works in counter flow configuration and the total mass flow rate is ~62 kg/s of nitrogen: since the mass flow rate for the air loop is relatively low, the temperature increase of nitrogen is very high, about 500°C.

The power lost through the DRACS system during normal operation is about 34 MW (1% of the total power).

Figure 5-25. Temperature profiles for the intermediate coolant and air into the salt-to-air exchanger

5.4   Transient behavior

5.4.1   Loss of forced cooling (LOFC) accident

The steady state simulation provides a relevant amount of information about the behavior of the system, but the model is designed for the evaluation of transients; the LOFC transient was selected as a typical accident scenario.[17]
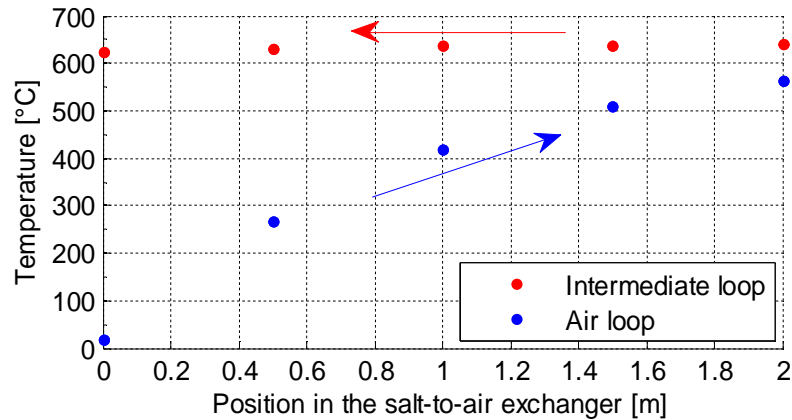
The transient has the following features:

- The initial conditions are the steady state conditions presented in the last section;
- The reactivity is decreased from 0 to -15 $ in 20 s;
- The mass flow rate produced by the pumps of the primary and intermediate loop are reduced from the nominal value to 0 in 2 minutes.

The main purpose of the simulation is the verification of the effective cooling capability of the DRACS system.

In relation to the coolant temperature, during the initial transient, the outlet temperature decreases, because the core power is reduced. Then, since the cooling capability is initially lower than the core power, the inlet temperature increases, as well as the outlet temperature. The maximum outlet temperature is 714°C at 21500 s and the maximum inlet temperature is 688 at 24500 s; the two temperatures decrease after this point and the difference between them becomes almost constant and equal to ~25°C.
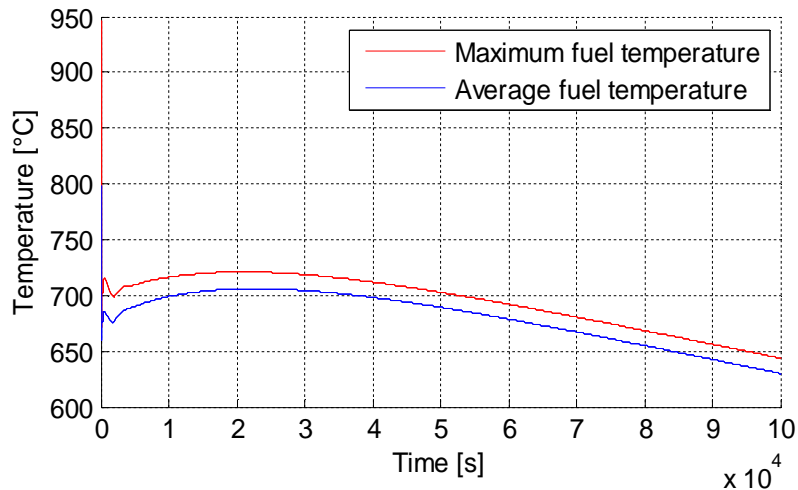
Figure 5-26. Maximum and average fuel temperature during the LOFC transient

Figure 5-26 shows the maximum and average fuel temperature dependence on time. Similarly to the coolant temperature, the maximum fuel temperature, initially 950°C, decreases to a minimum (700°C), reaches a relative maximum at 21000 s (721°C) and then decreases.

In relation to the mass flow rates (Figure 5-27), the primary mass flow rate, driven by natural circulation, initially inverts the flow direction (from upward to downward), reaches about 500 kg/s and then slightly decreases. The DRACS loop mass flow rate is initially 1330 kg/s, reaches a maximum at 21000 s and then decreases. The air mass flow rate is almost constant during the transient (about 42 kg/s).

Figure 5-27. Total mass flow rates for the primary, DRACS and air loop

Figure 5-28 shows the total core power and the power removed by the DRACS system during the LOFC transient.

114

Figure 5-28. Total core power and removed power during the LOFC transient

The capability of the DRACS system is about 25 MWth; the total core power drops below this value 26000 s (7.2 h) after the beginning of the transient; the power removed by DRACS slightly decreases with time.

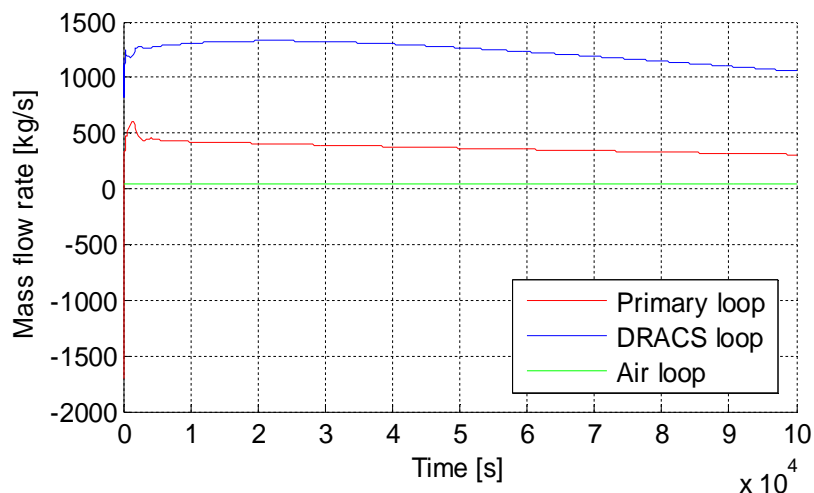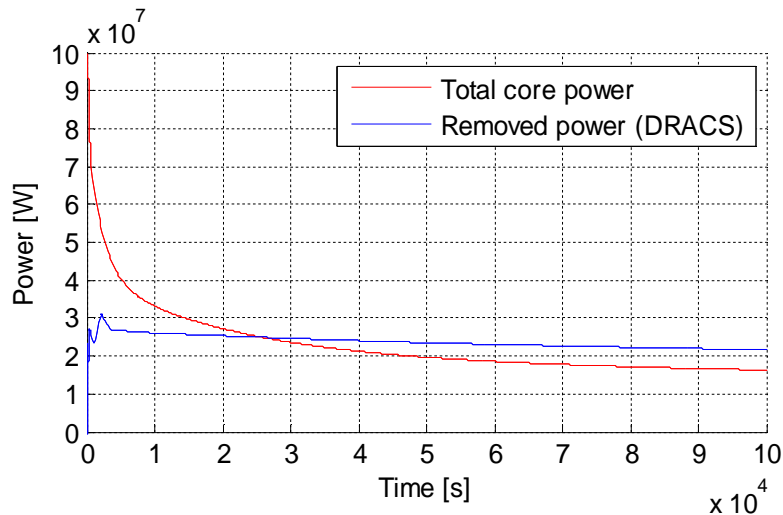As we can see from the results of the simulation, the DRACS system provides effective heat removal and the fuel temperature always remains well below the damage limits for TRISO fuel.

5.4.2   Fuel assembly removal

The AHTR core model was adapted for the modeling of the assembly removal transient. This type of transient plays an important role in the study of the AHTR reactor, enabling the possible capability for an on-line or pseudo-online refueling option.

As previously mentioned, the AHTR core presents a low heavy metal loading of the core, due to the use of TRISO fuel and graphite moderation, which reduces the amount of energy extractable from a single fuel assembly and consequently its core lifetime. If a normal refueling procedure (similarly to light water reactors) were adopted, a large amount of the reactor lifetime would be spent in off-line refueling operations, leading to a decrease in the energy delivered to the grid and to an increase of the electricity production cost.

Two reasons contribute to the previous effect: the high frequency of refueling operation pauses, due to the low fuel loading in the core, and the long duration of the refueling operation, due to the high temperature and thermal capacity of the primary coolant. The first reason is intrinsic to the reactor type features, so it cannot be changed, but the second reason can be easily addressed through the adoption of a pseudo-online or online refueling. The use of an online (no power reduction) or pseudo-online (partial or total power reduction for a short time, shorter than the Xe build-up effects) procedure substantially reduces the time lost in refueling operation and

115

enables a multi-batch option with a number of batches much higher than a normal refueling procedure, meaning an increase in the fuel burn-up of almost a factor 2, which is the maximum theoretical limit for continuous refueling.

The previous consideration makes the online refueling an interesting and suitable option, due to the low heavy metal loading features of the AHTR. From the neutronic standpoint (multi-batch fuel cycle), some evaluations have been performed by ORNL,[6] but the thermal hydraulic consequences still need to be evaluated.

The feasibility of this procedure is relatively challenging, since the density of the fuel and the coolant are not very different, and the system, with reference to the current design, is not yet capable to enable this option, but the thermal hydraulic analysis at the fuel assembly level can be performed by making simplifying assumptions. The following sections present the modeling and the results for this transient type.

5.4.2.a   Fuel assembly removal transient

The core model described in section 5.2 was used for the transient evaluation; the 6th ring of the core model was modified: the single assembly, representing the 36 real fuel assemblies of the 6th ring, in the initial model was changed to two fuel assemblies, one representing 35 real fuel assemblies of the 6th ring, and one representing the assembly which is to be removed from the core. The 6th ring was selected, because it represents the average condition of the fuel in the core; the properties and structure of the assemblies was not changed.

The initial conditions for the system were set to the steady-state condition presented in section 5.3; the transient was structured in four different parts:

1- The decay heat power is activated in the removed assembly; after the activation, the system evolves for 50 s;

2- Reduction of the form loss coefficient at the entrance of the inter-assembly channels connected to the removed assembly from 1500 (nominal value) to 0; duration: 20 s;

3- Rise of the removed assembly; duration 200 s (3 min and 20 s);

4- Stay of the removed assembly in the upper plenum; duration 200 s (3 min and 20 s);

In relation to the first part, the power in the core was determined by the point kinetics model, similarly to the LOFC transient, and the power of the removed assembly was given by an empirical formula for ^{235}U decay heat.[21]

In relation to the second part, a valve component was used to model the inlet junction of the inter-assembly channels near to the removed assembly, in order to be able to increase the mass flow rate in the interested channel from the initial value to the higher value reached immediately after the detachment of the fuel assembly from the lower support plate.

In relation to the third point, a particular approach has been adopted, since RELAP5 does not allow to model a volume whose height can change with time. A discretized transient was performed: the height of the core was divided into different levels and, for each level, starting from the conditions at the previous level, the geometric configuration was changed (the elevation of the assembly was increased by a discrete amount) and the system was let evolve for the respective amount of time. This procedure was repeated for each axial step, every 10 cm from 0 cm to 6.7 m (full ejection of the assembly from the core), for a 3 s rise time per step.

In relation to the fourth part of the transient, the assembly was left in the upper plenum for a certain amount of time, before being moved to the used fuel storage pool.

5.4.2.b   Fuel assembly removal: results

In relation to the global behavior of the reactor during this type of transient, Figure 5-29 shows the temperatures of the coolant in the lower and upper plenum during the transient; the temperature of the upper plenum is measured in the upper part, accounting even for the coolant that passes through the removed assembly.
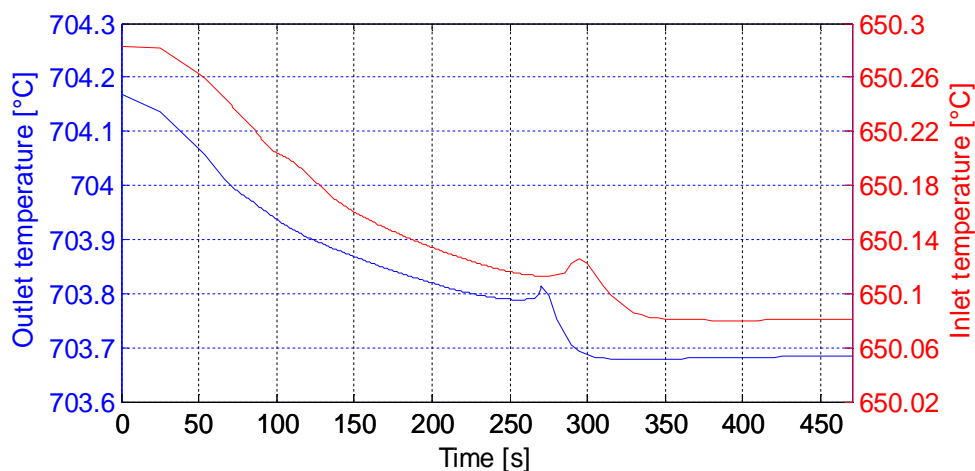
Figure 5-29. Inlet and outlet core temperatures during the transient

Both the inlet and outlet temperature decrease, but the temperature in the upper plenum decreases of 0.5°C, while in the lower plenum the decrease is by an amount equal to 0.2°C; since the total core mass flow rate is unchanged, this means that the total core power is reduced, which is in reasonable agreement with the fact that a control rod was fully inserted in one of the 252 fuel assemblies.

Figure 5-30 shows the maximum and average temperature of the fuel in the core during the transient, excluding the removed assembly.

117

Figure 5-30. Maximum and average fuel temperature in the core during the transient

Despite the lower overall coolant temperature rise across the core (Figure 5-29), both the maximum and average fuel temperature increase, by 2°C and 1°C, respectively; this is due to the fact that even if the total c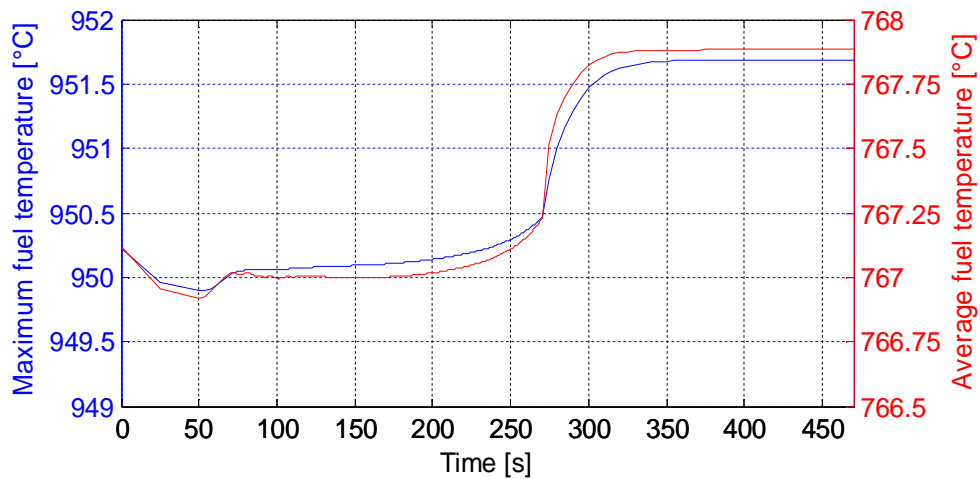ore mass flow rate is constant, its distribution is different: the pressure losses are step by step reduced in the channel of the removed assembly, so the mass flow rate that effectively cools down the core becomes lower, causing an overall increase in the fuel temperature. A lower mass flow rate in the active part of the core means that the mass flow rate in the channel of the removable assembly is increased, as shown in Figure 5-31.
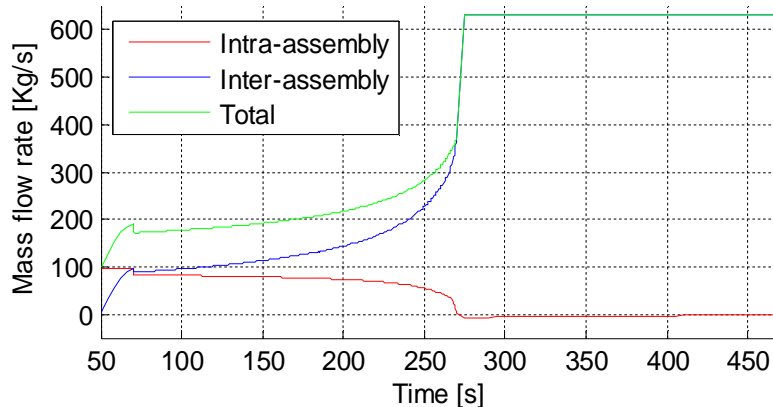
Figure 5-31. Mass flow rate in the intra-assembly channel, in the inter-assembly channel and total mass flow rate for the removed assembly

The total mass flow rate in the assembly channel is represented by the green line; in steady state conditions, it is about 100 kg/s and it increases in three steps:

- From 100 kg/s to 200 kg/s during the initial detachment of the assembly from the plate;
- From 200 kg/s to 400 kg/s during the rise of the assembly in the channel, until 270 s;

- From 400 kg/s to 600 kg/s during the final jump in the upper plenum.

The two components of the flow, the inter- and intra-assembly mass flow, show a different evolution in time: the inter-assembly flow increases, because of the progressive reduction of the friction losses, while the intra-assembly flow decreases from 100 kg/s to about 0 kg/s, when the assembly is completely removed.

Figure 5-32. Maximum and average fuel temperature for the removed assembly during the transient

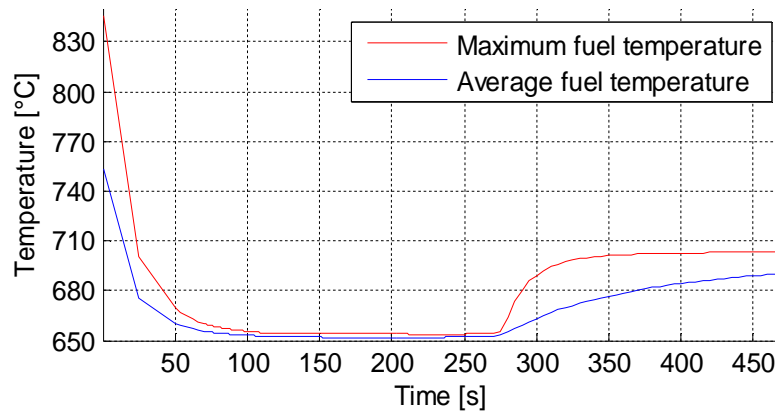The reduction of the intra-assembly mass flow rate causes an increase in the fuel temperature of the removed assembly, as shown in Figure 5-32; initially, the temperature decreases, because of the insertion of the control rod, but when the assembly is completely moved in the upper plenum, the maximum fuel temperature increases to about 700°C. Anyway this value is well below the maximum fuel temperature in nominal operating conditions, so the integrity of the fuel plates is not compromised.

The overall response of the AHTR to the transient shows that the system, from a global point of view, is not strongly affected by the removal of a fuel element; from a local standpoint, the removed fuel assembly does not show a high temperature increase, but the final flow velocity in the channel, about 3.5 m/s, is higher than the nominal design value[6] by a factor 2, resulting in possible corrosion of the structures. The results presented in this section are a preliminary indication about the response of the AHTR to the assembly removal transient; the model requires further work, in order to have a better characterization of all the aspects of the transient, accounting for all the involved phenomena.

CHAPTER 6
CONCLUSIONS AND FUTURE WORK

The work presents different aspects regarding the modeling, the study and the characterization of the AHTR reactor, including both neutronic and thermal-hydraulic evaluations; several models have been developed and tested, in order to obtain a complete view of the problem.

The MATLAB model is a useful tool for preliminary fast evaluations and allows the evaluation of different aspects of the fuel element design and modelling. These evaluations showed that the coolant channel of the AHTR assembly is able to provide effective cooling, requiring a small fraction of the core volume and keeping the fuel temperatures well below the maximum limit for TRISO fuel. The plate fuel configuration was proven to be flexible with respect to a relevant variation of dimensional and design parameters; among the parameters considered for the sensitivity studies, some of them have a relevant influence on the maximum fuel temperature (e.g. cladding thickness), while others have lower importance (e.g. transversal power profile within the fuel plate).

The model gives a good description of the AHTR fuel element, but further work will be required in order to improve its capabilities. In particular, the model will be adapted to account for 2D and 3D heat conduction, for a better description of the temperature distribution; moreover, the characterization of the coolant properties will be improved, considering the effects of heat conduction and more accurate correlations for the pressure drop and the convective heat transfer.

The MATLAB model does not allow the evaluation of transient scenarios; the RELAP5 model provided this capability, but some approximation were introduced in the calculation of the temperature distribution, since a relatively low number of discretized mesh points is desirable to keep the computational time and data output reasonably small, particularly in the case of the full core model. The approximations introduced through a coarser discretization of the model was considered acceptable, since the validation and comparison with the MATLAB model was relatively accurate. 3D effects on the temperature distribution as well as the evaluation of particular local aspects with time dependence cannot be performed through RELAP5, so other codes might be required for a deeper analysis.

The RELAP5 fuel assembly model constituted the intermediate step on the way to the development of a full core model. The model expanded the amount of information available from the single channel model, particularly regarding the heat conduction among fuel plates and support structures (box wall, Y-shaped support). Conduction enclosures were used for the implementation of a pseudo-3D heat conduction model for the structure of the fuel assembly, which could be further improved through an accurate evaluation of more realistic values for the

gap conductance and the area view factor; other codes than RELAP5 3D are required for a more accurate evaluation of the heat distribution in the complex structure of the AHTR fuel element.

An intermediate step, related to the neutronic modeling of the fuel assembly through SCALE, provided important information about the reactivity feedback, along with a basic characterization of the power distribution in the fuel stripe and in the core. Further work is required to improve the modeling, but the results obtained from these initial evaluations were considered reliable. More accurate information about the heavy metal loading is required in order to elaborate a full core model for the calculation of the reactivity feedback, which was performed only at the fuel element level; full core evaluations will provide a better characterization of the power distribution as well as the reactivity feedback, though the computational capabilities required to perform these calculations are substantially higher.

The information collected from the single channel and fuel assembly studies was used for the development of a full core model, in order to be able to evaluate the possible transient and accident scenarios and eventually perform the safety analysis of the reactor.

The LOFC transient was evaluated; the system was proved very effective in the passive heat removal. A similar analysis was performed in order to evaluate the response of the system to a possible online refueling procedure, which would enable a better utilization of the fuel as well as lower cost of electricity. RELAP5 does not allow the modeling of variable volumes, so some approximations have been adopted in order to obtain reasonably interesting information; the results of the simulation are positive, but further analysis, with more appropriate means, is required.

The core model presents the capability to simulate different types of transient, which will be evaluated in the future work. Future work will also include more specific modeling of the coolant flow in the channel and more complete description of the power production inside the plate as well as a 3D plate temperature distribution.

REFERENCES

[1]   Generation IV International Forum, *A Technology Roadmap for Generation IV Nuclear Energy Systems Executive Summary.* March, 2003. GIF-001-00.

[2]   V. K. Varma, D. E. Holcomb, F. J. Peretz, E. C. Bradley, D. Ilas, A. L. Qualls, N. M. Zaharia, *AHTR Mechanical, Structural, and Neutronic Preconceptual Design.* Oak Ridge National Laboratory, September, 2012. ORNL/TM-2012/320.

[3]   S. R. Greene, J. C. Gehin, D. E. Holcomb, et al., *Pre-Conceptual Design of a Fluoride-Salt-Cooled Small Modular Advanced High-Temperature Reactor (SmAHTR).* Oak Ridge National Laboratory, December, 2010. ORNL/TM-2010/199.

[4]   J. A. Phillips, C. M. Barnes, J. D. Hunn, *Fabrication and Comparison of Fuels for Advanced Gas Reactor Irradiation Tests.* Idaho National Laboratory, October, 2010. INL/CON-10-18865.

[5]   *Advanced Gas Reactor Fuel Program's TRISO Particle Fuel Sets A New World Record For Irradiation Performance.* Washington, November, 2009. http://nuclear.energy.gov/genIV/neGenIV9.html.

[6]   D. E. Holcomb, D. Ilas, V. K. Varma, A. T. Cisneros, R. P. Kelly, J. C. Ghein, *Core and Refueling Design Studies for the Advanced High Temperature Reactor.* Oak Ridge National Laboratory, September 30, 2011. ORNL/TM-2011/365.

[7]   C. Jensen, *TRISO Fuel Thermal Conductivity Measurement Instrument Development.* All Graduate Theses and Dissertations, Utah State University, December, 2010. Paper 838.

[8]   H. Gougar, et al., *Prismatic Coupled Neutronics/Thermal fluids transient benchmark of the MHTGR-350 MW Core Design.* June 12, 2010.

[9]   D. F. Williams, L. M. Toth, K. T. Clarno, *Assessment of Candidate Molten Salt Coolants for the Advanced High-Temperature Reactor (AHTR).* Oak Ridge National Laboratory, March, 2006. ORNL/TM-2006/12.

[10]   C. B. Davis, *Implementation of Molten Salt Properties into RELAP5-3D/ATHENA.* Idaho National Laboratory, January, 2005. INEEL/EXT-05-02658.

[11]   Y. Katoh, D. F. Wilson, C. W. Forsberg, *Assessment of Silicon Carbide Composites for Advanced Salt-Cooled Reactors.* Oak Ridge National Laboratory, September, 2007. ORNL/TM-2007/168.

[12]   G. Muralidharan, D. F. Wilson, L. R. Walker, M. L. Santella, D. E. Holcomb, *Cladding Alloys for Fluoride Salt Compatibility.* Oak Ridge National Laboratory, May 25, 2011. ORNL/TM-2011/95.

[13]   *HASTELLOY N alloy.* Haynes International, Inc., 2002. H-2052B.

[14]   D. T. Ingersoll, *Status of Physics and Safety Analyses for the Liquid-Salt-Cooled Very High-Temperature Reactor (LS-VHTR).* Oak Ridge National Laboratory, December, 2005. ORNL/TM-2005/218.

[15]   D. T. Ingersoll, C. W. Forsberg, P. E. MacDonald, *Trade Studies for the Liquid-Salt-Cooled Very High-Temperature Reactor: Fiscal Year 2006 Progress Report.* Oak Ridge National Laboratory, February, 2007. ORNL/TM-2006/140.

[16]   *Pebble Bed Advanced High Temperature Reactor.* http://pb-ahtr.nuc.berkeley.edu. University of California, Berkeley.

[17]   A. Griveau, F. Peterson, *RELAP5-3D Loss of Forced Cooling (LOFC) Transient Response Modeling for the PB-AHTR.* U. C. Berkeley, September 17, 2006. UCBTH-06-003.

[18]   A. Griveau, *Modeling and Transient Analysis for the Pebble Bed Advanced High Temperature Reactor (PB-AHTR).* University of California at Berkeley, February, 2007. UCBTH-07-001.

[19]   RELAP5-3D Code Development Team, *RELAP5-3D Code Manual Volume I: Code Structure, System Models and Solution Methods.* Idaho National Laboratory, June, 2012. INEEL-EXT-98-00834.

[20]   H. J. Lim, P. F. Peterson, *Conceptual Design of the Intermediatee Heat Exchanger (IHX) for the PB-AHTR.* U. C. Berkeley, May 20, 2009. UCBTH-09-0005.

[21]   Todreas N. E., Kazimi M. S., *Nuclear Systems I - Thermal Hydraulic Fundamentals.*